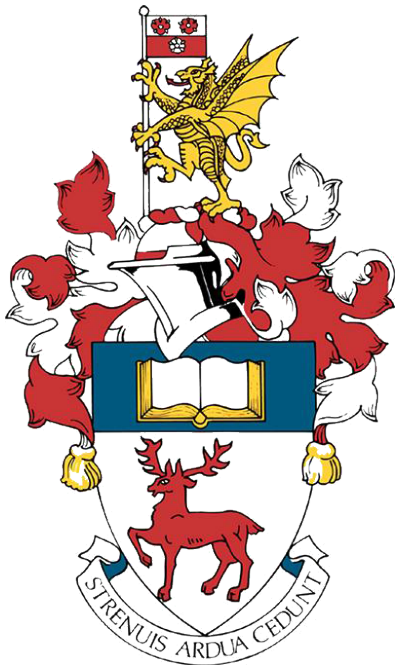

UNIVERSITY OF SOUTHAMPTON

FACULTY OF ENGINEERING AND PHYSICAL SCIENCES

Optoelectronics Research Centre

High-Speed Silicon Photonics Modulators for the 2 µm wavelength

Wei Cao

Thesis for the degree of Doctor of Philosophy

Supervisor: Prof Goran Mashanovich

Co-Supervisor: Dr Miloš Nedeljković

Co-Supervisor: Prof Graham T. Reed

11 June 2020

UNIVERSITY OF SOUTHAMPTON

ABSTRACT

FACULTY OF ENGINEERING AND PHYSICAL SCIENCES
Optoelectronics Research Centre

Doctor of Philosophy

High-Speed Silicon Photonics Modulators for the 2 µm wavelength

by Wei Cao

The 2 µm communication windows has established itself amongst other solutions to address the capacity crunch. The 2 µm window offers three benefits: predicted ultra low loss windows of hollow-core fibres, optical amplification gain windows of thulium doped amplifier and compatibility with the silicon photonics silicon-on-insulator platform.

We demonstrate state of the art high-speed modulators based on a 220 nm silicon-on-insulator platform operating at a wavelength of 1950 nm using the free carrier plasma dispersion effect in silicon. The Mach-Zehnder interferometer carrier-depletion modulator has a modulation efficiency ($V_\pi \cdot L_\pi$) of 2.89 V·cm at 4 V reverse bias. The insertion loss is 5.25 dB. It operates at a data rate of 25 Gbit/s OOK with an extinction ratio of 6.25 dB. We have also demonstrated a streamlined dual drive PAM4 generation method, producing 25 Gbit/s PAM4 signal using the same device.

A Michelson interferometer is demonstrated with a $V_\pi \cdot L_\pi$ of 1.36 V·cm. It has almost double the efficiency of an equivalent MZM. It reaches a data rate of 20 Gbit/s.

A broadband MZM was developed and its performance has been characterized at both 1550 nm and 1950 nm wavelengths. At 1950 nm, the carrier-depletion modulator operates at a data rate of 20 Gbit/s with an extinction ratio of 5.8 dB and insertion loss of 13 dB. The modulation efficiency ($V_\pi \cdot L_\pi$) is 2.68 V·cm at 4 V reverse bias. At 1550 nm, an open eye is obtained at 30 Gbit/s. The difference in bandwidth is caused by the bandwidth limit of the 2 µm measurement setup.

This work is a proof of principle demonstration, significantly improving previously published results and filling the long pending gap for the 2 µm silicon modulators. It paves a route towards a fully silicon-based transceiver in the 2 µm window.

Contents

List of Figures

List of Tables

Declaration of Authorship

I, Wei Cao , declare that the thesis entitled *High-Speed Silicon Photonics Modulators for the 2 μm wavelength* and the work presented in the thesis are both my own, and have been generated by me as the result of my own original research. I confirm that:

- this work was done wholly or mainly while in candidature for a research degree at this University;
- where any part of this thesis has previously been submitted for a degree or any other qualification at this University or any other institution, this has been clearly stated;
- where I have consulted the published work of others, this is always clearly attributed;
- where I have quoted from the work of others, the source is always given. With the exception of such quotations, this thesis is entirely my own work;
- I have acknowledged all main sources of help;
- where the thesis is based on work done by myself jointly with others, I have made clear exactly what was done by others and what I have contributed myself;
- parts of this work have been published as listed in following pages.

Signed:.....

2020-06-11

Date:.....

Related Journal Papers

[1] **Cao, W.**, Hagan, D., Thomson, D. J., Nedeljkovic, M., Littlejohns, C. G., Knights, A., Alam, S.-U., Wang, J., Gardes, F., and others. 'High-speed silicon modulators for the 2 µm wavelength band' *Optica*, 5(9):1055-1062, Sep 2018.

[2] Hagan, D. E., Nedeljkovic, M., **Cao, W.**, Thomson, D. J., Mashanovich, G. Z.,and Knights, A. P. 'Experimental quantification of the free-carrier effect in silicon waveguides at extended wavelengths' *Optics Express* 27(1):166–174, 2019.

[3] Nedeljkovic, M., Littlejohns, C. G., Khokhar, A. Z., Banakar, M., **Cao, W.**, Penades, J. S., Tran, D. T., Gardes, F. Y., Thomson, D. J., Reed, G. T.,and others. 'Silicon-on-insulator free-carrier injection modulators for the mid-infrared' *Optics Letters* 44(4):915–918, 2019.

[4] Li, T., Nedeljkovic, M., Hattasan, N., **Cao, W.**, Qu, Z., Littlejohns, C. G., Penades, J. S., Mastronardi, L., Mittal, V., Benedikovic, D.,and others 'Ge-on-Si modulators operating at mid-infrared wavelengths up to 8 µm' *Photonics Research* 7(8):828–836, 2019.

[5] Mashanovich, G., **Cao, W.**, Qu, Z., Li, K., Thomson, D., Nedeljkovic, M., Hagan, D.,and Knights, A. (2019), 'Mid-Infrared Silicon Photonics for Communications' *International Journal of Electrical Engineering and Computing* 3(1):32–36, 2019.

[6] Mashanovich, G. Z., Nedeljkovic, M., Soler-Penades, J., Qu, Z., **Cao, W.**, Osman, A., Wu, Y., Stirling, C. J., Qi, Y., Cheng, Y. X.,and others. 'Group IV mid-infrared photonics' *Optical Materials Express* 8(8):2276–2286, 2018.

Related Conference Proceedings

[1] **Cao, W.**, M. Nedeljkovic, C. G. Littlejohns, T. Li, Z. Zhou, F. Y. Gardes, D. J. Thomson, G. T. Reed, and G. Z. Mashanovich. 25 Gbit/s silicon based modulators for the 2 µm wavelength band In Optical Fiber Communication Conference (OFC), San Diego, USA, Mar 2020.

[2] **Cao, W.**, Thomson, D. J., Nedeljkovic, M., Alam, S.-u., Wang, J., Gardes, F., Reed, G. T., Mashanovich, G. Z., Littlejohns, C. G., and Rouifed, M.

S. 20-Gb/s Silicon Optical Modulators for the 2 µm Wavelength Band In In *2018 IEEE 15th International Conference on Group IV Photonics (GFP)*, pp. 1-2, Aug 2018.

[3] **Cao, W.**, Milos Nedeljkovic, Shenghao Liu, Callum G. Littlejohns, David J. Thomson, Frederic Gardes, Zhengqi Ren, Ke Li, Graham T. Reed, and Goran Z. Mashanovich Silicon and germanium mid-infrared modulators. In *IEEE Summer Topicals, Hawaii, USA*, pp. 209-210, July 2018. (invited)

[4] Li, K., Thomson, D., Liu, S., Meng, F., Shakoor, A., Khokhar, A., **Cao, W.**, Zhang, W., Wilson, P., and Reed, G. Co-design of electronics and photonics components for Silicon Photonics transmitters In *44th European Conference on Optical Communication*, 2018.

[5] Li, T., Nedeljkovic, M., Hattasan, N., Khokhar, A. Z., Reynolds, S. A., Stanković, S., Banakar, M., **Cao, W.**, Qu, Z., Littlejohns, C. G., and others. Mid-infrared Ge-on-Si electro-absorption modulator In *2017 IEEE 14th International Conference on Group IV Photonics (GFP)*, pp. 7–8, 2017.

[6] Littlejohns, C. G., Nedeljkovic, M., **Cao, W.**, Soler-Penades, J., Hagan, D., Ackert, J. J., Rouifed, M.-S., Wang, W., Zhang, Z., Qiu, H., and others. All silicon approach to modulation and detection at 2 µm In *Optical Interconnects XVIII*, pp. 105380Y, 2018.

[7] Mashanovich, G. Z., Penades, J. S., **Cao, W.**, Qu, Z., Osman, A., Wu, Y., Khokhar, A. Z., Littlejohns, C. J., Stankovic, S., Reynolds, S., and others. Group IV mid-infrared devices and circuits In *Integrated Optics: Devices, Materials, and Technologies XXII*, pp. 1053512, 2018.

[8] Thomson, D. J., Li, K., **Cao, W.**, Hagan, D., Liu, S., Meng, F., Nedeljkovic, M., Khokhar, A. Z., Littlejohns, C. G., Zhang, W., and others. Silicon Optical Modulators for Data Transmission in Different Wavelength Bands In *2019 21st International Conference on Transparent Optical Networks (ICTON)*, pp. 1–4, 2019.

[9] Zhang, W., Debnath, K., Chen, B., Husain, M. K., Khokhar, A. Z., Liu, S., Byers, J., **Cao, W.**, Ebert, M., Reynolds, J. D., and others. High speed silicon capacitor modulators for TM polarisation In *2019 IEEE 16th International Conference on Group IV Photonics (GFP)*, pp. 1–2, 2019.

Other Journal Papers

[1] Perez, D., Gasulla, I., Crudgington, L., Thomson, D. J., Khokhar, A. Z., Li, K., **Cao, W.**, Mashanovich, G. Z., and Capmany, J. 'Multipurpose silicon photonics signal processor core' *Nature communications* 8(1):636, 2017.

[2] Perez, D., Gasulla, I., Fraile, F. J., Crudgington, L., Thomson, D. J., Khokhar, A. Z., Li, K., **Cao, W.**, Mashanovich, G. Z., and Capmany, J. 'Silicon photonics rectangular universal interferometer' *Laser & Photonics Reviews* 11(6):1700219, 2017.

[3] Mashanovich, G., Mitchell, C., Penades, J. S., Khokhar, A., Littlejohns, C., **Cao, W.**, Qu, Z., Stankovic, S., Gardes, F., Masaud, T. B., and others. 'Germanium Mid-Infrared Photonic Devices' *Journal of Lightwave Technology* 35(4):624-630, 2017.

[4] Milosevic, M. M., Chen, X., **Cao, W.**, Runge, A. F. J., Franz, Y., Littlejohns, C. G., Mailis, S., Peacock, A. C., Thomson, D. J., and Reed, G. T. 'Ion implantation in silicon for trimming the operating wavelength of ring resonators' *IEEE Journal of Selected Topics in Quantum Electronics* 24(4):1–7, 2018.

[5] Penades, J. S., Sánchez-Postigo, A., Nedeljkovic, M., Ortega-Mocux, A., Wangüemert-Perez, J. G., Xu, Y., Halir, R., Qu, Z., Khokhar, A. Z., Osman, A., **Cao, W.**, and others. 'Suspended silicon waveguides for long-wave infrared wavelengths' *Optics Letters* 43(4):795–798, 2018.

[6] Sánchez-Postigo, A., Wangüemert-Perez, J. G., Penades, J. S., Ortega-Mocux, A., Nedeljkovic, M., Halir, R., Mimun, F. E. M., Cheng, Y. X., Qu, Z., Khokhar, A. Z., Osman, A., **Cao, W.**, and others. 'Mid-infrared suspended waveguide platform and building blocks' *IET Optoelectronics* 13(2):55–61, 2018.

[7] Wu, Y., Qu, Z., Osman, A., **Cao, W.**, Khokhar, A. Z., Soler Penades, J., Muskens, O. L., Mashanovich, G. Z., and Nedeljkovic, M. 'Mid-infrared nanometallic antenna assisted silicon waveguide based bolometers' *ACS Photonics* 6(12):3253–3260, 2019.

Other Conference Proceedings

[1] Wu, Y, Khokhar, A. Z., Mashanovich, G. Z., Muskens, O. L., Osman, A. M., Penades, J. S., Cao, W., Qu, Z., and Nedeljkovic, M. (2019), Mid-Infrared Silicon Waveguide-Based Bolometer, in '2019 IEEE 16th International Conference on Group IV Photonics (GFP)', pp. 1–2.

[2] Mashanovich, G. Z., Littlejohns, C. G., Thomson, D. J., Cao, W., Li, T., Khokhar, A. Z., Stankovic, S., Penades, J. S., Qu, Z., Mitchell, C. J., and others (2017), Germanium and silicon photonic integrated circuits for the mid-infrared, in '2017 19th International Conference on Transparent Optical Networks (ICTON)', pp. 1–1.

[3] Milosevic, M. M., Chen, X., Cao, W., Khokhar, A. Z., Thomson, D. J., and Reed, G. T. (2017), Towards autonomous testing of photonic integrated circuits, in 'Silicon Photonics XII', pp. 1010817.

[4] Milosevic, M. M., Chen, X., Cao, W., Thomson, D. J., Reed, G. T., Littlejohns, C. G., and Wang, H. (2017), Ion implantation in silicon for photonic device trimming, in '2017 Conference on Lasers and Electro-Optics Pacific Rim (CLEO-PR)', pp. 1–2.

[5] Perez, D., Gasulla, I., Capmany, J., Crudgington, L., Thomson, D. J., Khokhar, A. Z., Li, K., Cao, W., and Mashanovich, G. Z. (2017), Integrated RF-photonic delay lines using reconfigurable photonic waveguide meshes, in '2017 International Topical Meeting on Microwave Photonics (MWP)', pp. 1–4.

[6] Perez, D., Gasulla, I., Crudgington, L., Thomson, D. J., Khokhar, A. Z., Li, K., Cao, W., Mashanovich, G. Z., and Capmany, J. (2017), Compact programmable RF-photonic filters using integrated waveguide mesh processors, in '2017 19th International Conference on Transparent Optical Networks (ICTON)', pp. 1–4.

[7] Perez, D., Gasulla, I., Crudgington, L., Thomson, D. J., Khokhar, A. Z., Li, K., Cao, W., Mashanovich, G. Z., and Capmany, J. (2017), Silicon RF-Photonics Processor Reconfigurable Core, in '2017 European Conference on Optical Communication (ECOC)', pp. 1–3.

[8] Qu, Z., Nedeljkovic, M., Wu, Y., Penades, J. S., Khokhar, A. Z., Cao, W., Osman, A. M., Qi, Y., Aspiotis, N. K., Morgan, K. A., and others (2018),

Waveguide integrated graphene mid-infrared photodetector, in 'Silicon Photonics XIII', pp. 105371N.

[9] Reed, G. T., Chen, X., Milosevic, M. M., Cao, W., Littlejohns, C., Khokhar, A. Z., Franz, Y., Runge, A. F. J., Mailis, S., Thomson, D. J., and others (2018), Advancing silicon photonics by germanium ion implantation into silicon, in 'Smart Photonic and Optoelectronic Integrated Circuits XX', pp. 105361T.

[10] Reed, G. T., Milosevic, M. M., Chen, X., Cao, W., Littlejohns, C. G., Wang, H., Khokhar, A. Z., and Thomson, D. J. (2017), Ion implantation in silicon to facilitate testing of photonic circuits, in 'Smart Photonic and Optoelectronic Integrated Circuits XIX', pp. 1010709.

[11] Sánchez-Postigo, A., Wangüemert-Perez, G., Penades, J. S., Ortega-Mocux, A., Nedeljkovic, M., Halir, R., Mimum, F. E. M., Qu, Z., Khokhar, A. Z., Osman, A., and others (2019), Suspended silicon integrated platform for the long-wavelength mid-infrared band, in '2019 21st International Conference on Transparent Optical Networks (ICTON)', pp. 1–4.

Chapter 1

Introduction

Fibre based telecommunication systems have sustained a startling increase in capacity demand since the inception of the internet. The introduction of technologies such as erbium doped fibre amplifiers (EDFA), wavelength division multiplexing (WDM) and high-spectral efficiency coding have allowed bandwidth capacity to keep up with demand [1]. The optical fibres transmission capacity was once deemed almost boundless. However, with the latest digital signal processing (DSP) assisted coherent detection we are getting ever closer to the theoretical capacity limit of conventional single mode fibres (SMFs) [2]. There are techniques to further squeeze out the remaining bit of capacity, but it faces diminishing returns [3] or involves significantly scaled-up power consumption.

The total capacity demand has nevertheless maintained its exponential growth trend, fuelled by bandwidth-hungry applications, such as HD video streaming and cloud based services, and facilitated by the upcoming 5G network. In the longer term, we cannot yet even see the cap or slowing down of the trend, at least in the foreseeable future the upcoming 4K and 8K video streaming/broadcasting, immersive virtual reality (VR), self-driving cars, internet of things are all behemoths of data flow that keep spurring the demand boom [4]. As illustrated as the orange curve in figure 1.1, the projected demand may eventually hit the stagnant capacity ceiling, resulting in a 'capacity crunch', where the current communication system can no longer sustain the bandwidth demands of the internet [1].

The crisis might not be imminent as it can be addressed by funding more infrastructure with multiple parallel links (including spatial division multiplexing (SDM)) and by trimming down the transmitted data via compression. This may

partly solve the issue, but neither solution can be scaled up indefinitely as multiple links and data compression implies a substantial hike in energy consumption.

The more elegant solution is to develop technologies to further increase spectral efficiency without a significant increase in launch power. Such technologies when used in conjunction with SDM, are able to offer the next round of revolutionary capacity boost.

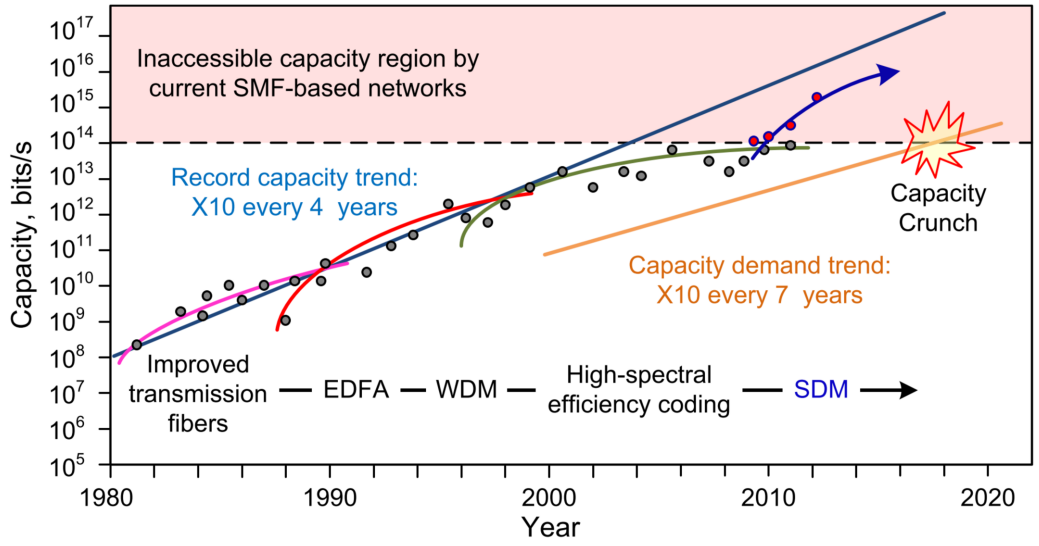

Figure 1.1: Reproduced from book Fibre Optic Communication [5]

One possible route is to enhance the fundamental property of optical fibre and hence increase the Non-Linear Shannon Limit. A promising emerging candidate is a hollow-core photonic bandgap fibre (HC-PBGF). The optical mode resides largely in the air core of HC-PBGFs, hence minimizing the Rayleigh scattering (λ^{-4} wavelength dependence), which is the dominant source of loss in standard SMFs. By considering remaining loss mechanisms namely surface scattering (λ^{-3} wavelength dependence) and infrared absorption loss of the silicon dioxide, the predicted lowest loss windows is shifted from 1550 nm to 1900 - 2100 nm band and the theoretical minimum loss achievable is below 0.1 dB/km [6, 7], which is lower than the best conventional SMF (0.1484 dB/km) [8]. Furthermore, the nonlinearity of HC-PBGF can be highly reduced, owing to the fact that a large fraction of the light propagates in the air core that has extremely weak nonlinear property [9]. With the aforementioned low loss and low nonlinearity, and some other advantages including low latency [10], low thermal sensitivity [11] and high radiation hardness [12], HC-PBGF shows great potential as a candidate building block of future telecommunication systems.

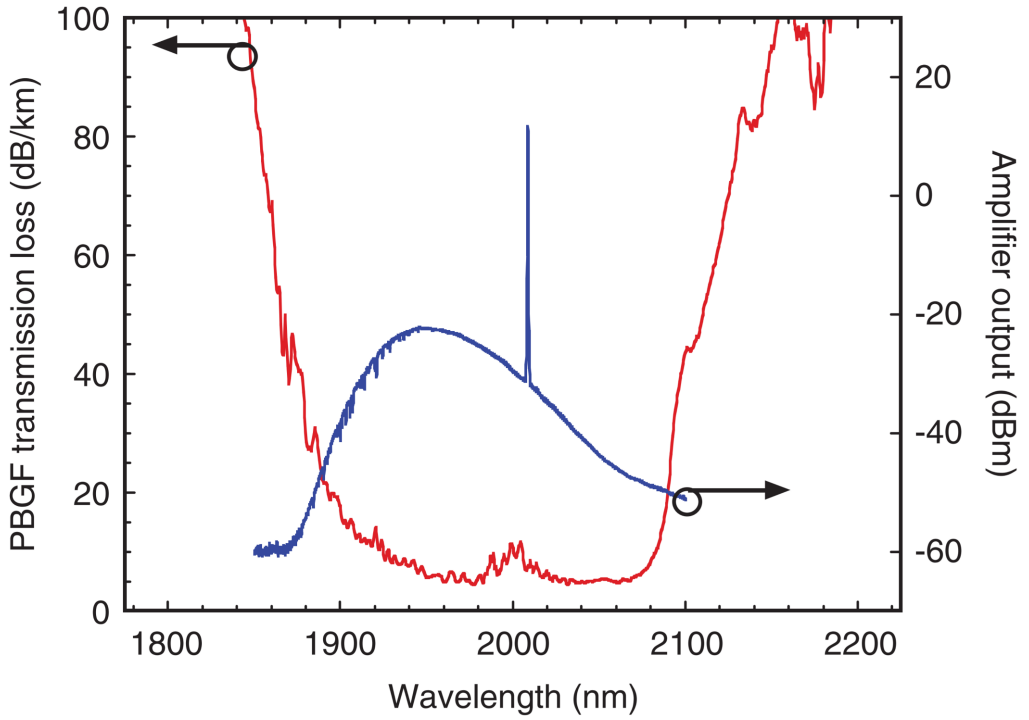

Figure 1.2: Image courtesy [13]

Researchers have demonstrated a 3.8 km long hollow-core fibre with loss as low as 3 dB/km at 2 µm [14, 15]. Although, it is still a magnitude away from the predicted sub 0.1 dB/km loss figure, the breakthroughs in hollow-core fibre drawing have indeed offered a opportunity of open the 2 µm wavelength window [16].

Coincidentally, the optical gain window of thulium-doped fibre amplifiers (TDFA) resides at around 1910 - 2020 nm as in figure 1.2 and it can be used as the equivalent to erbium-doped fibre amplifiers (EDFA) in a 2 µm system [17, 18]. Another advantage of such a system is the compatibility with silicon photonics, as the material loss of silicon dioxide is low at 2 µm [19] (Figure 1.3) and low propagation loss strip and rib waveguides on an SOI platform have been demonstrated [20]. This allows for potentially fully integrated high performance transceivers mass produced with reduced cost by leveraging complementary metal–oxide–semiconductor (CMOS)-compatible fabrication processes. Aside from the cost, optical systems based on silicon photonics are generally compact owing to the large refractive index contrast between the silicon core and the oxide cladding. Such a property is especially conducive to integrating large complex transceiver systems potentially with on-chip WDM and multiple modulators and detectors. Several silicon photonics based bulk defect-mediated absorption (BDA) types of detector in 2 µm have been successfully demonstrated. Ackert et al. [21] have realised the highest data rate defect photodiode (PD) so far, which can operate at 20 Gbit/s at 2

µm in silicon. However, prior to our work there have been few demonstrations of high-speed 2 µm group-IV material based modulators.

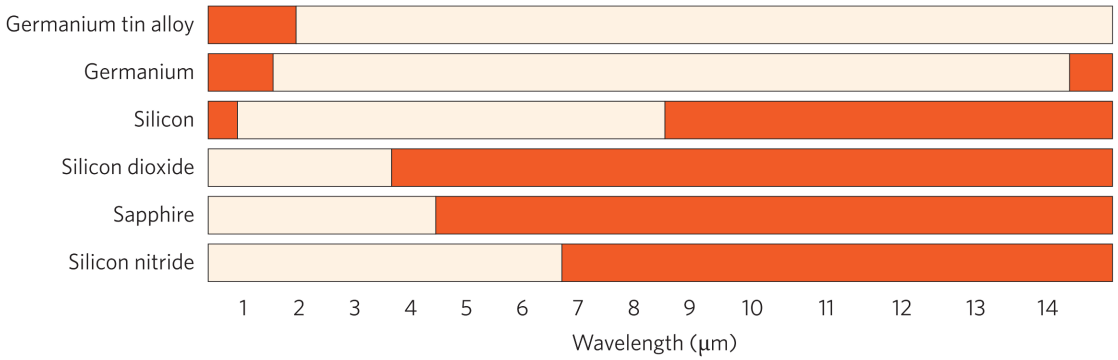

Figure 1.3: List of material candidates which is transparent in MIR range. The light beige region indicates optical propagation loss is less than 2 dB/cm, the red region represents high loss. After [19]

Outline of the thesis:

Chapter 2 will further elaborate on how to overcome the capacity crunch by innovations in fibres. It analysed the benefit of opening a telecommunication windows in 2 µm wavelength band in terms of improving spectral efficiency and expanding channel bandwidth. Followed by a literature review on the various development 2 µdevices and demonstrations of 2 µsystems.

Chapter 3 goes through the fundamentals of a Mach-Zehnder electo-optical modulator. It starts from basic passive building blocks of a modulator, in which the operation of Mach-Zehnder interferometers are covered in detail as this is the one of the cornerstone of our modulator. It then moves to the active device, the various modulation mechanism in silicon are discussed and the most widely used plasma dispersion effect is emphasised with examples of PN junction phase shifter structures. The MZM performance criteria are listed with exampled 1550 nm modulators, some important properties such as phase shift, efficiency are covered with details showing how to calculate them. We then moved to 2 µregime, and the plasma dispersion effect difference between 1550 nm and 2 µare compared. Finally, all silicon based 2 µmodulators, to our knowledge including our works, have been reviewed.

Chapter 4 delineates the design procedure of a 2 µhigh-speed silicon modulator. It starts from an optical mode trend analysis in a waveguide for different wavelengths. The active simulation flow is introduced later. The phase shifter performances are simulated and analysed against wavelength, PN junction position and highly-doped region position. To fully understand how doping concentration may affect

the device performance, both DC and AC analysis are performed. The whole device was put together as a layout mask. Method of how to draw such a layout mask and some design considerations are then explained.

Chapter 5 introduces the lab setup in the high-speed modulator measurement for both conventional 1550 nm devices and 2 µdevices.

Chapter 6 comprises four sections corresponding to four series of actual experimental results. The actual design parameters and specific testing conditions are also given along with the results. The four series of experiments are 1) 20 Gbit/s broadband MZM, 2) 25 Gbit/s dedicated 2 µm MZM, 3) 20 Gbit/s Michelson interferometer modulator, and 4) 25 Gbit/s PAM4 signal with 2 µm MZM.

Chapter 7 concludes the work and the thesis with outlooks of future works.

Chapter 2

2-μm Communication Window

2.1 Capacity Limits in Conventional Fibres

The upper capacity boundary of classical memoryless additive white Gaussian noise (AWGN) channels has been defined by the well-known Shannon's theorem derived from fundamental information theory [22]. The channel capacity is given as,

$$C = B \log_2 [1 + SNR] \tag{2.1}$$

where C is the channel capacity, B is the effective transmission bandwidth and SNR is the effective channel signal-to-noise ratio.

For a conventional single mode optical fibre link, if we define the spectral efficiency as SE, we have [23],

$$C = 2 \cdot B \cdot SE \tag{2.2}$$

where the factor 2 arises from the fact that in a conventional SMF fibre core, we can utilize 2 polarisation modes for polarisation division multiplexing (PDM)[1]. For existing SMF systems, the transmission line bandwidth B is limited by the bandwidth of the EDFA and is around 10THz. The spectral efficiency SE for a

[1]SMF is not polarization maintaining, the two polarization signal channels will lose their original polarisation states at the receiver end. However as long as both polarisation channel are orthogonal to each other, the signal can be retrieved by using polarization demultiplexing and polarization mode dispersion (PMD) compensation techniques, eg. finite impulse response (FIR) filters [24]. Coherent QPSK with polarization multiplexing (DP-QPSK) via SMF is widely used in WDM transmission practices [25, 26].

purely linear fibre, is limited by Shannon's theorem.

$$SE = \log_2 [1 + OSNR] \tag{2.3}$$

Therefore in a linear fibre, the SE can theoretically be improved by cranking up the optical signal to noise ratio (OSNR). This implies an almost indefinite scale up of SE by increase the launching power, until material failure. However real fibre is no where near a linear medium, the silica has inherent nonlinear effect such as cross phase modulation (XPM) and four wave mixing (FWM). These are manifested as crosstalk between adjacent spectral channels, degrading the overall spectral density (SE). The so-called nonlinear Shannon limit has taken nonlinear effect into account, and predicts a maximum value of SE at a certain launch power. A consensus has not yet been reached on the exact expression to estimate the nonlinear Shannon limit, several works has been published taking account different levels of nonlinear effect and nonlinearity compensation [27, 28, 29, 30, 31]. For explanatory purpose, the maxima is clearly illustrated in figure 2.2 excerpted from [2] which uses the analytical estimation formulae proposed in [32]. We can see from the solid black curve, depicting the conventional SMF system, the spectral efficiency drops off after a certain power.

According to the equation 2.2, to improve channel capacity, one can either increase spectral efficiency (SE) or total bandwidth (B). Various techniques have been developed and implemented to improve SE, namely advanced modulation formats including DSP assisted coherent detection, nonlinear transmission optimization, geometrical and probabilistic shaping, variable spectral efficiency. These optimization techniques however are still operating within the boundary of nonlinear Shannon limit of SMF. There are further more expensive techniques using DSP to compensate dispersion and nonlinearity but only to a limited extent. It will be the backbone network that feels the capacity crunch first, which uses the C band. In the C band, with the help of the above mentioned techniques, the record to date reaches 34.9 Tb/s over 6375 km with SE of 8.3 b/s/Hz [33]. To explore a wider bandwidth, there has also been research demonstrating a record breaking C+L band transmission with 71.64 Tb/s capacity over 6960 km distance. The SE however is slightly lower at 7.36 b/s/Hz. [34] To fully saturate the SMF capacity there is still years of development that can be done, but the closer the limit, the harder it will get, the associated cost and latency might increase significantly.

For anything beyond that, we need to start looking for more drastic new solutions. For a single link, the principle is still to raise SE by improving optical fibre

characteristics and B by expanding the wavelength band; and another way is to explore the spatial domain, using multi-mode fibre, multi-core fibre or parallel fibre bundles.

2.2 Exceeding the Limit with 2 µm photonics

The development of 2 µm communication systems can fit into this future plan by simultaneously improve the SE and B, while remaining compatible with the spatial multiplexing.

2.2.1 Enhancing the Spectral Efficiency

The incumbent commercial SMF fibre has not yet been fundamentally improved for many years, but we have been approaching ever closer to its nonlinear Shannon limit defined by the signal impairment properties namely loss, dispersion and nonlinearity. The loss is mainly contributed by Rayleigh scattering and infra-red photonics absorption by silica. The former has a λ^{-3} wavelength dependence and dominant at shorter wavelengths. While we increase wavelength hoping to reduce the Rayleigh scattering, it will quickly hit the infrared absorption edge of silica, which rises quickly beyond 1.7 µm. Therefore 1550 nm becomes the optimal point in terms of low loss.

People have tempted to push spectral efficiency beyond the envelope defined by the silica material even before the invention of EDFA by experimenting with novel materials such as soft glass (eg. ZBLAN), chalcogenide glass etc. They may offer significantly superior loss properties than silica fibre by moving towards the mid-infrared region and hence avoid high Rayleigh scattering. However these are extremely brittle fibres that cannot bend too much, and generally have high nonlinearity. The later revolution in EDFA has soon rendered the soft glass approach obsolete. However even to date, there is still attempts perfect the manufacturing process of soft glass. Two companies have even been experimenting drawing ZBLAN fibre in space hoping the microgravity environment will aid in reducing the loss to a point that no optical amplifier is needed for a transatlantic link [35].

We might be able to achieve a similar result while remaining on ground though. Hollow-core photonic bandgap fibres (HC-PBGFs) create bandgaps by clearly engineered wavelength-sized cladding structure, which largely traps the optical mode

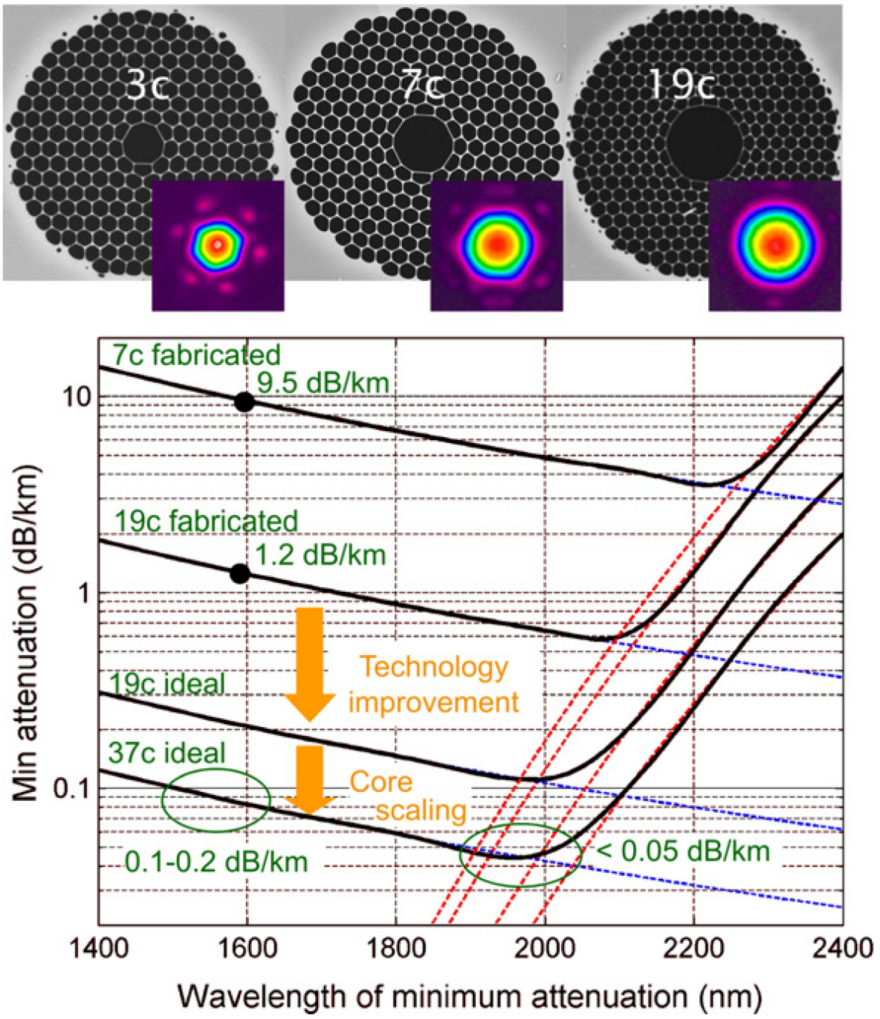

Figure 2.1: Top part: Cross sections SEM images of HC-PBFGs with different core sizes with corresponding fundamental mode image. Bottom part: Predicted fibre attenuation against the wavelength of HC-PBFGs. The total loss is defined by the surface scattering and infrared absorption edge. The lowest loss and low loss windows is defined by the cross point of the two loss mechanism. Image courtesy [7].

inside an air core. Air does have orders of magnitude lower Rayleigh scattering and has a infrared absorption at a significantly longer wavelength. Therefore the Rayleigh scattering in hollow-core fibre is almost negligible and the loss at lower wavelengths is dominated by surface scattering between air and silica cladding, which is a higher order loss mechanism and has a wavelength dependence of λ^{-4}. The surface scattering loss may be improved with more advanced manufacturing techniques. The demonstrated hollow core fibre loss are summaries in the table 2.1; the lowest loss published reaches 1.2 dB/km at 1620 nm wavelength [6]. The extrapolated surface scattering losses are then shown in graph 2.1 as blue dotted lines.

Other loss factor is the remnant mode residing in the silica cladding, which can be reduced by increasing air core size and use of high air fraction cladding, which shifts the red dotted lines towards the right in figure 2.1. Considering both loss mechanisms, the predicted overall loss minima lands in the region of 1900-2100 nm. It could reach around 0.1 dB/km for a 19c-sized air core fibre [6, 7], comparing to the 0.2 dB/km-loss SMF fibre widely used currently.

Nevertheless, the bend loss is higher in hollow-core fibres compare to conventional fibres due to its larger mode. A huge 37-cell hollow core fibre could be especially vulnerable. However, there is a demonstration of 37c HC-PBGFs, despite the handicap, showing the a very good bend loss and modal stability in a record data transmission capacity test [36].

Table 2.1: The demonstrated loss and distance of Hollow-core photonic bandgap fibres (HC-PBGFs) in chronological order.

Year & Ref	**Wavelength (nm)**	**Loss (dB/km)**	**Length (km)**	**BW (nm)**
2004 OFC [37]	1565	1.7	3	20
2005 OE [6]	1620	1.2	-	-
2012 OFC [38]	1510	3.5	0.25	160
2013 OL [39]	1530	1.8	0.5	40
2014 OFC [40]	1510	8.0	0.95	160
2015 OE [41]	1990	2.8	1.15	85
2015 JLT [14]	2010	3.2	3.85	160
2015 JLT [14]	2001	2.5	0.5	122
2015 OFC [42]	1538	6.5	2.75	12
2016 JLT [15]	1560	5.2	11.07	200

The large proportion of mode inside the air core has another advantage, that is low nonlinearity. As air compared to silica is effectively linear, a 0.001% mode overlap in silica translates to slashing the nonlinearity of the fibre down to 1/1000th of that of solid core counterpart. [9] This means it can sustain a much higher launch power, hence gaining a higher OSNR and a higher spectral efficiency.

Figure 2.2 illustrated the SE performance of various fibre systems, and it clearly depicts the advantage of hollow core fibre over traditional SMF fibre. As we can see, at higher overall launch power, the spatial division multiplexing (the dashed line) offers proportionally higher SE to a certain point. It is able to overcome the nonlinear edge by essentially diluting the power in each fibre/mode. The reduced in amplifier noise (blue curve), shows a moderate increase in SE at the same launch

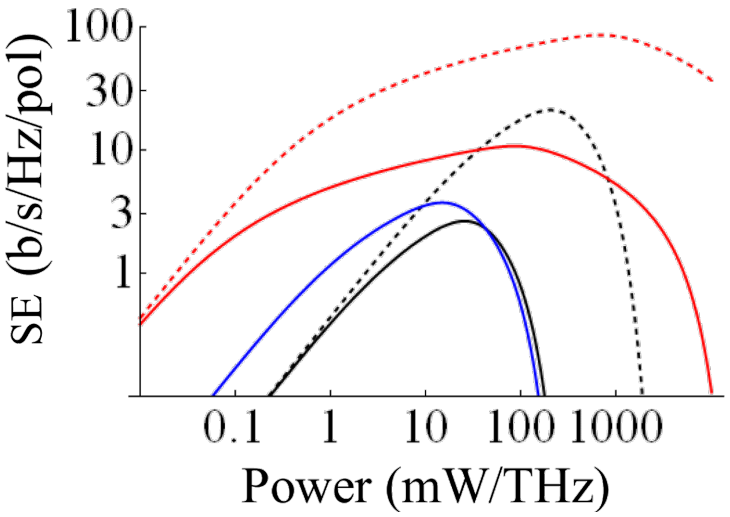

Figure 2.2: Calculated SE for different types of fibre, amplification and spatial division multiplexing. In the model, total fibre length is 10,000 km with 125 km amplifier spacing. Solid black curve: conventional SMF. Dotted black curve: a perfect 8 channel spatial division multiplexing without crosstalk. Solid blue curve: phase sensitive amplifiers with 6dB OSNR improvement. Solid red curve: loss loss hollow core fibre (0.05dB/km). Dotted red curve: low loss hollow core fibre and 8 channel spatial division multiplexing. Image courtesy [2].

power. This is due to improved OSNR and a reduced loss should have a similar curve shifting trend. The hollow core fibre (solid red) however offers both higher SE and given launch power thanks to the lower loss, and higher nonlinear edge thanks to the significantly lower nonlinear effect. Therefore single link hollow core fibre is predicted to have around 2-4 fold increase in SE. When paired with spatial division multiplexing (dashed red), it truly shows a substantial SE boost. [2]

The hollow core fibre can also offer a low latency transmission [10], due to the fact that air has a refractive index of 1 and silica has a refractive index of 1.4-1.5. This is vital in latency sensitive applications such as high frequency trading. The air core can also help reducing the thermal sensitivity of group delay. it is now limited by the higher order material thermal expansion, quoting 2 ps/km/K comparing to SMFs's 40 ps/km/K [11]. The thermal sensitivity can be further reduced to almost zero, by engineering the fibre so to have a negative thermally induced group velocity change and effectively compensating the material elongation. [43]

Other extra perks of using a hollow-core fibre includes dispersion control, and high radiation hardness[2] [12].

[2]HC-PBGF shows radiation induced loss (RIA) of 2.1dB/km in one experiment with 940kGy gamma dose, which is two orders of magnitude less than in a conventional fibre. The mechanism

2.2.2 Extending the Optical Bandwidth

Apart from improving SE, expanding the bandwidth B can also be a straightforward method to boost the capacity. As illustrated in figure 2.3, the predicted low loss windows of HC-PBGF has a frequency bandwidth of 37 THz which is almost three times of the conventional C+L band.

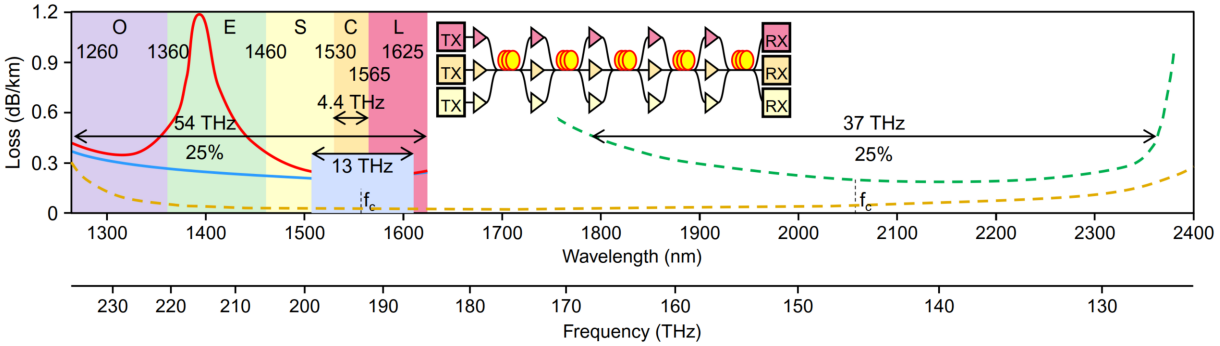

Figure 2.3: Low loss windows of SMF ranging from 1260 nm to 1625 nm is shown on the left. The red curve depict the loss of a fibre with the hydroxyl absorption peak and blue curve shows the fibre without the hydroxyl absorption peak. The dashed green line shows the predicted loss of Hollow-core photonic bandgap fibre (HC-PBGF) and the orange curve shows a predicted loss performance of a nested anti-resonant nodeless hollow-core fibre. Image courtesy of [44].

As for the optical fibre amplifier, Tm^{3+} ion has a gain windows range around 1700-2050 nm [18]. If Ho^{3+} ion dopant is added into the mix, it is possible to expand the gain window coverage even further into the 2200 nm. Therefore the whole 37 THz low loss windows can be unlocked by such fibre amplifier.

There is a new type of hollow-core fibre called anti-resonant fibre which in theory is capable of delivering an even lower loss and wider low loss window than HC-PBGF. The orange curve in figure 2.3 illustrates its performance, whose low loss window covers the whole 1300 nm - 2400 nm range. In fact hollow-core anti-resonant fibres have demonstrated some record low loss (summaries in table 2.2) amongst various types of hollow core fibres. Although so far it is still challenging to draw a sufficiently long anti-resonant fibre.

of radiation induced loss is not yet conclusive but includes radiation induced point defects in silica, radiation induced surface roughness, increased attenuation in ionized air. The low RIA in hollow core fibre might result from a low overlap of the mode and defects in silica. [12]

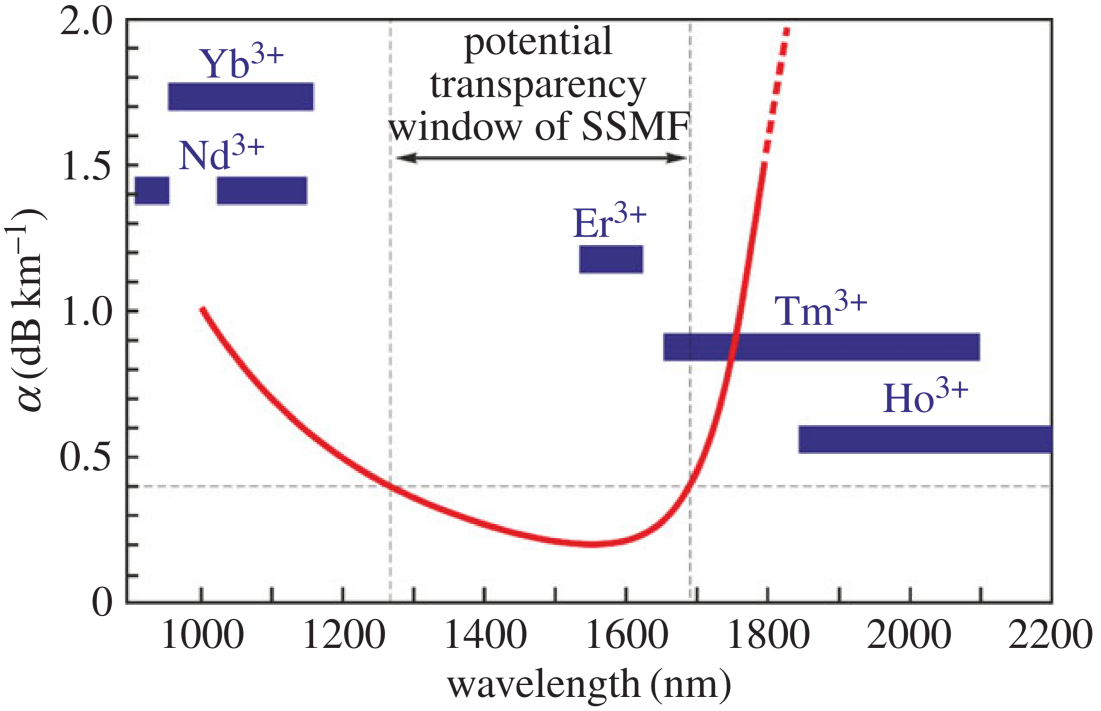

Figure 2.4: Optical gain windows of various rare-earth ions doped in silica. Image courtesy [23].

Year & Ref	λ (nm)	Loss (dB/km)	Length (km)	BW Span
2018 NC [45]	1512	2.0	0.33	1302-1637 nm (loss <16 dB km^{-1})
2019 OE [46]	1540	0.35	-	1330-1660 nm (loss <1 dB km^{-1})

Table 2.2: The demonstrated loss and bandwidth range of hollow-core anti-resonant fibres.

2.3 2 µm system - the state of the art

The 2µm communication system involves high speed transceiver, fibres and fibre amplifiers etc. Recent breakthroughs in hollow-core photonic bandgap fibre makes such a system feasible. Researchers have demonstrated a 3.8km long hollow-core fibre with loss as low as 3dB/km at 2 µm [14]. Also thulium-doped fibre amplifier (TDFA) works at 2 µm regime and can used as an MIR equivalent to erbium-doped fibre amplifier (EDFA). Several successful bulk defect-mediated absorption (BDA) types of detector in 2um have been demonstrated. These have all paved the way to a successful 2 µm communication system.

As for the transceiver, it consists of an optical modulator and a detector. Ackert et al. [21] have realised fastest defect photodiode (PD) so far, which can operate at data rate of 20 Gbit/s at 2 µm. At NIR, plasma dispersion effect based modulators show high performance and good CMOS compatibility [47]. In the near-infrared (NIR), plasma dispersion effect based modulators show convincing performance, as well as CMOS compatibility [47], with data rates of up to 90 Gbit/s [48]. A theoretical analysis of the plasma dispersion effect in the mid-infrared (MIR) has been performed [49] and suggests that the effect is present in the 2 µm regime and is even moderately stronger than in the NIR. However, prior to our work to our knowledge the only demonstration of 2 µm wavelength high-speed modulator using silicon carrier effect was made by IBM who have reported SOI carrier injection modulators operating at 2165 nm. Using a pre-emphasis drive signal, the device reached a bitrate of 3 Gbit/s [50]. The same year as our work published, there are several groups demonstrated the µhigh speed modulator and this will be discussed in section 3.8.

Towards longer wavelengths, an electro-absorption modulator is shown operating at 3.8 µm with a data rate of at least 6 MHz. [51]. Optical attenuators (VOA) based on free carrier injection have also been demonstrated on both silicon-on-insulator (SOI) [52] and germanium-on-insulator platforms [53]. Nedeljkovic et al. have realised a thermal-based SOI modulator operating at KHz regime [54]. Other modulation approaches exploit Pockels effect in silicon-on-lithium-niobate, which demonstrated 23KHz at 3.39µm wavelength [55]. Some theoretical proof of concept analysis of modulating using Aluminium Nitride [56] and GeSn quantum well [57]has also been published. Direct modulation of QCL laser has been attempted at room temperature at around 4.72 µm wavelength [58]. On germanium-on-silicon platform an all optical modulator based on free-carrier absorption has been demonstrated working at around 55MHz across the 2-3.2 µm wavelength range [59]. Recently a 15 GHz all optical modulator operating in the 3.5-4.4 µm wavelength range has been demonstrated using porous Si membranes [60].

There have been several high-speed transmission demonstrations over HC-PBGF in 2 µm. The recently developed 2µm lasers [61, 62], Hollow Core Photonic Bandgap Fibers (HC-PBGF), TDFAs [17, 18], AWGs [63], optical hybrids [64], PDs [65, 66, 67], all ensure the feasibility of 2 µm transmission system. 2µm InGaAs quantum well photo detector has been first demonstrated in 2012 operating at 7 GHz and with 0.3 A/W responsivity. At 1550 nm the device maintained similar performance. [65] Later an improved edge-coupled version with a butterfly packaging shows a bandwidth of 10 GHz. [66] A surface coupled version with

10GHz bandwidth and 0.93 A/W has also been shown. [67] The state of art III-V photodiode to date has a bandwidth of 25 GHz and shows an eye at 30 Gbit/s. The device however has a relatively moderate responsivity of 0.07 A/W [68].

Most of the systems demonstrating 2µm modulation resort to directly modulated laser (internal modulation) or using commercially available LiNbO3 MZMs (eg. MX2000-LN-10, Photline). [41, 69, 70, 14, 58] The state of art demonstration shows 8 channel total 100Gbit/s capacity at 2 µm, with 4 internal modulation channels each at 9.3 Gbit/s and 4 external modulation channels each at 15.7 Gbit/s . The direct modulated laser is based on $In_{0.75}Ga_{0.25}As$ quantum well and with a bandwidth of 5.1 GHz. The encoding technique (double side-band 4-ASK Fast-OFDM) used has spectral efficiency of 2 bit/s/Hz, and 7% overheads, hence the 9.3 Gbit/s per channel. The LiNbO3 MZMs based external modulation requires relatively large 9.5 V switching voltage, [41] which is impractical to integrate. In 2015, there has been a demonstration of 2 µm InP based MZM with data rate of 10Gbit/s. [71] A 4-channel system is shown with 40Gb/s data rate, where the newly developed InP MZM replaces the LiNbO3 counterpart [72]. Although the InP MZM is significantly more compact than $LiNbO_3$ devices, it still lacks CMOS compatibility.

Chapter 3

Silicon Modulators Fundamentals

An electro-opto modulator is a device which modulates optical signal based on the information of a electrical signal. High speed modulator which modulates the signal efficiently in high bit rate is an essential element in telecommunication applications. Together with detector they compose the core of a data transceiver. Various building blocks of a silicon modulator is introduced in the chapter.

3.1 Passive components in silicon modulator

Passive devices in silicon photonics generally refer to those do not interact with electrical signal and perform functions involving optical signal only. Here we look into a selection of such devices which are used as building blocks of active devices such as modulators.

3.1.1 Multimode Interferometer (MMI)

An multimode interferometer (MMI) is a compact device consisting of a planar multi-mode free-propagating waveguide and several input/ouput ports accessing the multi-mode waveguide at front and end faces. In 1995, Lucas et al. published a comprehensive analytical model of MMI devices [73], which has later been realised on SOI platform including devices in the longer MIR wavelength regime [74, 75]. The multimode waveguide will allow a continuum of waveguide modes to propagate in the multimode region. A signal from the input waveguide

into the multimode region will propagate as a linear combination of those continuum of multiple modes. As a consequence of interference among those modes, the single or multiple images will appear periodically in the multimode region. Full details of MMI theory is elaborated in the Appendix A.

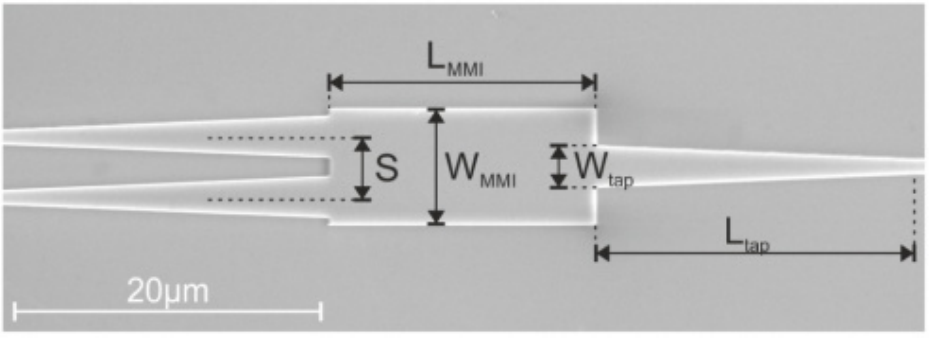

Figure 3.1: A typical 1x2 MIR MMI image with tapered input/output port. W_{tap} is the tapered I/O waveguide width, L_{MMI} is the multimode waveguide length, W_{MMI} is the multimode waveguide width, S is the port spacing. After [74]

Refer to Appendix A the N-fold self-imaging condition is given by [73]:

$$L_{MMI} = \frac{4Nn_{eff}W_{MMI}^2}{\lambda} \tag{3.1}$$

Where N is the order of self-imaging, L_{MMI} is the multimode waveguide length, W_{MMI} is the multimode waveguide width, λ is the input frequency, n_{eff} is the effective refractive index in the multimode region.

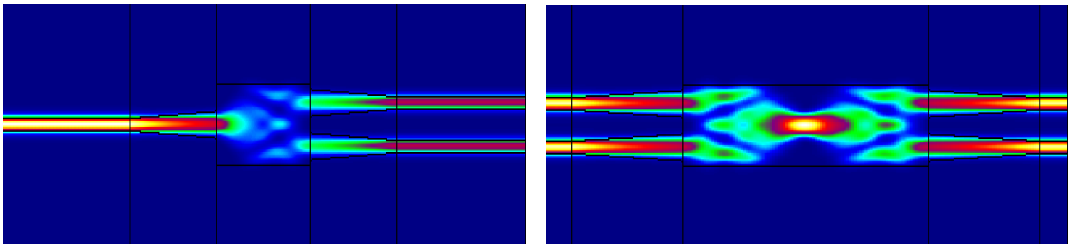

(a) 1x2 MMI (b) 2x2 MMI

Figure 3.2: Example of MIR 1x2 MMI act as power splitter and 2x2 MMI as a 3dB coupler. They can be used in MZI structure as couplers.

Thus by appropriately selecting multimode region length and I/O port position, various combinations of power splitting or combining can be achieved. As we can see in the case of 3.2(a) where the 1x2 MMI splits power evenly into two portions. While in 2x2 MMI the output ports are positioned at the 2-fold self-imaging position, therefore even only one of the input is excited, both output

ports will see the self images. This hence acts as a 3 dB coupler. Due to its compactness and very low loss, the MMI is widely adopted as coupler in Mach-Zehnder interferometer (MZI) or as general power splitter/combiner. The 1x2 power splitter MMI is often a quarter the length of the 2x2 3dB coupler MMI, detailed analysis are discussed in Appendix A.1.1 and Appendix A.1.2.

The bandwidth of a MMI has been approximated analytically in Appendix A.2. For a criterion of 0.5 dB excessive loss due to the wavelength shift, the bandwidth is

$$2|\delta\lambda| \approx \frac{\pi w_0^2 \lambda_c}{8NW_{MMI}^2} \quad \text{for excessive loss of 0.5 dB} \tag{3.2}$$

3.1.2 Mach-Zehnder Interferometers (MZI)

Mach-Zehnder Interferometer conveniently converts phase variation into intensity variation. In a MZI, input light is splitted evenly into two portions and then travels through two separate arms and finally recombine and interfere with each other. Since light signal in two arms is coherent, the difference in optical path length between to arms will produce interference pattern at the output. If the signals are in phase, they will interfere constructively and gives maxima output; if in anti-phase, it will interfere destructively and gives minima output.

3.1.2.1 1x1 MZI

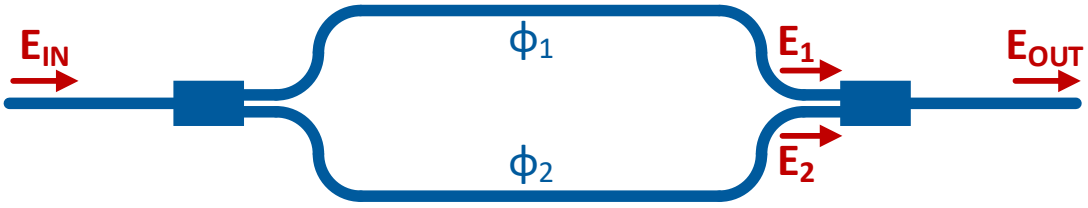

Figure 3.3: Schematic representation of a 1x1 MZI with 1x2 MMI as spitter and combiner.

Figure 3.3 shows a schematic example 1x1 MZI which can be used in a modulator to convert phase modulation produced by phase shifter into amplitude modulation. The power spitter and combiner are often realised using Y-junctions or 1x2 MMIs. We will then perform a analytical analysis, to find out the transfer function of a 1x1 MZI. The light intensity in the output waveguide of a MZI against the light

intensity in the input waveguide is

$$\frac{I_{OUT}}{I_{IN}} = \frac{\langle S_{OUT}\rangle}{\langle S_{IN}\rangle} \tag{3.3}$$

$$= \frac{E_{OUT} \times H_{OUT}}{E_{IN} \times H_{IN}} \tag{3.4}$$

$$= \frac{S_0 E_{OUT}^2}{S_0 E_{IN}^2} \tag{3.5}$$

$$= \left(\frac{E_{OUT}}{E_{IN}}\right)^2 \tag{3.6}$$

where $\langle S\rangle$ is the time averaged Poynting vector and $S_0 = \sqrt{\frac{\epsilon}{\mu}}$. Therefore we only need to know the ratio of $\frac{E_{OUT}}{E_{IN}}$ to find out the transfer function of the MZI.

Assume a perfect 50%-50% power splitter and combiner, the electric field on each arm right before the recombination point can be formalized as,

$$E_1 = \tfrac{1}{\sqrt{2}} E_{IN} \tau_1 e^{j(\omega t - \phi_1)} \tag{3.7}$$

$$E_2 = \tfrac{1}{\sqrt{2}} E_{IN} \tau_2 e^{j(\omega t - \phi_2)} \tag{3.8}$$

where E_{IN} is from the light in the input waveguide, τ is the optical loss on each arm, ϕ is the overall phase shift on each arm. For an arm with arm length of L_i and average waveguide propagation constant beta β_i,

$$\phi_i = \beta_i L_i \tag{3.9}$$

To put thing together, we can represent the MZI response as a transfer matrix

$$E_{OUT} = M_{1\times 1MZI} \cdot E_{IN} \tag{3.10}$$

And refer back to equation 3.7 and 3.8,

$$M_{1\times 1MZI} = \begin{bmatrix} \frac{1}{\sqrt{2}} & \frac{1}{\sqrt{2}} \end{bmatrix} \begin{bmatrix} \tau_1 e^{j(\omega t - \phi_1)} & 0 \\ 0 & \tau_2 e^{j(\omega t - \phi_2)} \end{bmatrix} \begin{bmatrix} \frac{1}{\sqrt{2}} \\ \frac{1}{\sqrt{2}} \end{bmatrix} \tag{3.11}$$

$$= \tfrac{1}{2}[\tau_1 e^{j(\omega t - \phi_1)} + \tau_2 e^{j(\omega t - \phi_2)}] \tag{3.12}$$

The transfer function can then be find as the ratio of output and input intensity,

$$\begin{aligned}\frac{I_{OUT}}{I_{IN}} &= \left(\frac{E_{OUT}}{E_{IN}}\right)^2 \\ &= \tfrac{1}{4}[\tau_1 e^{j(\omega t-\phi_1)} + \tau_2 e^{j(\omega t-\phi_2)}] \cdot [\tau_1 e^{j(\omega t-\phi_1)} + \tau_2 e^{j(\omega t-\phi_2)}]^* \\ &= \tfrac{1}{4}[\tau_1 e^{j(\omega t-\phi_1)} + \tau_2 e^{j(\omega t-\phi_2)}] \cdot [\tau_1 e^{-j(\omega t-\phi_1)} + \tau_2 e^{-j(\omega t-\phi_2)}] \\ &= \tfrac{1}{4}[\tau_1^2 + \tau_2^2 + \tau_1\tau_2 e^{j(\phi_1-\phi_2)} + \tau_1\tau_2 e^{j(\phi_2-\phi_1)}] \\ &= \tfrac{1}{4}[\tau_1^2 + \tau_2^2 + 2\tau_1\tau_2\cos(\phi_1-\phi_2)] \end{aligned} \tag{3.13}$$

Assume no loss in waveguide, $\tau_1 = \tau_2 = 1$,

$$\frac{I_{OUT}}{I_{IN}} = \tfrac{1}{2}[1 + \cos(\phi_1 - \phi_2)] \tag{3.14}$$

$$= \cos^2\left(\frac{\phi_1 - \phi_2}{2}\right) \tag{3.15}$$

$$= \cos^2\left(\frac{\Delta\phi}{2}\right) \tag{3.16}$$

The transfer function of an 1x1 MZI is therefore sinusoidal and it is dependent on the phase difference $\Delta\phi$ between two arms. According to equation 3.9, $\Delta\phi$ can be represented as $\beta_1 L_1 - \beta_2 L_2$.

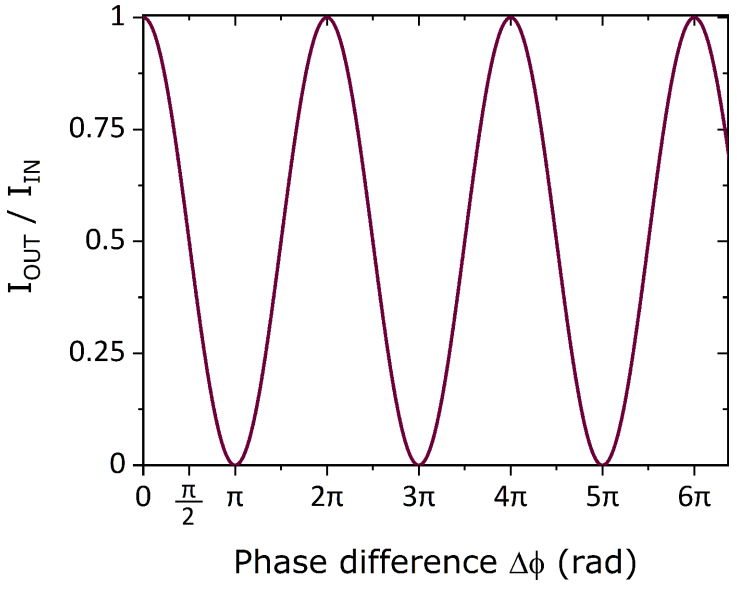

Figure 3.4: The normalised transfer function of an 1x1 MZI.

3.1.2.2 1x2 MZI

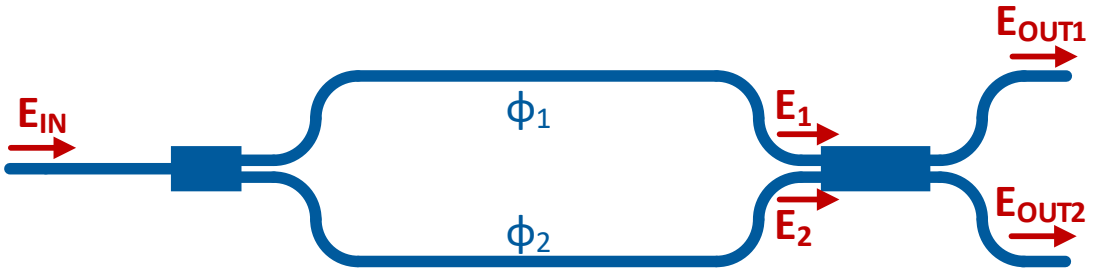

Figure 3.5: Schematic representation of a 1x2 MZI with 1x2 MMI as spitter and a 2x2 3 dB coupler at output.

In a 1x2 MZI, as shown in Figure 3.5, the input light is split evenly by a splitter and a 2x2 3dB coupler is used to produce two outputs. The 2x2 3dB coupler are often realised by a 2x2 MMI or a directional coupler. The transfer matrix of a 1x2 MZI response is defined as,

$$\begin{bmatrix} E_{OUT1} \\ E_{OUT2} \end{bmatrix} = M_{1\times 2MZI} \cdot E_{IN} \tag{3.17}$$

$$M_{1\times 2MZI} = \begin{bmatrix} \frac{1}{\sqrt{2}} & -\frac{1}{\sqrt{2}} \\ \frac{1}{\sqrt{2}} & \frac{1}{\sqrt{2}} \end{bmatrix} \begin{bmatrix} \tau_1 e^{j(\omega t-\phi_1)} & 0 \\ 0 & \tau_2 e^{j(\omega t-\phi_2)} \end{bmatrix} \begin{bmatrix} \frac{1}{\sqrt{2}} \\ \frac{1}{\sqrt{2}} \end{bmatrix} \tag{3.18}$$

$$= \frac{1}{2} \begin{bmatrix} \tau_1 e^{j(\omega t-\phi_1)} - \tau_2 e^{j(\omega t-\phi_2)} \\ \tau_1 e^{j(\omega t-\phi_1)} + \tau_2 e^{j(\omega t-\phi_2)} \end{bmatrix} \tag{3.19}$$

Therefore,

$$\begin{bmatrix} E_{OUT1} \\ E_{OUT2} \end{bmatrix} = \begin{bmatrix} \frac{1}{2}\left(\tau_1 e^{j(\omega t-\phi_1)} - \tau_2 e^{j(\omega t-\phi_2)}\right) \\ \frac{1}{2}\left(\tau_1 e^{j(\omega t-\phi_1)} + \tau_2 e^{j(\omega t-\phi_2)}\right) \end{bmatrix} \tag{3.20}$$

The intensity ratio,

$$\begin{aligned} \frac{I_{OUT1}}{I_{IN}} &= \left(\frac{E_{OUT1}}{E_{IN}}\right)^2 \\ &= \tfrac{1}{4}[\tau_1 e^{j(\omega t-\phi_1)} - \tau_2 e^{j(\omega t-\phi_2)}] \cdot [\tau_1 e^{j(\omega t-\phi_1)} - \tau_2 e^{j(\omega t-\phi_2)}]^* \\ &= \tfrac{1}{4}[\tau_1 e^{j(\omega t-\phi_1)} - \tau_2 e^{j(\omega t-\phi_2)}] \cdot [\tau_1 e^{-j(\omega t-\phi_1)} - \tau_2 e^{-j(\omega t-\phi_2)}] \\ &= \tfrac{1}{4}[\tau_1^2 + \tau_2^2 - \tau_1\tau_2 e^{j(\phi_1-\phi_2)} - \tau_1\tau_2 e^{j(\phi_2-\phi_1)}] \\ &= \tfrac{1}{4}[\tau_1^2 + \tau_2^2 - 2\tau_1\tau_2 \cos(\phi_1 - \phi_2)] \end{aligned} \tag{3.21}$$

And similarly to equation 3.13,

$$\frac{I_{OUT2}}{I_{IN}} = \left(\frac{E_{OUT2}}{E_{IN}}\right)^2 = \tfrac{1}{4}[\tau_1^2 + \tau_2^2 + 2\tau_1\tau_2\cos(\phi_1 - \phi_2)] \tag{3.22}$$

Assume no loss in waveguide, $\tau_1 = \tau_2 = 1$,

$$\frac{I_{OUT1}}{I_{IN}} = \tfrac{1}{2}[1 - \cos(\phi_1 - \phi_2)] \tag{3.23}$$

$$= \sin^2\left(\frac{\phi_1 - \phi_2}{2}\right) \tag{3.24}$$

$$= \sin^2\left(\frac{\Delta\phi}{2}\right) \tag{3.25}$$

$$\frac{I_{OUT2}}{I_{IN}} = \tfrac{1}{2}[1 + \cos(\phi_1 - \phi_2)] \tag{3.26}$$

$$= \cos^2\left(\frac{\phi_1 - \phi_2}{2}\right) \tag{3.27}$$

$$= \cos^2\left(\frac{\Delta\phi}{2}\right) \tag{3.28}$$

3.1.2.3 2x2 MZI

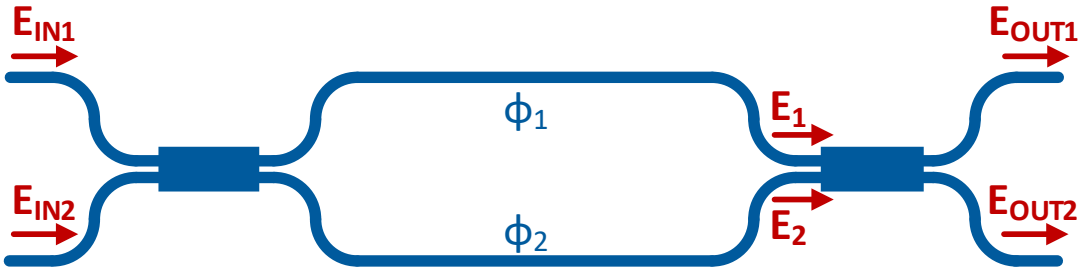

Figure 3.6: Schematic representation of a 2x2 MZI with two 2x2 MMI as 3 dB couplers to provide four ports.

The 2x2 MZI contains four ports and comprises two 2x2 3dB couplers. The transfer matrix is given as,

$$\begin{bmatrix} E_{OUT1} \\ E_{OUT2} \end{bmatrix} = M_{1\times 2MZI} \cdot \begin{bmatrix} E_{IN1} \\ E_{IN2} \end{bmatrix} \tag{3.29}$$

$$M_{2\times 2MZI} = \begin{bmatrix} \frac{1}{\sqrt{2}} & -\frac{1}{\sqrt{2}} \\ \frac{1}{\sqrt{2}} & \frac{1}{\sqrt{2}} \end{bmatrix} \begin{bmatrix} \tau_1 e^{j(\omega t-\phi_1)} & 0 \\ 0 & \tau_2 e^{j(\omega t-\phi_2)} \end{bmatrix} \begin{bmatrix} \frac{1}{\sqrt{2}} & -\frac{1}{\sqrt{2}} \\ \frac{1}{\sqrt{2}} & \frac{1}{\sqrt{2}} \end{bmatrix} \tag{3.30}$$

$$= \frac{1}{2} \begin{bmatrix} \tau_1 e^{j(\omega t-\phi_1)} - \tau_2 e^{j(\omega t-\phi_2)} & -\tau_1 e^{j(\omega t-\phi_1)} - \tau_2 e^{j(\omega t-\phi_2)} \\ \tau_1 e^{j(\omega t-\phi_1)} + \tau_2 e^{j(\omega t-\phi_2)} & -\tau_1 e^{j(\omega t-\phi_1)} + \tau_2 e^{j(\omega t-\phi_2)} \end{bmatrix} \tag{3.31}$$

Assume the there is only light from one input,

$$\begin{bmatrix} E_{IN1} \\ E_{IN2} \end{bmatrix} = \begin{bmatrix} 1 \\ 0 \end{bmatrix} \tag{3.32}$$

Then,

$$\begin{bmatrix} E_{OUT1} \\ E_{OUT2} \end{bmatrix} = \begin{bmatrix} \frac{1}{2}\left(\tau_1 e^{j(\omega t-\phi_1)} - \tau_2 e^{j(\omega t-\phi_2)}\right) \\ \frac{1}{2}\left(\tau_1 e^{j(\omega t-\phi_1)} + \tau_2 e^{j(\omega t-\phi_2)}\right) \end{bmatrix} \tag{3.33}$$

This is similar to the case of a 1x2 MZI, and assuming lossless waveguide, the intensity ratio is then given as,

$$\frac{I_{OUT1}}{I_{IN}} = \sin^2\left(\frac{\phi_1 - \phi_2}{2}\right) \tag{3.34}$$

$$= \sin^2\left(\frac{\Delta\phi}{2}\right) \tag{3.35}$$

$$\frac{I_{OUT2}}{I_{IN}} = \cos^2\left(\frac{\phi_1 - \phi_2}{2}\right) \tag{3.36}$$

$$= \cos^2\left(\frac{\Delta\phi}{2}\right) \tag{3.37}$$

3.1.2.4 Free Spectral Range (FSR) of an MZI

In an unbalanced MZI, the optical path length of two arms are different either by varying effective refractive index or varying physical length or both. Such unbalanced design makes the MZI an comb frequency filter with squared sinusoidal frequency response. The transfer function become a function of wavelength. To find out the free spectral range (FSR) of an unbalanced MZI, we need to revisit the wave propagation in a waveguide.

$$E = E_0 e^{j(\omega t-\beta' z)} \tag{3.38}$$

where the complex propagation constant $\beta' = \dfrac{2\pi \cdot n_{eff}(\lambda)}{\lambda} - i \cdot \dfrac{\alpha}{2}$.

To find out the wave propagation velocity, we only need to investigate the oscillation part,

$$E = E_0 e^{j(\omega t - \beta z)} \tag{3.39}$$

where the propagation constant $\beta = \dfrac{2\pi \cdot n_{eff}(\lambda)}{\lambda}$. By also applying

$$\omega = 2\pi f = 2\pi \cdot \frac{c}{\lambda} \tag{3.40}$$

The phase velocity which is the propagation velocity of the carrier wave,

$$v_{ph}(\lambda) = \frac{\omega}{\beta} = \frac{c}{n_{eff}(\lambda)} \tag{3.41}$$

The group velocity which is the propagation velocity of the signal,

$$v_g(\lambda) = \frac{d\omega}{d\beta} = \Big(\frac{d\beta}{d\omega}\Big)^{-1} \tag{3.42}$$

$$= c\Big[\frac{d}{d\frac{1}{\lambda}}\frac{n_{neff}(\lambda)}{\lambda} \cdot (-\lambda^2)\Big]^{-1} \tag{3.43}$$

$$= c\Big[\frac{d}{d\lambda} n_{neff}(\lambda) \cdot (-\lambda^2)\Big]^{-1} \tag{3.44}$$

$$= c\Big[n_{neff}(\lambda) - \lambda\Big(\frac{d}{d\lambda} n_{neff}(\lambda)\Big)\Big]^{-1} \tag{3.45}$$

$$= \frac{c}{n_g} \tag{3.46}$$

where $n_g = n_{neff}(\lambda) - \lambda\Big(\dfrac{d}{d\lambda} n_{neff}(\lambda)\Big)$

The FSR is the wavelength difference of adjacent transfer function peaks. In an unbalanced MZI with arm difference of ΔL, assuming no other phase modulation,

$$FSR = \lambda_{m+1} - \lambda_m \tag{3.47}$$

Related back to equation 3.16, the adjacent peaks are spaced with π phase shift.

$$\begin{aligned}
\frac{\pi}{FSR} &= \frac{\frac{\phi(\lambda_{m+1})}{2} - \frac{\phi(\lambda_m)}{2}}{\lambda_{m+1} - \lambda_m} \\
\frac{1}{FSR} &= \frac{\Delta L}{2\pi} \frac{\beta(\lambda_{m+1}) - \beta(\lambda_m)}{\lambda_{m+1} - \lambda_m} \\
&\approx \frac{\Delta L}{2\pi} \cdot \frac{d\beta}{d\lambda} \\
&= \frac{\Delta L}{2\pi} \cdot 2\pi \Big[\frac{1}{\lambda} \frac{d}{d\lambda} n_{eff}(\lambda) - \frac{1}{\lambda^2} n_{eff}(\lambda) \Big] \\
&= \frac{\Delta L}{\lambda^2} n_g \qquad (3.48) \\
FSR &= \frac{\lambda^2}{\Delta L \cdot n_g} \qquad (3.49)
\end{aligned}$$

3.2 Electro-optical Modulation Mechanism in Silicon

There are various electro-optical effect one can use to conduct an electro-optical modulation. Such effects are categorised in two types, the applied electric signal induces change in refractive index is called electro-refractive modulation; and the applied electric signal induces change in absorption coefficient is called electro-absorptive modulation.

In conventional photonics, material such as $LiNbO_3$ are widely used for its strong linear electro-refractive Pockels effect, where the index change is proportional to the electrical field. Other field effect such as second order electro refractive Kerr effect, and electro absorption Franz-Keldysh effect and the quantum-confined Stark effect (QCSE) have all been exploited to making modulators. The effective effect is almost instantaneous and therefore highly advantageous in making high-speed devices. However according to Soref and Bennett [76] those handy electric field effects are either too weak or requires high voltage to take effect in pure silicon at telecommunication wavelengths.

Silicon however exhibits a strong thermal-optic effect. This is widely used to produce relatively slow modulator. Nedeljkovic et al. [54] has first realised a thermal-based SOI modulator working in MIR. The speed nevertheless is in kHz regime. The thermal effect is too slow for the usage in data communication applications.

The most widely used method to achieve modulation in silicon is plasma dispersion effect. The change in free carrier concentration (ΔN) in silicon can make changes in refractive index (Δn) and absorption coefficient ($\Delta\alpha$). The refractive index (n) and absorption coefficient (α) are inter-related, in fact they the the manifestation of real (n) and imaginary (k) part of complex refractive index. Where $\alpha = 4\pi k/\lambda$. n and k are coupled together by Kramers-Kronig dispersion relations, therefore change in one will result change in another.

Drude-Lorenz equation predicts [77] the response from underlying physics but it coincides with the actual results only partially. However Soref and Bennett [76] semi-empirically produced equations that later proved to agree with the experiment results very well. Therefore those equations are generally adopted as a guideline to the designs for almost all later modulator designs in telecommunication wavelength. Only 1300 nm and 1550 nm wavelength are analysed, and the equations are given bellow: [76]

For $\lambda = 1550nm$:

$$\Delta n = \Delta n_e + \Delta n_h = -[8.8 \times 10^{-22} \times \Delta N_e + 8.5 \times 10^{-18} \times (\Delta N_h)^{0.8}] \quad (3.50)$$

$$\Delta\alpha = \Delta\alpha_e + \Delta\alpha_h = 8.5 \times 10^{-18} \times \Delta N_e + 6.0 \times 10^{-18} \times \Delta N_h \quad (3.51)$$

For $\lambda = 1300nm$:

$$\Delta n = \Delta n_e + \Delta n_h = -[6.2 \times 10^{-22} \times \Delta N_e + 6.0 \times 10^{-18} \times (\Delta N_h)^{0.8}] \quad (3.52)$$

$$\Delta\alpha = \Delta\alpha_e + \Delta\alpha_h = 6.0 \times 10^{-18} \times \Delta N_e + 4.0 \times 10^{-18} \times \Delta N_h \quad (3.53)$$

where Δn_e is the change in real refractive index resulting from change in free electron carrier concentration; Δn_h is the change in real refractive index resulting from change in free hole carrier concentration; $\Delta\alpha_e$ is the change in absorption coefficient resulting from change in free electron carrier concentration; $\Delta\alpha_h$ is the change in absorption coefficient resulting from change in free hole carrier concentration; ΔN_e is the change in free electron carrier concentration; ΔN_h is the change in free hole carrier concentration. Compared to the weak field effects in Silicon, carriers effect are efficient enough for practical modulators. The speed although still lag behind the the almost instantaneous field effect, is able to produce devices achieving tens of gigahertz bandwidth.

On silicon platform, in addition to plasma dispersion effect, researchers have also explored Pockels effect with strained silicon [78], Kerr effect with silicon nanocrystals [79], and Franz-Keldysh effect with SiGe [80, 81].

3.3 PN junction silicon phase shifters

In carrier effect phase shifter, phase change are generated by either introduce or reject free carrier from the waveguide region. The phase shifter is then incorporated into an MZI or ring resonator to convert phase change into amplitude change. There are mainly three types of phase shifter structures namely carrier injection, carrier accumulation and carrier depletion.

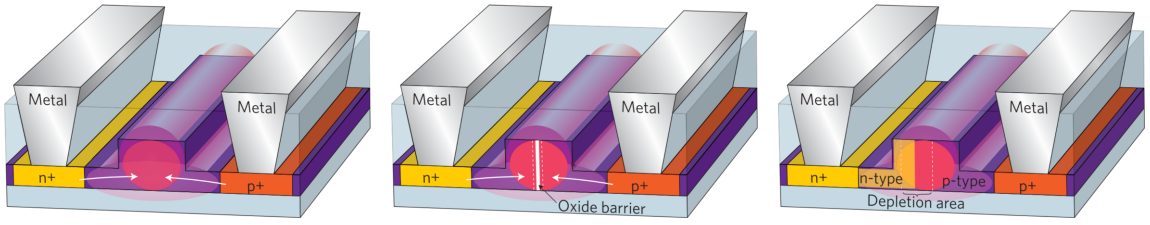

(a) Carrier injection type.

(b) Carrier accumulation type.

(c) Carrier depletion type.

Figure 3.7: Schematic of typical phase shifter structures based on plasma dispersion effect. After [82]

The carrier injection device is based on a PiN diode. As shown on Figure 3.7(a), the intrinsic part coincides with the waveguide core and highly doped p+ and n+ region are lying on the slab region of the waveguide. During operation, the forward bias is applied and free carriers are injected into the intrinsic junction region. Due to this large injection current, the the modulation efficiency can reach a very decent high level. However, due to the constant current flow at on state, it is not energy efficient compare to the other two types. Moreover, the device speed is limited by the carrier generation and recombination rate. By adopting pre-emphasis electric driving signal, 10 Gbit/s has been achieved by MZI type [83, 84] and 18 Gbit/s by ring modulator [85]. However the pre-emphasis driving signal requires complicated driver system and it is not very power efficient.

Carrier accumulation device incorporated a thin dielectric layer between p-type and n-type (Figure 3.7(b)). The free carriers can be accumulated around the dielectric wall. It essentially forms a metal-oxide-semiconductor (MOS) capacitor. The MOS capacitor phase shifter has a potential to be very modulation efficient.

For such device, since it does not involve carrier recombination, their speed is essentially mainly limited by device resistance and capacitance [82]. The fabrication of accumulation type of device is rather complex owing to the thin insulation layer. It is challenging to growing signal crystal silicon on top of the thin insulation layer due to the lacking of proper seed. Intel addressed this issue by laterally grow the upper signal crystal silicon layer using the seed on the side [86]. Using similar fabrication technique, Cisco has demonstrated 40Gb/s bitrate [87]. The first vertical-walled insulator MOS capacitor has been published to provide 25 Gbit/s datarate [88].

Gardes et al. proposed carrier depletion in 2005. Shown in Figure 3.7(c), the device consists a PN junction. Instead of inject carriers, it operates at reverse bias and reject free carriers to create a carrier concentration variation. Carrier depletion device does not limited by carrier recombination rate, therefore it has a potential to reach very high bitrate. It is relatively easier to fabricate than accumulation device and a plethora of designs have emerged. Intel reported the first carrier depletion device working at 30 Gbit/s [89]. Later Thomson et al. achieved 50 Gbit/s bitrate [90]. Numerous optimised design has published so far with speed ranging among tens of Gbit/s. A selection of c-band silicon MZM with data rate above 40Gbit/s is shown in Table 3.1. The popularity of the depletion type and the impressive performance achieved so far proved a promising potential of carrier depletion mechanism.

Table 3.1: A selection of c-band silicon Mach-Zehnder modulators with travelling wave electrode design. No slow light or other multiple-pass designs included.

Ref	$\mathbf{V_\pi \cdot L_\pi}$	**EO bandwidth**	**Modulation format**	**Data Rate**	**Length**
2015 [91]	3.2 V·cm	41 GHz	PAM 4	112Gb/s	4.25 mm
2015 [92]	3.57 V·cm	35 GHz	PAM 4	112Gb/s	4.2 mm
2017 [93]	-	30.2 GHz	PAM 4	64Gb/s	2 mm
2014 [94]	2.4 V·cm	55 GHz	OOK	70Gb/s	-
2014 [95]	2.43 V·cm	30 GHz	OOK	40Gb/s	3 mm
2014 [96]	1.93 V·cm	27 GHz	OOK	40Gb/s	3.5 mm
2014 [97]	2.2 V·cm	26 GHz	OOK	40Gb/s	0.95 mm
2014 [98]	1.85 V·cm	37 GHz	OOK	50.5Gb/s	3 mm
2012 [99]	2.2 V·cm	25.6 GHz	OOK	50.1Gb/s	4 mm
2012 [100]	2.4 V·cm	>20 GHz	OOK	50Gb/s	2 mm
2012 [90]	2.8 V·cm	>40 GHz	OOK	50Gb/s	1 mm

3.4 Modulator Performance Criteria

To assess the performance of a modulator there are several criteria to consider [82, 47]:

Modulation speed is characterised by either electro-optic bandwidth (in GHz) or in modulation data rate (in Gbit/s). According to Nyquist theorem, in an ideal OOK the data rate should be 2x of the bandwidth, however in practice, it is almost always below 2. An eye diagram is often used to demonstrate the working speed of an device.

Modulator loss consists various sources such as absorption of free carriers in the doped region. It also consists loss from passive optical components as well as contributions from metal electrode.

Modulator power consumption is often measured in energy per bit. Some temperature sensitive device such as ring modulator may require thermal stabiliser. The power consumption of such peripherals should also be taken account of.

Modulation extinct ratio also referred as modulation depth measures the ratio between maximum intensity and minimum intensity produced by modulator. Higher the extinct ratio normally implies better bit error rate.

Device footprint is vital if considering a full integration with CMOS technology. Mach-Zehnder devices are generally larger especially in one dimension, the length, than the ring modulator.

Optical bandwidth or spectral bandwidth refers to the wavelength range an modulator is able to working without tuning. The resonant-based ring modulators normally operate within 1 nm, whereas MZI based modulator is able to operate at much wider.

Temperature sensitivity is an issue in silicon based devices as silicon exhibits large thermo-optical effect. Ring resonator is particularly susceptible to temperature variation, while MZI based structure since the temperature affect both arm the thermal effect is almost cancelled in MZI.

Chirp refers to signal with a temporal increase or decrease in frequency. In the context of modulator, it is manifested as residual phase modulation as the amplitude modulates. Commercial silicon photonics transceiver (1310 nm) are currently used mostly in relatively short-link applications. However as the performance of

silicon photonics device progressing, and with the introduction of 2 µm telecommunication window one may expect silicon based device to be used in long-haul applications. In that case, chirp may become an important criterion for long-haul high-speed transmission.The plasma dispersion based MZM for example, even on a pull-push driving scheme, will still show residue chirp[1].

3.5 Comparison of common types of silicon optical modulators

An summarised comparison of three common types of modulator is given below.

Table 3.2: Comparison of three types of silicon optical modulators.

Type	**Footprint**	**Spectral BW**	**Thermal stability**	**Power Consumption**
MZM	Large (∼1mm)	Broadband	Highly Robust	Large dynamic power
MRM	Compact (∼5µm)	Narrow (<1nm)	Sensitive (<1K)	Low dynamic power (1Vpp)
EAM	Compact (∼60µm)	Middle (<30nm)	Insensitive (<30K)	Low dynamic power (2Vpp)

A micro ring modulator (MRM) contains a similarly structured phase shifter as in MZM. The phase shifter incorporated as part of a ring resonator. Light therefore travels multiple passes (proportional to the Q factor) in the ring as well the the phase shifter. Resulting a much more compact design compared to MZM. Due to its small footprint, it can often be treated as a lump model in electrode design and requires less driving power. However the being a resonant device means a fairly narrow spectral bandwidth and very sensitive to ambient temperature. The whole ring modulator package normally comes with an active temperature control system, which may draw significant power.

Another candidate is the Electro-absorption Modulator (EAM), which resorts to Franz–Keldysh effect in GeSi. By tuning the composition of the two element, one can effectively place the absorption edge into the telecommunication window. The edge is also responsible to electric field, hence the absorption-type modulation. If

[1]For a Pockels effect based MZM the chirp can be theoretically eliminated by pull-push drive both arm with complementary signal. In this case the phase of each arm is always equal and opposite, and according to equation (6.2), the phase of the output will stay constant. However for a plasma dispersion effect based MZM, even the phase from both arm are cancelled using similar method, because each arm are of different free carrier concentration instantaneously, the resulting residue loss imbalance will contribute to the output signal phase change, hence the chirp.

can offer high efficiency and small footprint and hence lumped model and lower power consumption. However due to absorption edge, the spectral bandwidth is limited to around 30 nm.

3.6 Mach-Zehnder Modulator (MZM)

A Mach-Zehnder Modulator (MZM) uses Mach-Zehnder Interferometer (MZI) to converts phase variation into intensity variation. It usually incorporates a phase shift on one arm or both arms. In silicon photonics we can use one of the above-mentioned PN junction phase shifter design, namely carrier injection, carrier accumulation and carrier depletion. Due to the non-resonant nature of the device, it often requires mm level of phase shifter length, and hence is often paired with a travel-wave electrode. The MZI hence consumes relatively large drive power. But since MZM is a non-resonant device, it provides unparalleled wide spectral bandwidth.

The phase shift of a phase shifter is positively correlated to drive voltage and almost linearly proportional to the phase shifter length.

$$\Delta\phi_{ps} = \int_0^{L_{ps}} [k(V_{ps}) - k(0)]\,\mathrm{d}x \tag{3.54}$$

$$= \frac{2\pi}{\lambda_0} \int_0^{L_{ps}} \Delta n_{eff}(V_{ps})\,\mathrm{d}x \tag{3.55}$$

for DC regime or lumped model,

$$\Delta\phi_{ps} = \frac{2\pi \cdot \Delta n_{eff}(V_{ps}) \cdot L_{ps}}{\lambda_0} \tag{3.56}$$

where λ_0 is the centre operation optical wavelength, $\Delta\phi_{ps}$ is the phase change due to the phase shifter, V_{ps} is the drive voltage of the phase shifter and L_{ps} is the length of the phase shifter, $k(V_{ps})$ and $k(0)$ are wavenumbers with V_{ps} applied and without any voltage applied respectively. When the phase shift reaches π, the light output in theory should reach zero. This is because the signal in the modulation arm invert itself and destructively interfere with the other arm in an MZI to produce zero intensity at the output. For a given length of the phase shifter, we define L_π as the device length required to shift the the phase by π for a given voltage, V_π. Assume the phase shifter modulation strength scales linearly

with its length,

$$\frac{L_{ps}}{L_\pi} = \frac{\Delta\phi_{ps}}{\pi} \tag{3.57}$$

$$L_\pi = \frac{\lambda_0}{2\Delta n_{eff}(V_\pi)} \tag{3.58}$$

If both phase shifter length and drive voltage are variables, the efficiency of a modulator is often quoted as the product of the two, ie $V_\pi \cdot L_\pi$. A lower such product value corresponds to a better modulation efficiency. In a push-pull configuration where phase shifters on both arms of an MZM are driven with differential signal, the effective $V_\pi \cdot L_\pi$ can ideally be halved.

Similarly, in a carrier depletion MZM case, assume the modulation strength scales linearly with reverse bias voltages, then

$$\frac{V_{ps}}{V_\pi} = \frac{\Delta\phi_{ps}}{\pi} \tag{3.59}$$

$$\Delta\phi_{ps} = \pi \cdot \frac{V_{ps}}{V_\pi} \tag{3.60}$$

According to MZI response from equation 3.16, the normalised MZM transfer function is,

$$\frac{I_{OUT}}{I_{IN}} = \cos^2\left(\frac{\Delta\phi_{ps}}{2}\right) \tag{3.61}$$

$$= \cos^2\left(\frac{\pi}{2} \cdot \frac{V_{ps}}{V_\pi}\right) \tag{3.62}$$

In commercial product, the MZM usually uses balanced MZI to maximize the spectral bandwidth. The both arm are of the same length and the transfer function has a almost flat response against wavelength. Therefore the transfer function of a balanced MZM become purely a function of drive voltage and independent of wavelength. During pure amplitude modulation operation it need to be thermally tune to the quadrature bias point (refer to figure 3.8) where the phase difference between the two arms are $\pi/2$ and the resulting amplitude modulation is large and linear. Coherent applications often operates at the null bias point, which is at the minima in the transmission function. This makes the amplitude modulation less linear and the overall optical output lower, but it offers phase inversion every time the drive voltage crosses the minimum transmission point (eg. essential for BPSK).

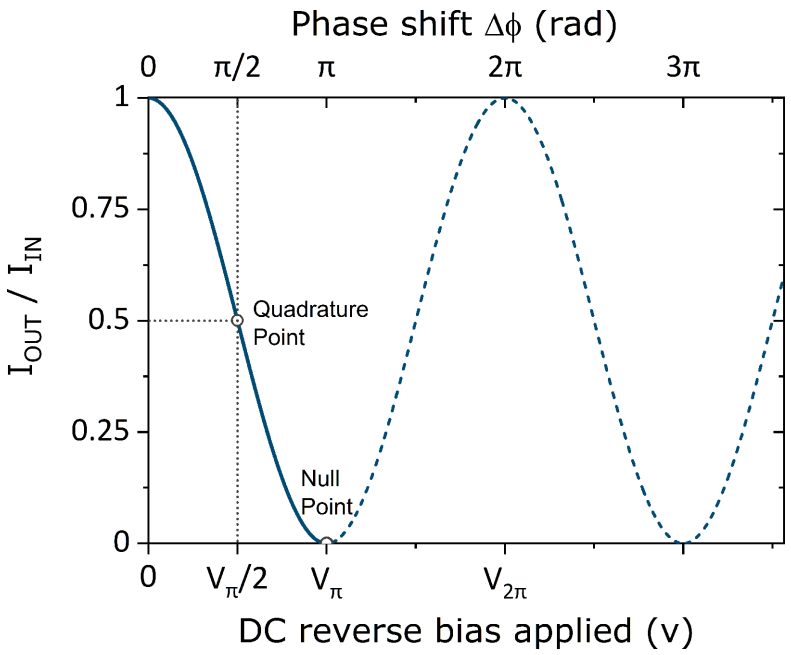

Figure 3.8: The normalised transfer function of an MZM against phase shift and DC reverse driving voltage.

In academia or in prototyping stage, the unbalanced MZI are preferred as it makes the characterisation easier. Since the unbalanced MZI has a sinusoidal response against wavelength, we can adjust the operation point of the modulator to the quadrature point by simply tune the wavelength of the laser. If choosing adequate FSR by tuning the arm length difference, the modulation can then be intuitively shown as peak shift compare to purely intensity drop. This helps to quickly locate the operation point of a modulator during the characterisation. It is especially helpful in distinguishing the negatively sloped and the positively sloped quadrature point.

3.7 Plasma dispersion effect of silicon in 2 µm band

Nedeljkovic et al. [49] later expand on the Soref and Bennett's work [76] and extend the wavelength range of the equations into 1.3 - 14 µm. Latest experimental data are adopted but similar method as Soref is used to calculate out the following

wavelength dependent equations: [49]

$$-\Delta n(\lambda) = \Delta n_e(\lambda) + \Delta n_h(\lambda) = p(\lambda) \times \Delta N_e^{q(\lambda)} + r(\lambda) \times \Delta N_h^{s(\lambda)} \tag{3.63}$$

$$\Delta\alpha(\lambda) = \Delta\alpha_e(\lambda) + \Delta\alpha_h(\lambda) = a(\lambda) \times \Delta N_e^{b(\lambda)} + c(\lambda) \times \Delta N_h^{d(\lambda)} \tag{3.64}$$

where a,b,c,d,p,q,r,s are coefficient that can be looked up in Table B.1 in Appendix B.

This work enables one to predict the plasma-dispersion-effect modulator behaviour in 2 µm and further beyond into MIR. By analysing the trend, we can see that below 3 µm, the phase shifter with MZI type of modulator is still feasible. By adopting carrier depletion, it is promising to make fast modulator working in 2 µm. However as wavelength increases, both Δn and $\Delta\alpha$ grows quickly. Above 3 µm, $\Delta\alpha$ become dominant in the overall response. It is more advisable to design a electro-absorption type of modulator in that wavelength range.

To understand the plasma dispersion effect difference between 2 µm and 1550 nm, I plug the coefficient back into the above equation,

$$\begin{aligned} -\Delta n(2\mu m) &= \Delta n_e(2\mu m) + \Delta n_h(2\mu m) \\ &= 1.91 \times 10^{-21} \times \Delta N_e^{0.992} + 2.28 \times 10^{-18} \times \Delta N_h^{0.841} \end{aligned} \tag{3.65}$$

$$\begin{aligned} \Delta\alpha(2\mu m) &= \Delta\alpha_e(2\mu m) + \Delta\alpha_h(2\mu m) \\ &= 3.22 \times 10^{-20} \times \Delta N_e^{1.149} + 6.21 \times 10^{-20} \times \Delta N_h^{1.119} \end{aligned} \tag{3.66}$$

$$\begin{aligned} -\Delta n(1.55\mu m) &= \Delta n_e(1.55\mu m) + \Delta n_h(1.55\mu m) \\ &= 5.40 \times 10^{-22} \times \Delta N_e^{1.011} + 1.53 \times 10^{-18} \times \Delta N_h^{0.838} \end{aligned} \tag{3.67}$$

$$\begin{aligned} \Delta\alpha(1.55\mu m) &= \Delta\alpha_e(1.55\mu m) + \Delta\alpha_h(1.55\mu m) \\ &= 8.88 \times 10^{-21} \times \Delta N_e^{1.167} + 5.84 \times 10^{-20} \times \Delta N_h^{1.109} \end{aligned} \tag{3.68}$$

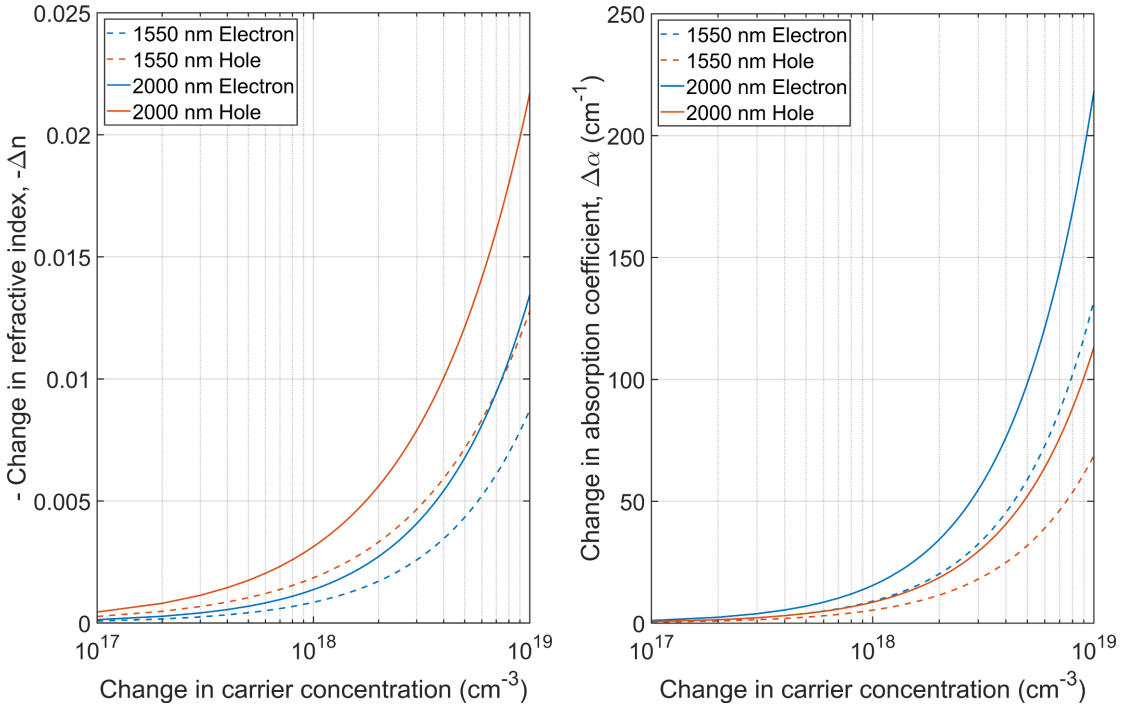

(a) The refractive index change against change in carrier concentrations.

(b) The absorption coefficient change against change in carrier concentrations.

Figure 3.9: Plasma dispersion effect in silicon at 1550 nm and 2000 nm wavelength, predicted by the semi-empirical equations.

Please note that new 1550 nm equations 3.67 and 3.68 shows a discrepancy to the original Soref equations 3.50 and 3.51. This is due to improve fitting method over the same data, where the original data was fit without a logarithm concentration, resulting a more weighted point towards the higher concentration points. We therefore only plot the new version of 1550 nm equations against 2 µm given in Figure 3.9. As we can see, 2 µm wavelength light has stronger interaction with both free electrons and holes in silicon than 1550 nm wavelength light, resulting a higher refractive change and high optical absorption. Furthermore, for both wavelengths, at the same change in concentration, free holes show higher impact in refractive change and free electrons correspond to larger absorption. In the actual PN junction phase shifter design, we may therefore want to bring the optical mode to interact more with the p-type doping to enhance the modulation efficiency and to reduce the loss.

3.8 State of the art high-speed 2 µm-band silicon modulators

Table 3.3: High-speed 2 µm-band silicon modulators including our works.

Ref	$V_\pi \cdot L_\pi$	Type &format	Datarate &ER	Loss	Length
2012 [50] IBM	1.2V·cm	Injection OOK	3Gb/s 8.9dB	9dB	1mm
2018 [101] This work 1	**2.68V·cm**	**Depletion OOK**	**20Gb/s 5.8dB**	**13dB**	**1.5mm**
2018 [101] This work 1	**4.4V·cm**	**Injection OOK**	**3Gb/s 2.3dB**	**-**	**Ring**
2018 [102] NTU	-	Depletion OOK	12.5Gb/s	3.2dB	1.5mm
2018 GFP McMaster	2.1V·cm	Depletion OOK	12.5Gb/s	-	Ring
2019 [103] This work 2	**2.89V·cm**	**Depletion OOK**	**25Gb/s 6.25dB**	**5.25dB**	**2mm**
2019 This work 2	**2.89V·cm**	**Depletion PAM4**	**25Gb/s**	**5.25dB**	**2mm**
2019 This work 2	**1.36V·cm**	**Depletion OOK**	**20Gb/s 0.8dB**	**3.9dB**	**0.5mm (Michelson)**

High-speed silicon modulator in 2 µm is scarce prior to our work. IBM, in 2012, have reported SOI carrier injection modulator operating at 2165 nm. Using pre-emphasis driving signal, the devices reaches 3 Gbit/s bitrate (Figure 3.10(a)) [50]. Our work that has published in 2018 has pushed the bar to 20 Gbit/s with a high-speed MZM. The result will be discussed in detail in the later chapters. In the same year, our collaborator NTU has demonstrated a 2 µm MZM working at 12.5 Gbit/s (Figure 3.10(b)) [102]. Collaborated with McMaster University, we have also tie the IBM's carrier injection record by demostrating a 3 Gbit/s silicon ring modulator at 2 µm as in Figure 3.10(c) [101]. Later McMaster has successfully run a 12.5 Gbit/s optical link consisting the same silicon ring under carrier depletion and silicon based defect detector. The eye diagram is shown in Figure 3.10(d). In 2019 I have characterised modulator optimized for 2 µm wavelength from a subsequent fabrication run. We have further pushed the limit of the detector and

achieved 25 Gb/s OOK and PAM4. In the meantime, addressed the issues of high insertion loss. And the results are the state of art to date. The table 3.3 compared all high-speed silicon modulator in the 2 µm wavelength band until 2019. I will elaborate the design and results of our work in the following chapter.

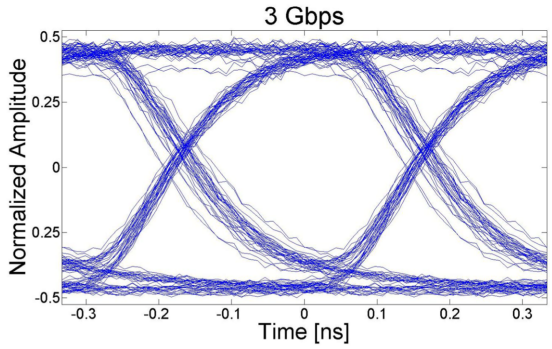

(a) IBM micro ring modulator in carrier injection. Data rate 3 Gbit/s at 2165 nm.

(b) NTU micro ring modulator in carrier depletion. Data rate 12.5 Gbit/s at 1973.2 nm. V_{bias} = -3 V, V_{p-p} = 6.0 V.

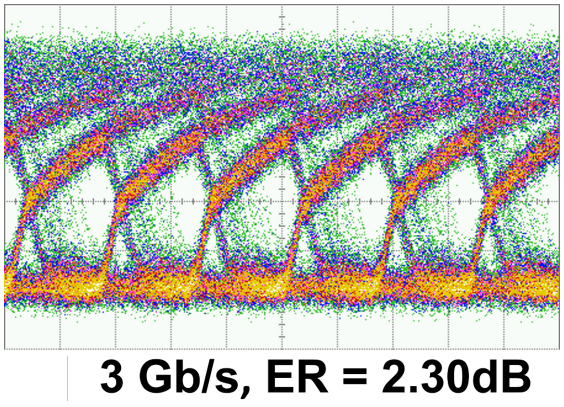

(c) McMaster, Southampton micro ring modulator in carrier injection. Data rate 3 Gbit/s at 1954 nm.

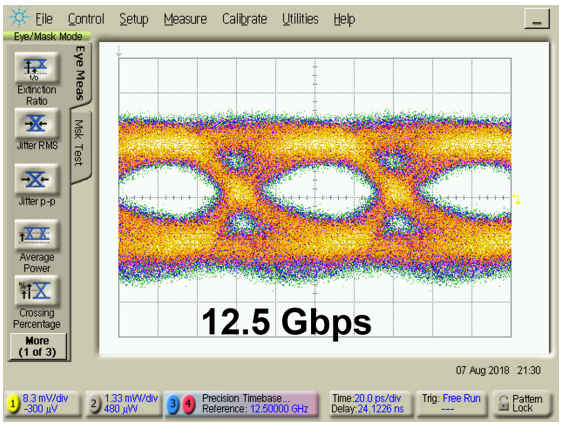

(d) McMaster micro ring modulator in carrier depletion. Data rate 12.5 Gbit/s at 1967.4 nm. V_{bias} = -2 V, V_{p-p} = 2.5 V.

Figure 3.10: Eye diagrams of silicon based high-speed 2 µm modulators from the literature.

Chapter 4

Methodology — Design a High-Speed 2 µm Si Modulator

4.1 Passive optical building blocks at 2 µm

A stronger plasma dispersion at 2 µm wavelengths compare to 1550nm makes the designing of highly efficient modulator seemingly easy. Transiting from 1550 nm into 2 µm wavelengths, however are associated implications. Most results from the physically larger optical mode size due to longer wavelength. On a 220nm SOI platform, the 2 µm mode is less confined and As a result, it will have larger bend loss and is more prone to substrate leakage. The mode also likely has more evanescent interaction with surroundings, thus anything with high optical absorption will need to placed further away from the waveguide. The longer wavelength also implies longer coupling interaction length and longer phase shifter device for a π phase shift. There is one advantage however, the surface scattering is reduced with a longer wavelength. Since surface roughness is a major contributor to optical loss in silicon photonics, we should expect decently low loss waveguide.

To investigate the single mode cut-off condition of longer wavelengths on 220 nm SOI platform, we use Lumercial mode solutions to calculate optical mode conditions for various waveguide widths. According to the simulation scan in figure 4.1(c), at 1950 nm, the rib waveguide is single mode for widths up to 650 nm. However, as the waveguide width gets narrower, the mode becomes less confined and this can reduce the efficiency of a modulator. 600 nm waveguide width is a preferable choice at 2 µm and it is used in our ring modulator design; while at

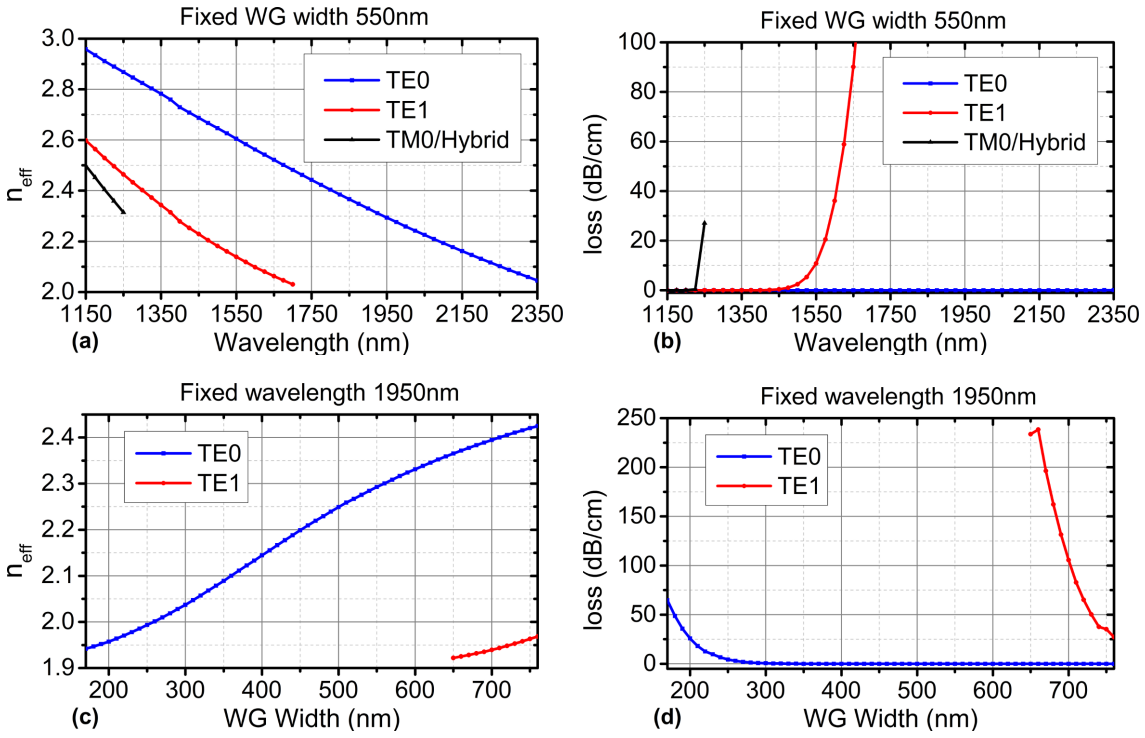

Figure 4.1: Mode analysis of a rib waveguide in the 220 nm SOI platform with 90 nm slab thickness. The calculated loss does not consider roughness. (a) Simulated optical mode effective refractive index with fixed waveguide width of 550 nm. (b) Simulated optical mode loss with fixed waveguide width of 550 nm. (c) Simulated optical mode effective refractive index with fixed wavelength of 1950 nm. (d) Simulated optical mode loss with fixed wavelength of 1950 nm.

1550 nm the waveguide becomes too multi-mode and since we target operation at both 1550 nm and at 2 µm on our MZI modulator, a narrower 550 nm width is adopted. The single mode cut off wavelength for a 550 nm wide waveguide is 1700 nm as shown in figure 4.1(a). At 1550 nm, figure 4.1(b) shows that the loss of the TE1 mode is about 10dB/cm higher than the TE0 mode. Such a waveguide is still usable in the C-band in our 'single mode' modulator optimization.

4.2 Phase shifter electro-optical simulation method

The phase shifter response is analysed by a combination of electrical device simulation using Silvaco TCAD tools and optical device simulation using a MATLAB based waveguide mode solver [104]. We uses matlab scripts to control the overall simulation flow. It automatically generates the Silvaco Atlas script, calls command line Silvaco simulations packages and modifies Athena script to scan parameters.

The overall simulation flow consists three main parts:

1. The Silvaco simulation software was used to build the electrical device model. The Athena package of Silvaco TCAD generates the cross section of the device by mimicking the actual fabrication process. The doping distribution is also simulated based on dose and energy of ion implantation. and the final structure including all diffused doping information Figure 4.2 shows the net doping concentration in silicon after ion implantation and thermal annealing.

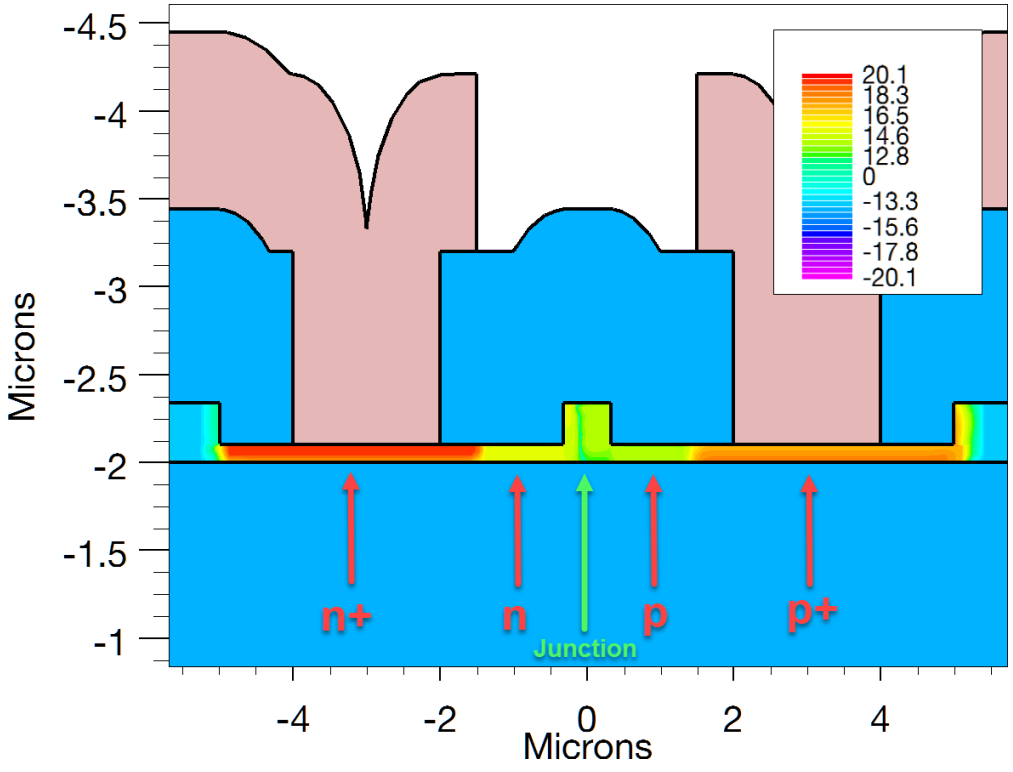

Figure 4.2: Cross section showing the net doping concentration. Produced with Athena.

2. The cross section and all doping information is then feed into Atlas package of Silvaco TCAD via a form of a structure file. Atlas simulates the free carrier distribution and recombination under various electrical conditions: a) different fixed reverse bias/forward bias voltages for obtaining the DC response, and with b) a step rise and a step fall in bias voltage for analysing the transient response in order to extract the RF performance. c) a sinusoidal AC response to extract capacitance and transmittance of the PN junction. The simulated free carrier concentration against various reverse biases voltage is illustrated in figure 4.3. The depletion region width enlarges with increasing reverse bias voltages. A step rise voltage from 0V to -4V as well as step fall voltage from -4V to 0V are also

applied to analyse the AC performance of the device. This free carrier distribution is independent of optical wavelength.

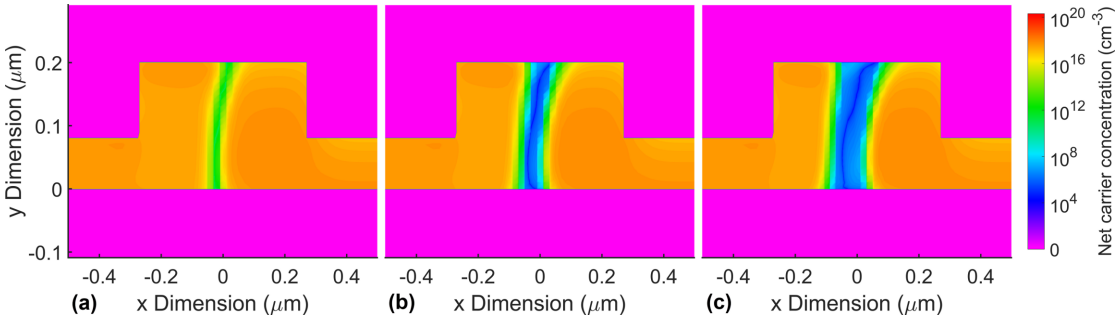

Figure 4.3: The simulated net carrier concentration of the phase shifter under various reverse biases. (a) Reverse bias 0V (b) Reverse bias 2V. (c) Reverse bias 4V.

3. Finally we implement the interaction of free carriers and light in MATLAB. The free carrier distribution is translated into a change in complex refractive index, where equations 3.63 and 3.64 [49] are used. A MATLAB based optical mode solver then finds the mode in the waveguide adding both the calculated perturbation in refractive index due to the free carrier effect and the baseline material refractive index. Figure 4.4 shows an example of a modulated optical mode. The performance of the phase shifter can then be evaluated through the effective refractive index change and loss of each optical mode.

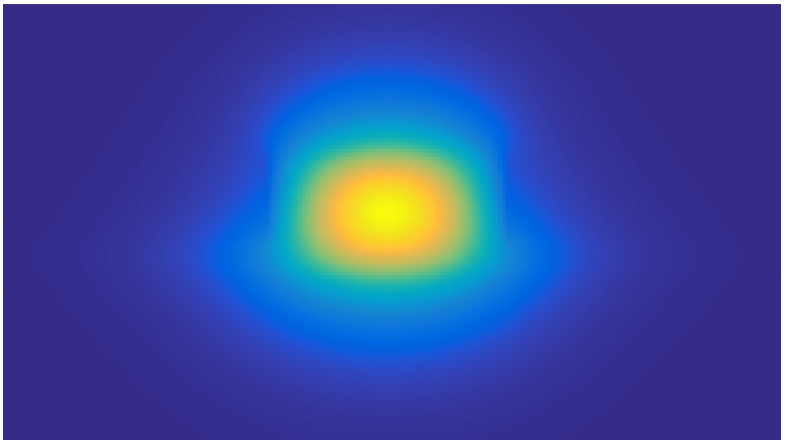

Figure 4.4: Cross section of final mode profile found in MATLAB by taking consideration of carrier effect.

Figure 4.5 shows an example of the refractive index change by varying the reverse bias conditions . The phase shift for a given length can then be calculated using equation 3.56 and the L_π can also be derived using equation 3.58.The rise response and fall response are produced by giving a step signal, and the transient simulation is running in time domain. The bandwidth of the phase shifter can then calculated

from the rising and falling time. This bandwidth however is the ideal bandwidth of a thin slice of phase shifter and if designed correctly is often far above the performance of the travelling wave electrode.

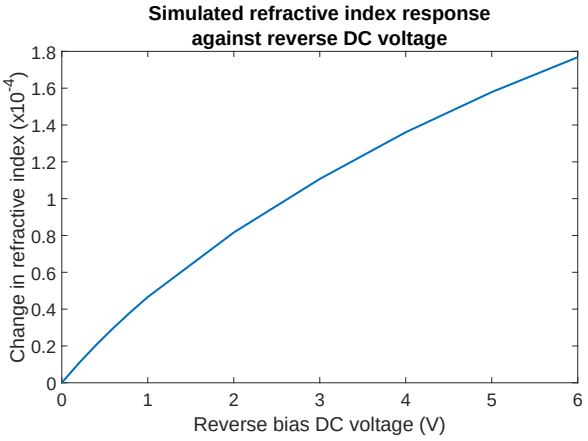

(a) DC Response

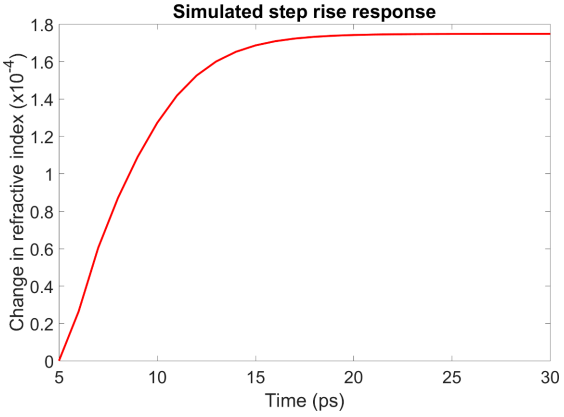

(b) Rise Response

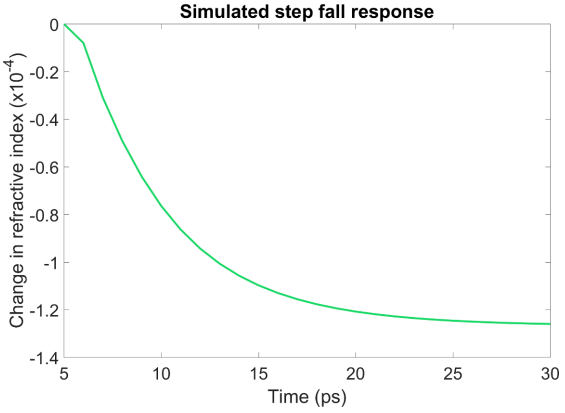

(c) Fall response

Figure 4.5: The refractive index change in response to change in electrical signal.

4.3 Phase shifter design insight

4.3.1 Wavelength analysis

Figure 4.6 shows how such a phase shifter design responds to 4V reverse bias when the wavelength is varied. The dashed line in the graph represent the loss derived from a similar device but with doping separations S_{dopP} and S_{dopN} increased to 1.7 µm to almost eliminate the loss contribution due to mode overlap with the highly-doped region. We notice that the change in refractive index rises as the wavelength

increases from 1500 nm towards 2000 nm. The overall loss shown in dotted curve also increases, and even without the absorption from the highly doped regions, loss still follows a rising trend. This is in accordance with the trend predicted by the generalised equation of the carrier effect [49], i.e. both change in refractive index and loss due to carrier effect are higher at 2 µm than at 1.55 µm. However if fixing the waveguide width at 550 nm, as depicted by the blue curve, there is a level off in the rise of change in refractive index after 2000 nm and there is even a slight drop beyond 2150 nm. This is because the mode profile size is significantly larger at longer wavelengths, and the effective overlap between the optical mode and the carrier changing region is diluted. Although the carrier effect is higher at longer wavelengths, the overall effect is the result of both. The light grey curve shows the effective index change for an optimized waveguide width at each wavelength. The general trend is that increasing the waveguide width increases the effective index change at longer wavelengths. As we can see, the 550 nm width strikes a good balance between the 1550 nm and 2 µm wavelengths.

4.3.2 Phase shifter dimension parameters

During the design process, two important dimension parameters have been swept to analyse their effects. The first is the separation between the high doping sections and the optical waveguide core. To form Ohmic contacts, a high doping concentration (eg. 1e20 cm^{-3}) at the interface of silicon and metal is required. According to figure 4.7(a), when varying the doping separation, there is a trade-off between device bandwidth and free carrier loss. The device bandwidth rises as the high doping separation decreases, due to reduced access resistance. However, when the high doping is too close to the waveguide core, the overlap between the optical mode and free carriers in the high doping region increases, which results in significant optical loss. Therefore, a trade-off between device bandwidth and device loss should be considered. We note that at 1950 nm the optical mode size in the waveguide must be larger than at 1550 nm, therefore a larger separating S_{dopP}+S_{dopN} is required, which theoretically reduces the bandwidth of the device.Figure 4.7(b) shows that the doping separation has very little effect on the efficiency of the modulator, as the parameters of the low doping concentration region have a more direct impact on the PN junction geometry and position, and hence on the device efficiency. The PN junction position is the second major parameter. By scanning its position, as illustrated in figures 4.7(c) and 4.7(d), we see that with the selected doping concentrations the device has the lowest loss and

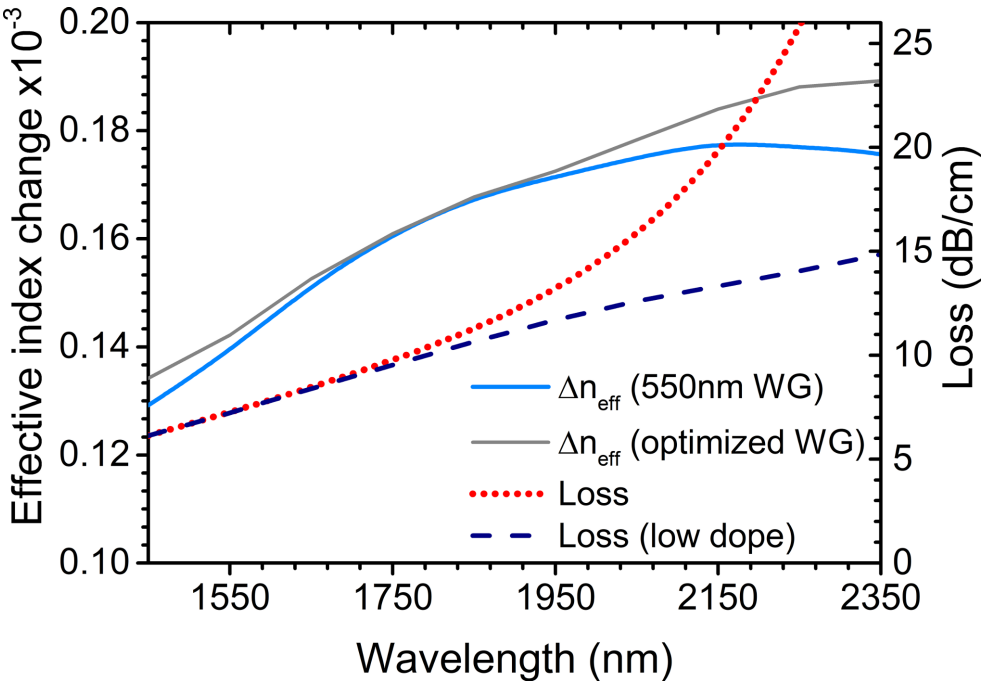

Figure 4.6: The simulated effective refractive index change and loss of a phase shifter with the adopted design due to carrier effect under 4 V reverse bias across the 1450-2250 nm wavelength range. The blue line shows the refractive index change for the 550 nm wide waveguide. The light grey line shows the refractive index change for a a waveguide width optimised at each wavelengths, with a width ranging from 450 nm to 650 nm. The red dotted line show loss with the adopted 550 nm wide waveguide. The dark blue dashed line is the simulated loss from a similar phase shifter design but with larger 1.7 µm S_{dopP} and S_{dopN} to serve as the reference loss of the low doped region.

highest efficiency when it is placed near the centre of the waveguide because the maximum overlap of the optical mode and depletion region is achieved. The bandwidth, however, increases when the junction position is close to the edge of the waveguide core. Because in this case the PN junction is partially in the slab region of the waveguide and has a reduced cross section compared to in the core region. This results in lower capacitance and hence higher bandwidth. However achieving this condition, comes at the cost of significantly higher loss and lower efficiency, because the depletion region will be so far off from the optical mode centre. If the doping separation is chosen properly, the simulated bandwidth should be greater than 75 GHz regardless of junction position.

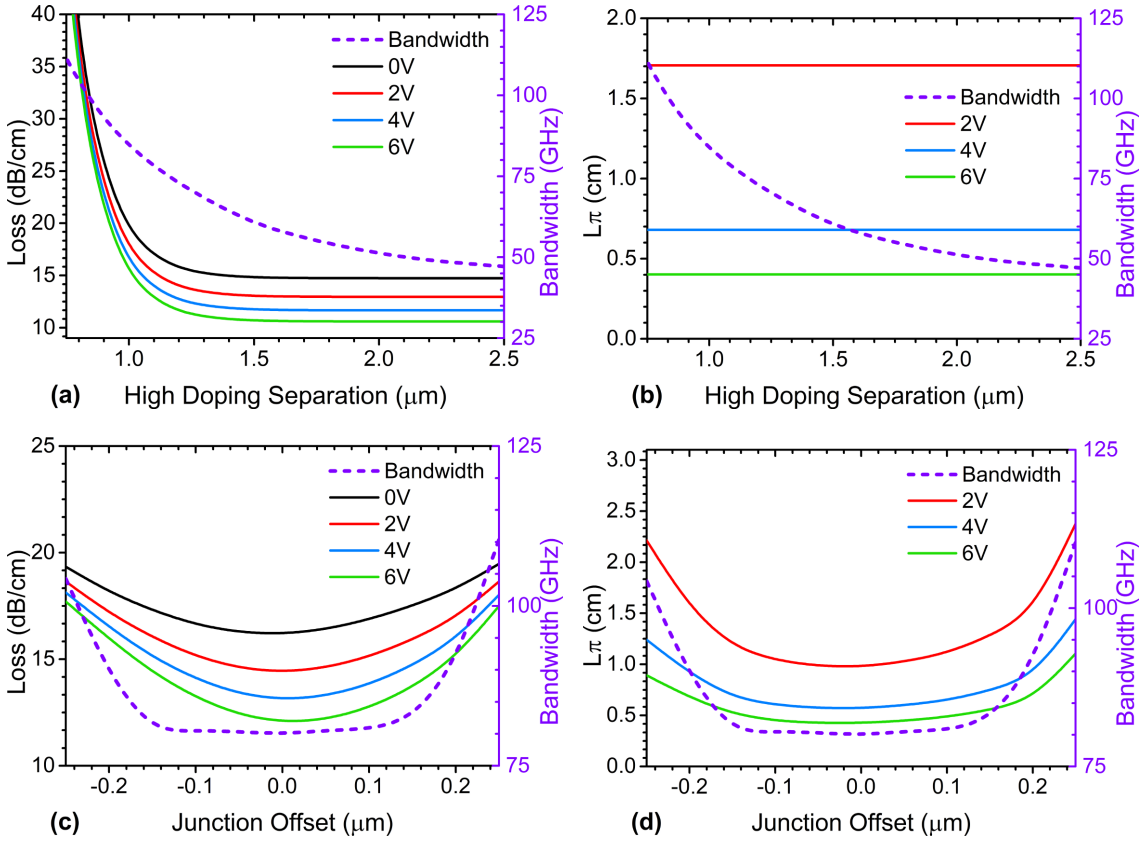

Figure 4.7: MZI modulator phase shifter simulation in 1950 nm. (a) Simulated loss vs high concentration doping separation with fixed junction offset 0. (b) Simulated L_π vs high concentration doping separation with fixed junction offset 0. (c) Simulated loss vs junction offset with fixed high concentration doping separation (S_{dopN}) 1.125 µm for n+ and (S_{dopP}) 1.025 µm for p+. (d) Simulated L_π vs high concentration doping separation with fixed junction offset 0.

4.3.3 Doping concentration DC analysis

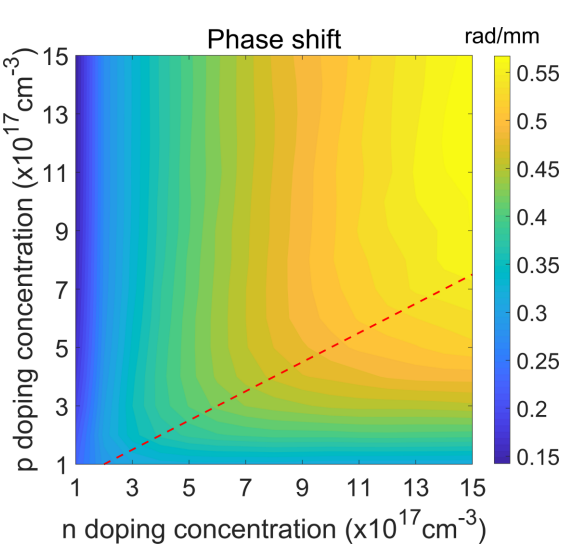

(a) Phase shift per mm, from 0V to 3V DC reverse bias.

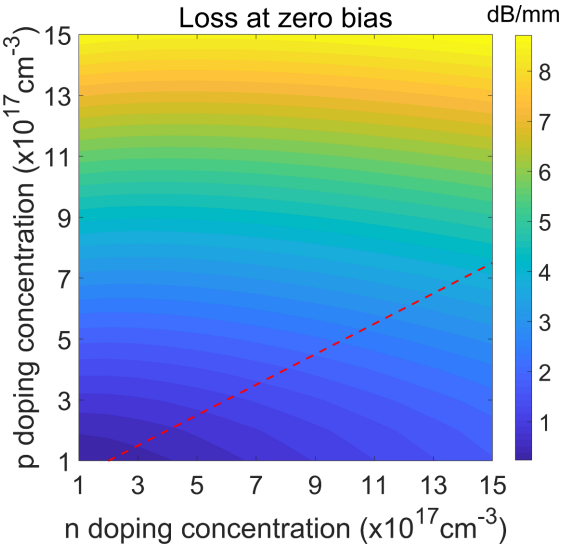

(b) Loss per mm at zero bias, excluding passive waveguide loss.

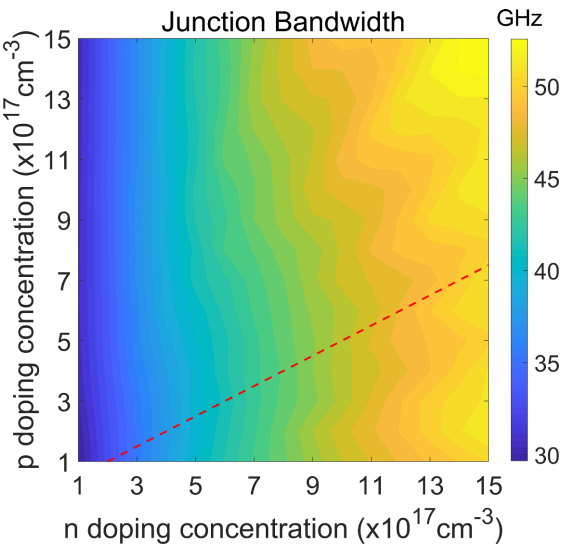

(c) Bandwidth of PN Junction.

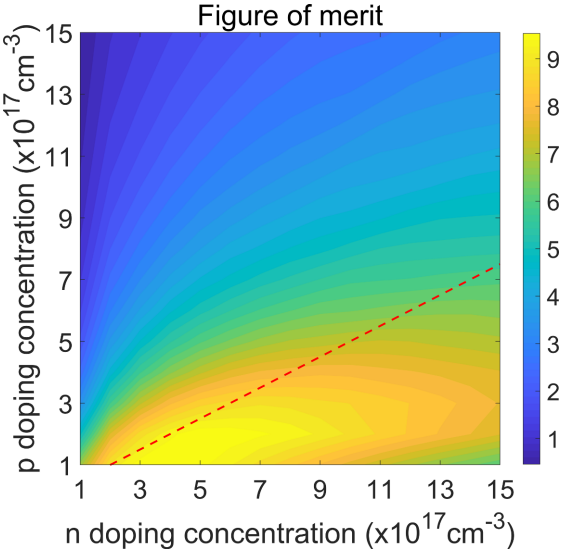

(d) Figure of merit: Phase shift × BW/(Loss + Passive loss).

Figure 4.8: Simulated DC performance of a phase shifter with various combination of doping concentrations. In the simulation, the target p and n doping are varying from 1e17 cm^{-3} to 1.5e18 cm^{-3} with a step of 1e17 cm^{-3}

.

In order to investigate how the low-dose doping affecting the phase shifter performance, we have run an array of simulations with different combinations of p and n

doping concentration. The PN junction cross section geometry is the same as the aforementioned simulations. The PN junction is in the centre of the waveguide and highly doped region are 1.1 µm away from the waveguide centre. All other conditions are the same, the only two variables are the p and n doping concentrations ranging from 1e17 cm^{-3} to 1.5e18 cm^{-3} with a step of 1e17 cm^{-3}.

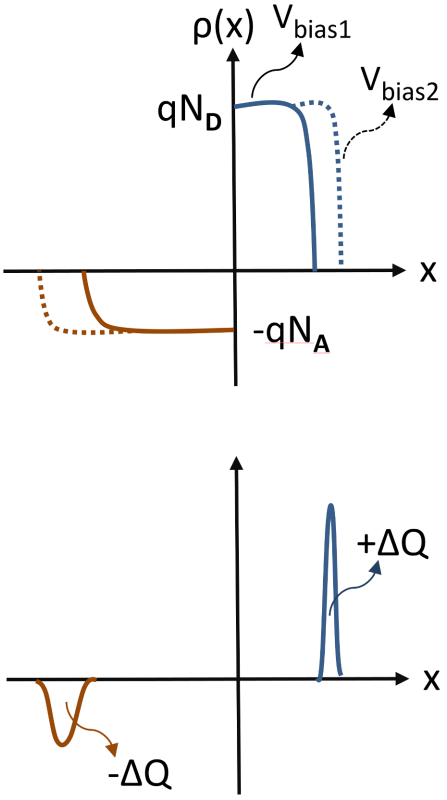

Figure 4.9: PN junction charge distribution under different reverse bias voltages, where $V_{bias1} < V_{bias2}$. N_D is the donor concentration in the n-type doped silicon and N_A is the acceptor concentration in the p-type doped silicon. After [105].

Figure 4.8(a) illustrates the phase shift per mm phase shifter length from 0V to 3V reverse bias voltage. A large phase shift per unit length is favourable, it implies higher modulation efficiency and shorter devices. According to the simulation, higher doping concentration in general providing a larger phase shift as there are more free carriers to begin with. Another crucial factor is the ratio of p and n doping concentration. At equilibrium the depletion region is charge neutral with positive charge of donor and negative charge of acceptor cancel each other. When adding reverse bias, as depicted in figure 4.9, the displacement of free carriers causing a depletion width extension and a charge change on each side; however an equal amount of electrons and holes have been displaced to keep the depletion region charge neutral. The eventual refractive index change is due

to the interaction between the optical mode and the change in depletion region. Since equal amount of electrons and holes has been displaced, depletion region width change under bias voltages dictates the modulation intensity. Therefore considering case of fixed total doping (n doping + p doping), the ratio between two types of doping are tuned to maximize the overall depletion width. If both free carriers contributed equally to the plasma dispersion dispersion, the optimum ratio between the n and p doping should be close to 1:1. However according to figure 3.9, per unit hole concentration change contributes more refractive index change than electrons at both 1550 nm and 2 µm. To increase the depletion region width on p side means higher n to p ratio. Thus the actual optimal doping ratio between n and p for the best modulation efficiency should be greater than one, somewhat towards 2:1 ratio according to the simulation for this particular phase shifter structure as shown by the red dashed line in figure 4.8(a).

The insertion loss per mm excluding passive waveguide loss is shown in figure 4.8(b). Please note that the loss here is the loss at zero bias representing the worst case, in practice due to operating at carrier depletion mode, the actual loss when operating with a reverse bias will be lower. As we can seen from the trend in the graph, the loss contribution from per unit increase in p and n are not equal, the loss rises significantly with an increasing p doping concentration, but only very moderately for an increasing n doping concentration. As unit electron contributes much more than holes in loss, to minimize the loss, we need to decrease the depletion region on n side, hence favouring a high n doping and a low p doping. Therefore coincidentally, by picking an n to p doping concentration ratio value grater than one, one can achieve both better modulation efficiency and lower loss.

We find out that the simulated phase shifter bandwidth is always above 30 GHz for all combinations as illustrated in figure 4.8(c). This however only account for the bandwidth of an infinitesimal slice of PN junction, and in real device the actual bandwidth will be further limited by the metal electrode and the signal is also subjected transmission line loss. We will discuss the RF performance of a modulator in detail in the next section.

To put all the performance measures together, we can define a figure of merit of phase shifter as: $\frac{\text{Phase shift} \times \text{BW}}{\text{Loss} + \text{Passive Loss}}$. The passive loss we use here is 0.77 dB/mm. Figure 4.8(d) shows that, for this particular cross section geometry, higher n doping is more favourable than high p doping.

4.4 High-speed considerations

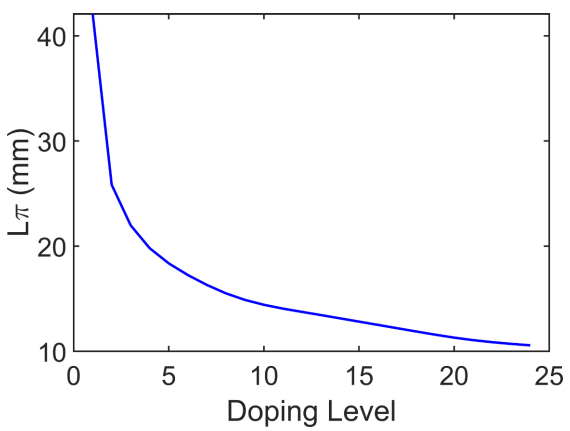

(a) L_π, with 2V to 4V DC reverse bias in a push-pull configuration.

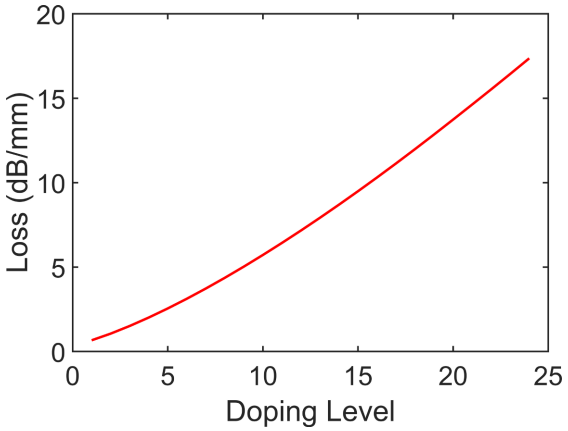

(b) Loss per mm at zero bias, including a 0.77 dB/mm passive waveguide loss.

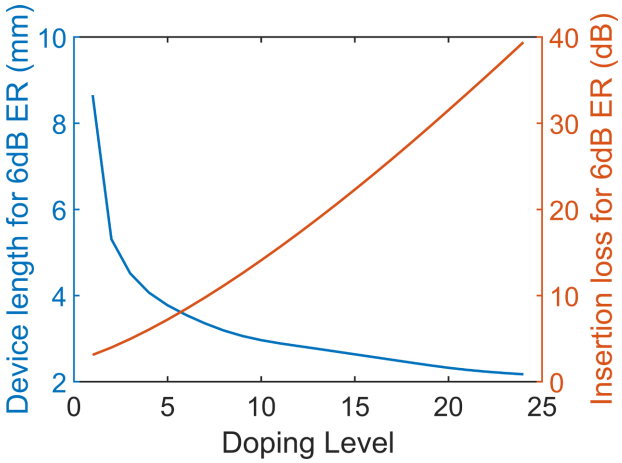

(c) The phase shifter length required and the total insertion loss to achieve 6 dB extinction ratio with 2V to 4V DC reverse bias in a push-pull configuration.

Figure 4.10: Phase shifter DC performance under various selected doping levels.

To obtain a more accurate modulator bandwidth, we need to consider not only the PN junction cross section but the phase shifter and the travelling wave electrode as a whole. We picked 25 doping levels to further analyse the effect of doping concentration on AC performance. The doping levels are generally following the red dashed line in graph 4.8 linearly ranging from lowest level 2 with n-type doping concentration 2e17 cm^{-3}, p-type doping concentration 1e17 cm^{-3} to highest level 25 with n-type doping concentration 15e17 cm^{-3}, p-type doping concentration

7.5e17 cm^{-3}. All other dimensions are identical to the previous section with PN junction in the middle of the waveguide.

Figure 4.10 shows the DC performance of phase shifters with these doping conditions. The modulator are assumed to work in a push-pull condition, which effectively doubles the efficiency. The reverse bias voltage on each arm is 2V for off states and 4V for on state. In the simulation we set a target extinction ratio of 6 dB, which at quadrature point is equivalent to approximately 37 degree phase shift on each arm. As shown in figure 4.10(c), the phase shifter length required for achieving 6dB ER drops significantly as doping increases, and there is a turning point at around doping level 5. Of course the short length are associated with higher total insertion loss due to the absorption from the free carriers at higher doping levels. However there is an extra perk for being shorter length: shorter phase shifter means shorter electrode which implies lower RF signal attenuation and higher bandwidth.

For each doping level, the capacitance and conductance value of the phase shifter structure are then extracted at different frequencies. The C and G values here are extracted from the total impedance and do not take account of the electrode part. Figure 4.11 shows the simulated C and G against the frequency at doping level 10. The capacitance increases while conductance decreases as frequency rises. Also a larger reverse bias causes a wider depletion region which gives a lower capacitance value.

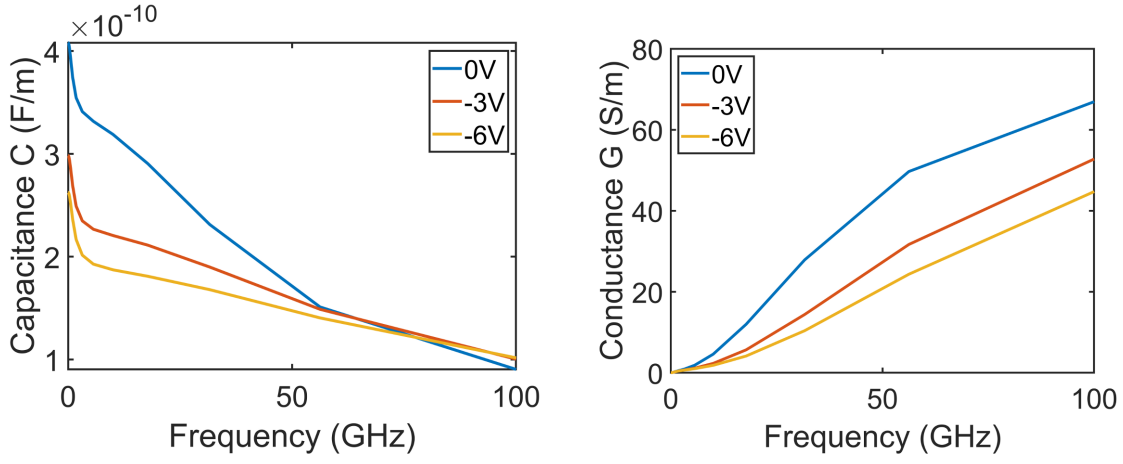

(a) Simulated Capacitance per meter, C

(b) Simulated Conductance per meter, G

Figure 4.11: Simulated C and G of a phase shifter at doping level 10 against the frequency.

If keep the frequency fixed, the trend of C and G against doping levels are shown in figure 4.12. The capacitance rises as the doping level increases, mostly because of a reduced depletion width. The conductance however are relatively stable with a changing doping level.

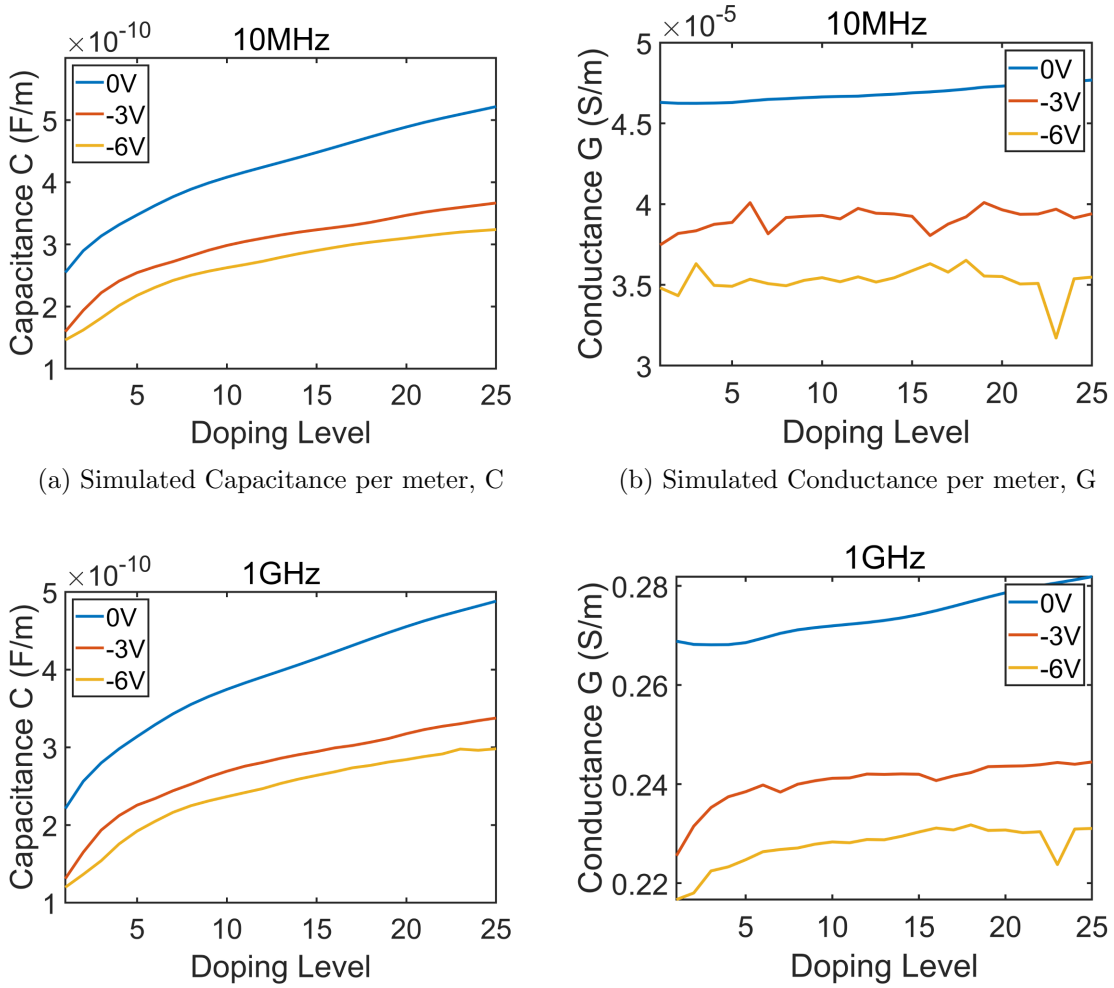

(a) Simulated Capacitance per meter, C

(b) Simulated Conductance per meter, G

(c) Simulated Capacitance per meter, C

(d) Simulated Conductance per meter, G

Figure 4.12: Simulated C and G of a phase shifter against doping levels.

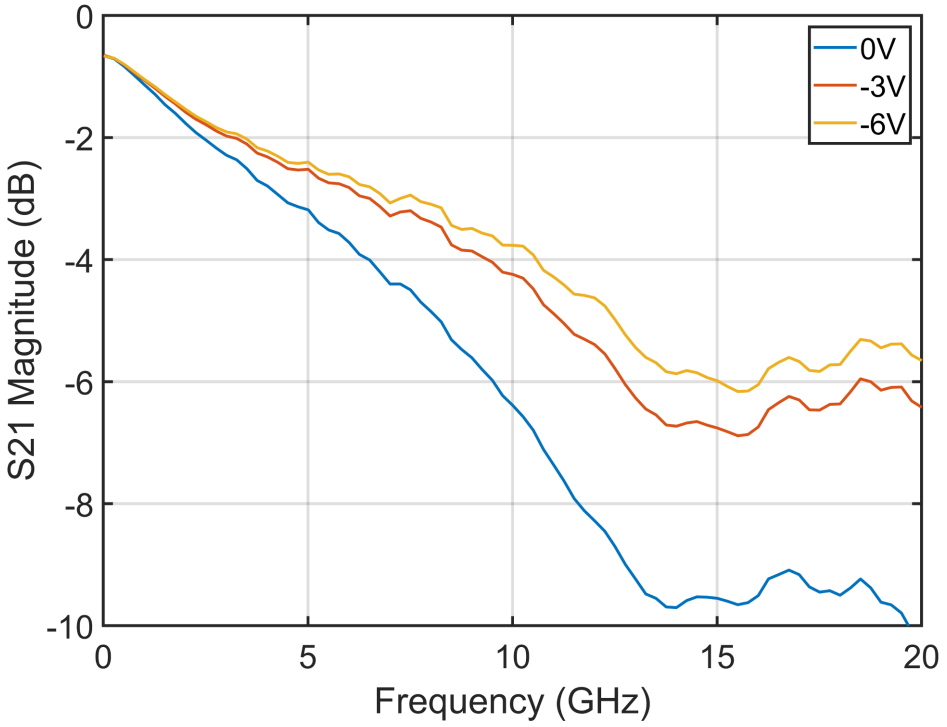

Figure 4.13: EE S21 measurement data from a 1.8 mm long phase shifter with doping concentration of n 3e17 cm^{-3}, p 8.5e17 cm^{-3}.

To include the the response from electrode and other parasitics, we can resort to a lab measurement. The figure 4.13 shows an experimental S21 EE response measurement of a 1.8 mm long phase shifter with a different doping concentration (n 3e17 cm^{-3}, p 8.5e17 cm^{-3}). But the travelling wave electrode is the same. Knowing the total length of 1.8 mm, the R, C, G, L value per unit length can be extracted from the experimental S21 measurement as shown in 4.14. The R and G have then been smoothed, to eliminate some resonance glitches.

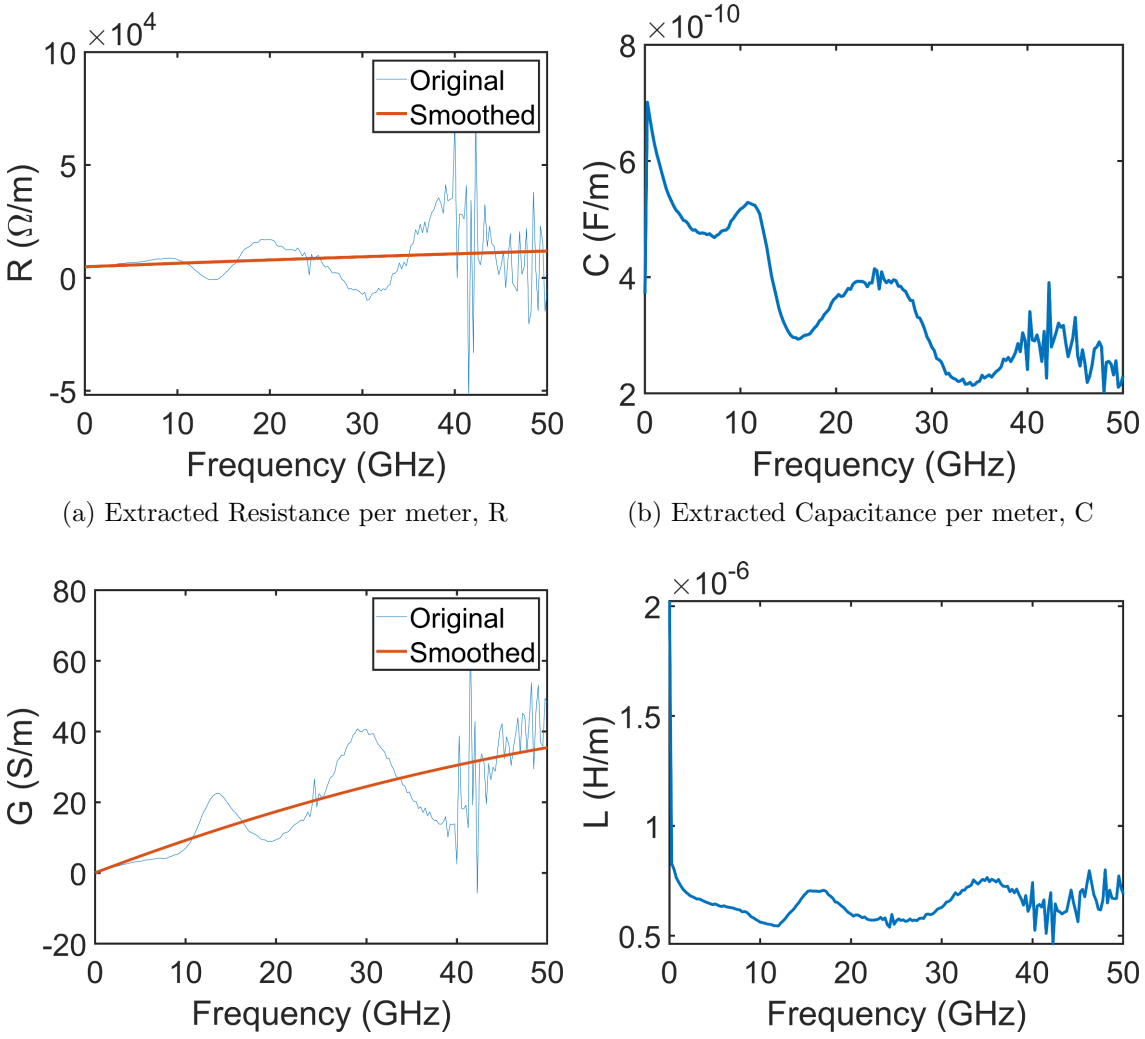

(a) Extracted Resistance per meter, R

(b) Extracted Capacitance per meter, C

(c) Extracted Conductance per meter, G

(d) Extracted Inductance per meter, L

Figure 4.14: The extracted R, C, G, L value from the experimental S21 data.

The R and L value are contributed mostly from the metal electrode. While the C and G comprises mostly portions from the PN junction and other parasitics. The simulated C and G of the phase shifter with n 3e17 cm^{-3}, p 8.5e17 cm^{-3} are first been subtracted from extracted experiment value. And C and G values from various doping level 2-25 are then be add back. The updated C and G are combined with the experimentally extracted R and L to generate S21 EE response. For each doping level the S21 are generated with a phase shifter length capable of delivering 6 dB extinction ratio modulation, referring to figure 4.10(c). The resulting S21 of selected doping levels are plotted in 4.15. The -6 dB EE bandwidth of such curve can then be used to estimate the -3 dB EO bandwidth of the modulator [106].

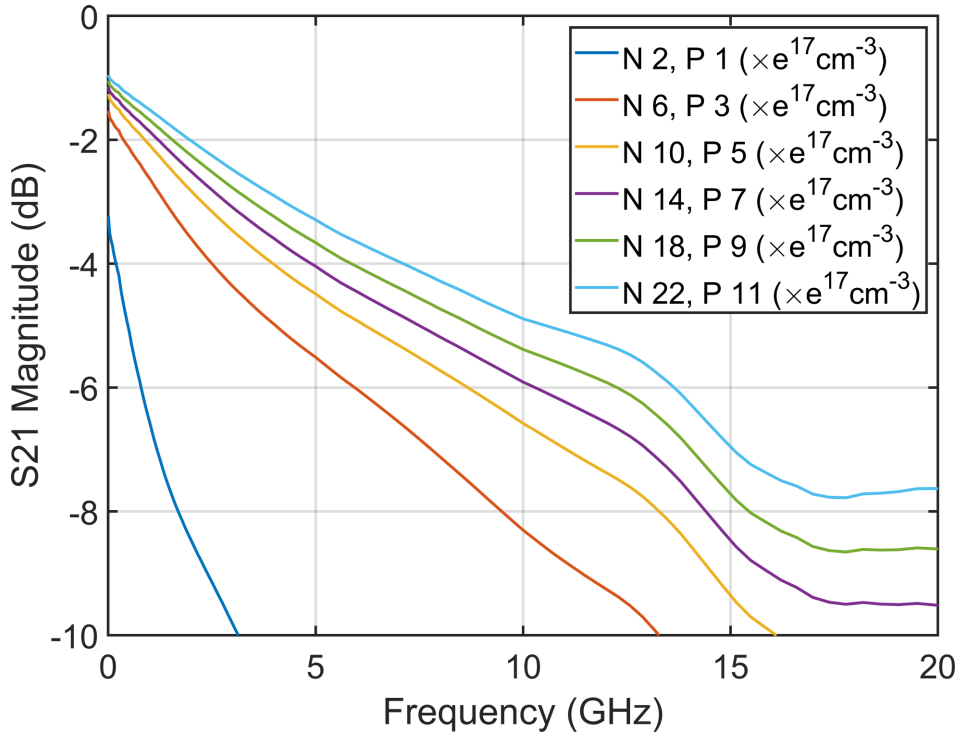

Figure 4.15: Simulated S21 EE response of phase shifter with multiple doping levels.

The bandwidth and insertion loss of a push-pull MZM to achieve 6dB extinction ratio with 2V to 4V DC reverse bias are given in figure 4.16(a). The updated figure of merit, $\frac{\text{BW}}{\text{Insertion Loss}}$, shows a maxima in figure 4.16(b) at doping level of 4. However if one can sustain a higher loss in their device specification, higher doping level can be used to further reduce the device length and to improve high-speed performance.

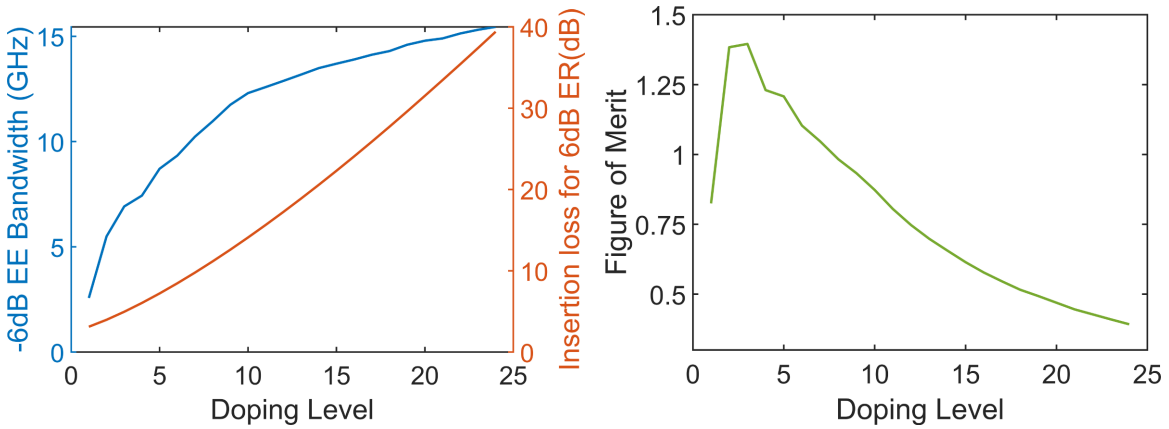

(a) 6 dB attenuation EE bandwidth and insertion loss for achieving 6 dB extinction ratio in amplitude modulation

(b) Figure of merit

Figure 4.16: The simulated bandwidth and total insertion loss to achieve 6 dB extinction ratio with 2V to 4V DC reverse bias in a push-pull configuration.

Doping concentration and ratio therefore play a pivotal role in device performance in terms of both efficiency, loss and RF bandwidth. The three are trading off with each other. Therefore to fully optimize a depletion type modulator based on SOI platform one need to start from the application requirement and specifications. One can trades some loss performance to efficiency and bandwidth by increase overall doping concentration. And depends on the certain geometry of PN junction, there should be a optimized p-n doping ratio. For junction in the middle, it is often more favourable to have higher n doping. If the drive voltage is exceptionally large, a ratio close to 1:1 will make the depletion region grow symmetrically inside the waveguide and delay the saturation voltage. For a PN junction positioned lopsided, the doping region takes up smaller region inside the waveguide should then have higher doping concentration to properly expand depletion region into the waveguide.

4.5 Layout mask drawing

The Mach-Zehnder Modulator (MZM) in this run (Figure 4.17) contains phase shifter on both arms. This converts the phase shift modulation into amplitude modulation. Both the device with grating coupler and the device using butt coupling are included in the mask design. All beam coupler are based on MMI, no

Y-splitter is used. This implies that the wavelength supported by the modulator will be limited by the MMI, but the insertion loss in generally lower in MMI than in Y-splitter. The two arms of MZI are of difference length to create a sinusoidal amplitude response against waveguide, which facilitate the testing procedure. The shift in peaks can be more intuitive to observe than change in amplitude.

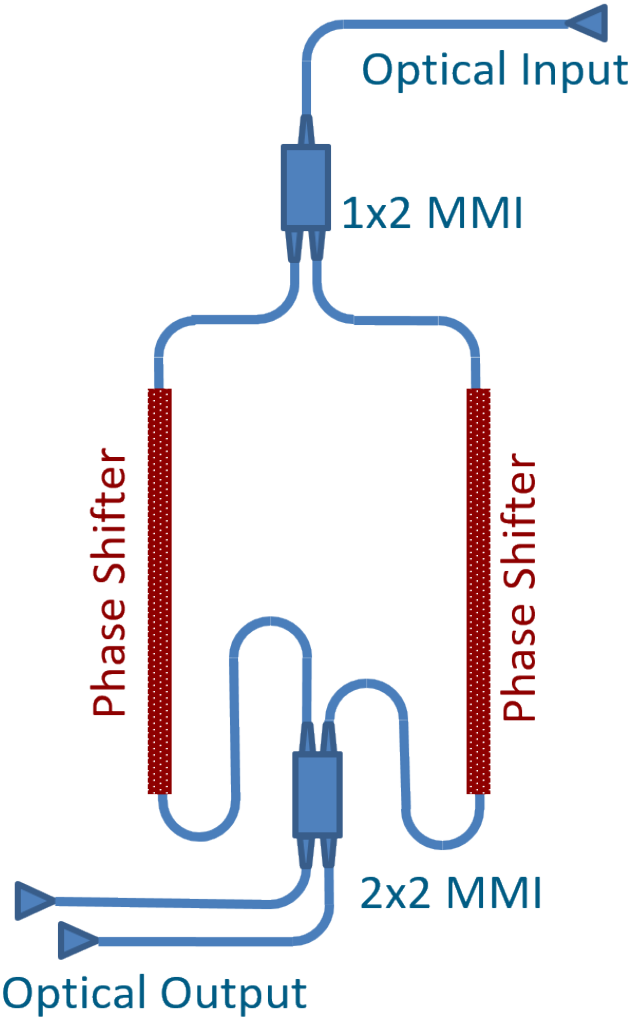

Figure 4.17: Principle schematic of a Mach-Zehnder Modulator.

The chip design is carried out on L-Edit layout software. The mask layout is generated with C++ scripting code paired with L-Edit library. The script predefines the drawing of some common structures eg. waveguide, taper, grating couplers into functions. For each new mask layout, a new C++ macro is created and it specifies the geometric parameters, alignment and linking of various basic structures. In modulator case, new function files was created as new structures are required and they may be reused in the future. Complex structures and repetitive patterns can be fast implemented by this semi-auto scripting approach. The

mask design is output in GDSII file format. Both e-beam lithography and photo lithography can be performed based on this mask file.

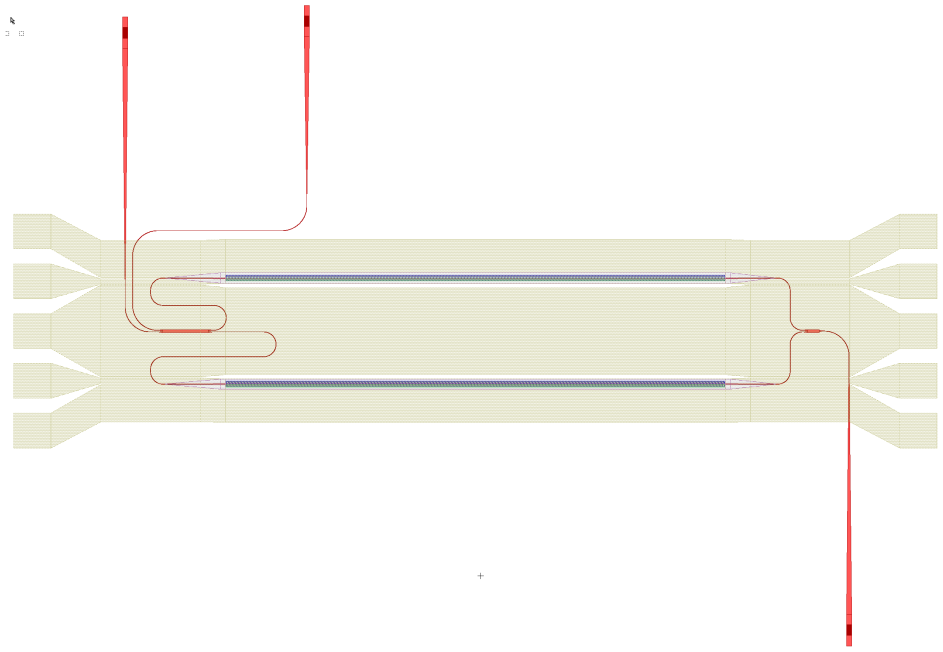

Figure 4.18: Mask design of modulator with unbalanced MZI.

A example modulator mask design is illustrated in Figure 4.18. It consists an MZI at its core and two phase shifters on both arms. The arm difference is related to the free spectral range (FSR). In our case an FSR around 5 nm should provide us a convenient view of the modulation shift during the device testing. Therefore arm difference around 200 µm are generally adopted. Some 150 µm and 300 µm devices are often also included. The number of bends for each arm are deliberately made the same, so that the bend loss of each arm would affect little in the extinction ratio of MZI. If balanced MZM is used, it needs to include a thermal heater so that the operating point can be fine tuned during the characterisation. Since the device is the push-pull type the length of the phase shifter should be comparable to the half of the L_π. In our case, we usually include devices with phase shifter length of 0.5 mm, 1.0 mm, 2.0 mm and so on.

Since the high speed and long phase shifter length, travelling wave electrode is required. A good electrode design should satisfy three criteria: a) electrical signal velocity matches the optical signal, b) the device impedance matches the driver impedance and the terminal load impedance ,and c) low attenuation of microwave. To design such electrode however is not trivial, it requires several iterations of simulations and test fabrication to optimize the design. In our case, since the device dimension is comparable to a previous design, instead of designing and

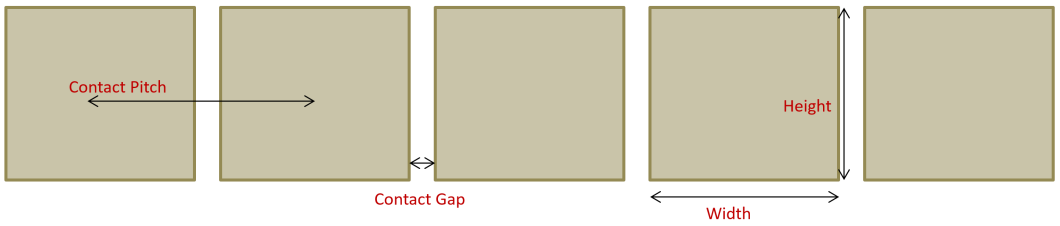

(a) Schematic of contact pad.

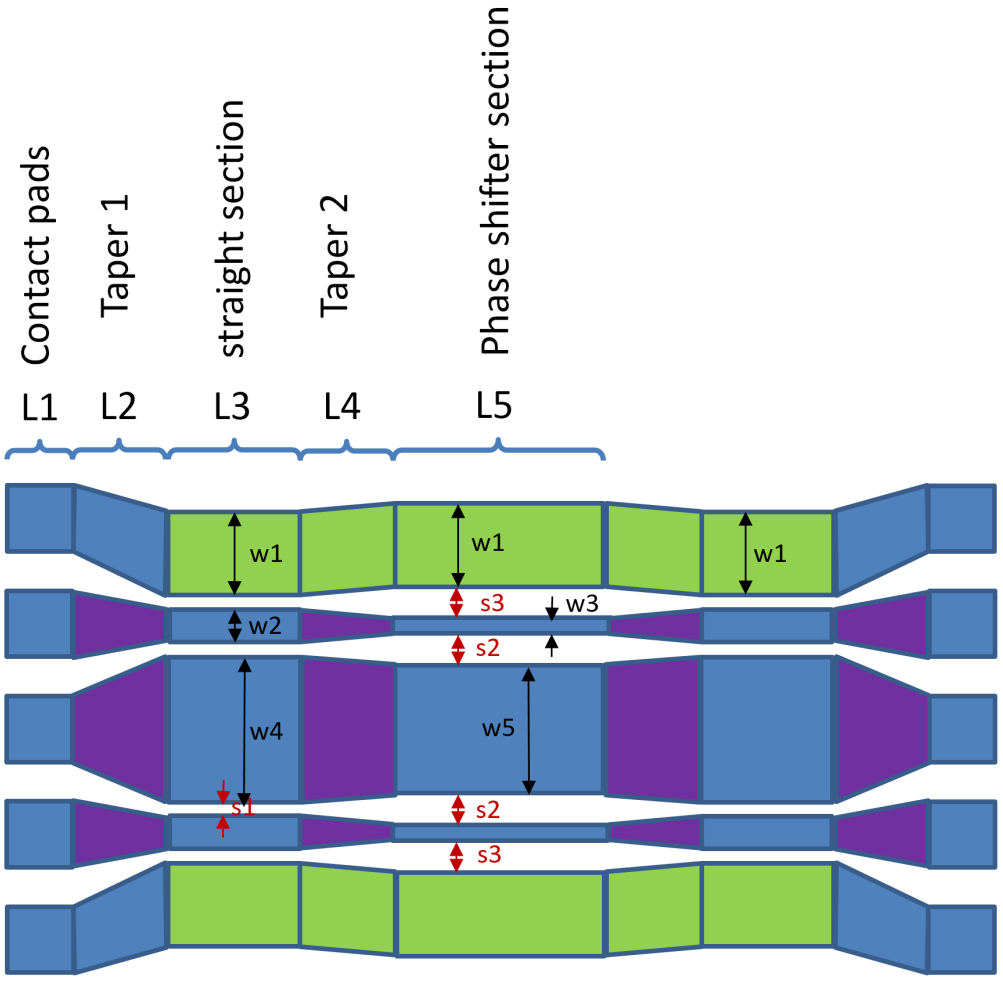

(b) Schematic of travelling wave electrode.

Figure 4.19: Schematics of electrode design.

simulating from scratch we modified a functional electrode design from a previous device.

The contact pad dimension is chosen according to the 100 µm pitch RF probe available in the high speed lab. Since it is a push-pull design, GSGSG probe is used, and the contact pad design is shown in Figure 4.19a. The contact pad pitch is 100 µm, the width of the pad is 70 µm, the height is 75 µm, the gap between two pad is 30 µm. As shown in Figure 4.19b, the travelling wave electrode consists 5

different sections and it is vertically and horizontally symmetrical. The dimension of the electrode: L1=75 µm, L2=100 µm, L3=250 µm, L4=50 µm, L5 equals to the phase shifter length, w1=75 µm, w2=11.1 µm, w3=9.1 µm, w4=184.9 µm, w5=175.3 µm, s1=2 µm, s2=7.8 µm, s3=4 µm. The electrode consist two sets of pads on both side of the modulator. One is for input signal and the other for external impedance termination.

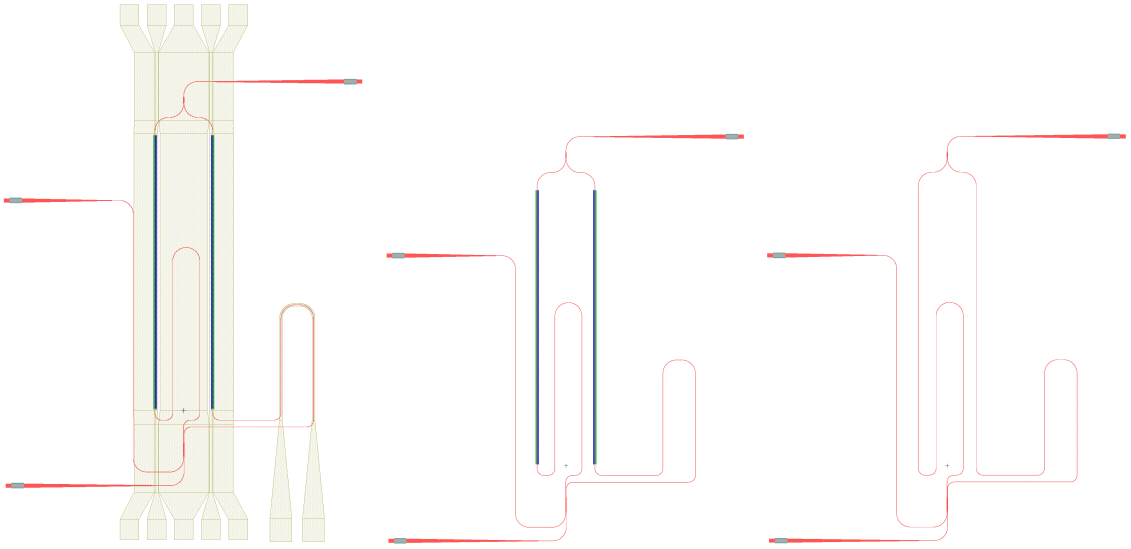

(a) Mach-Zehnder Modulator.

(b) Loss analysis structure will MZI and all dopings but without metal electrode.

(c) Loss analysis structure will bare passive MZI.

Figure 4.20: Example mask layout design for the modulator and reference normalisation structure used to analyse the loss contribution from different factors.

Various normalisation structures are also included. For example the structure in Figure 6.10b is identical to the one in Figure 6.10a except no electrode is included. From which the loss contributed by metal layer and metal via can be estimated. Similarly Figure 6.10c include only waveguide of a modulator. The effect of doped region can then be analysed.

Chapter 5

Experimental Setup for High-Speed Modulators

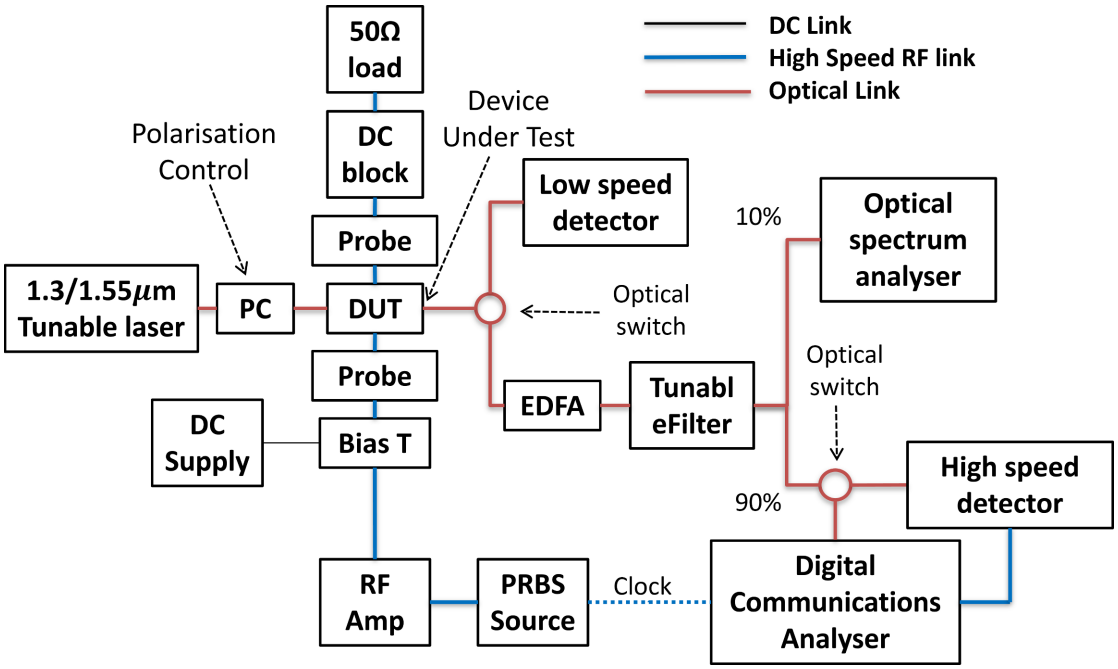

Figure 5.1: 1300nm/1550nm modulator measurement set up

For normal modulator measurement set up, the light source is a 1310 nm or 1550 nm tunable laser. The light is passed through device under test (DUT) and after that it is amplified by EDFA. The light path at this stage can also be switched to low speed detector for DC measurement and alignment. It is followed by a tunable filter to filter out unwanted signal, for example amplified spontaneous emission from EDFA. 10% of the light goes the optical spectrum analyser (OSA) to analyse its wavelength, and the spectrum information is used to fine tune the optical

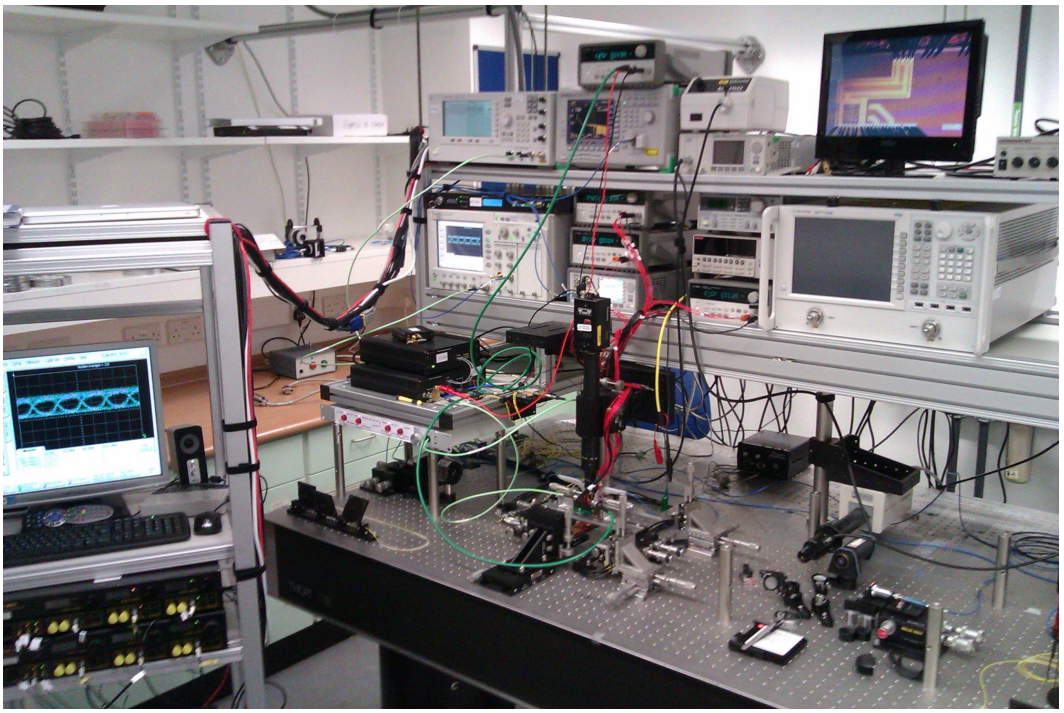

Figure 5.2: Photos of the high speed lab, modulator measurement corner

filter. The rest 90% goes either to a high speed detector or directly to the digital communication analyser (DCA) to produce an eye diagram. The DCA model is Keysight Infiniium DCA-X 86100D with Agilent 86116C-040 plugin module. For 1550 nm, the DCA has a build-in detector module, therefore no extra dedicated high-speed detector is required.

Expanding the measurement capability to 2 µm requires new components along the optical path, as most 1300/1550 nm equipment is incompatible with the 2 µm wavelength. Some bespoke 2 µm equipment has been used: an EOT ET-5000 high-speed 2 µm InGaAs detector, with a rated bandwidth of >12.5 GHz and peak responsivity of 1.3 A/W at 2000 nm; an amplified Thorlabs low speed 2 µm InGaAs detector, with peak responsivity of 1.3 A/W at 2300 nm and maximum internal gain of 70 dB; Thorlabs SM2000 silica fibres with 11 µm core diameter and optimized for 2 µm; and a Thorlabs TLK-L1950R tunable laser, which is tunable from 1890 nm to 2020 nm. We have also used a thulium doped fibre amplifier (TDFA) to increase the optical power, similar to the one presented in [18]. It uses an EDFA as a pump source, and gives 13 dB gain. Since the TDFA is polarization sensitive, a polarization controller before the signal input is essential. As the peak output power of the tunable laser is only 7 mW, the TDFA is used before the device under test (DUT). The low speed but more sensitive detector is used during alignment and DC measurements.

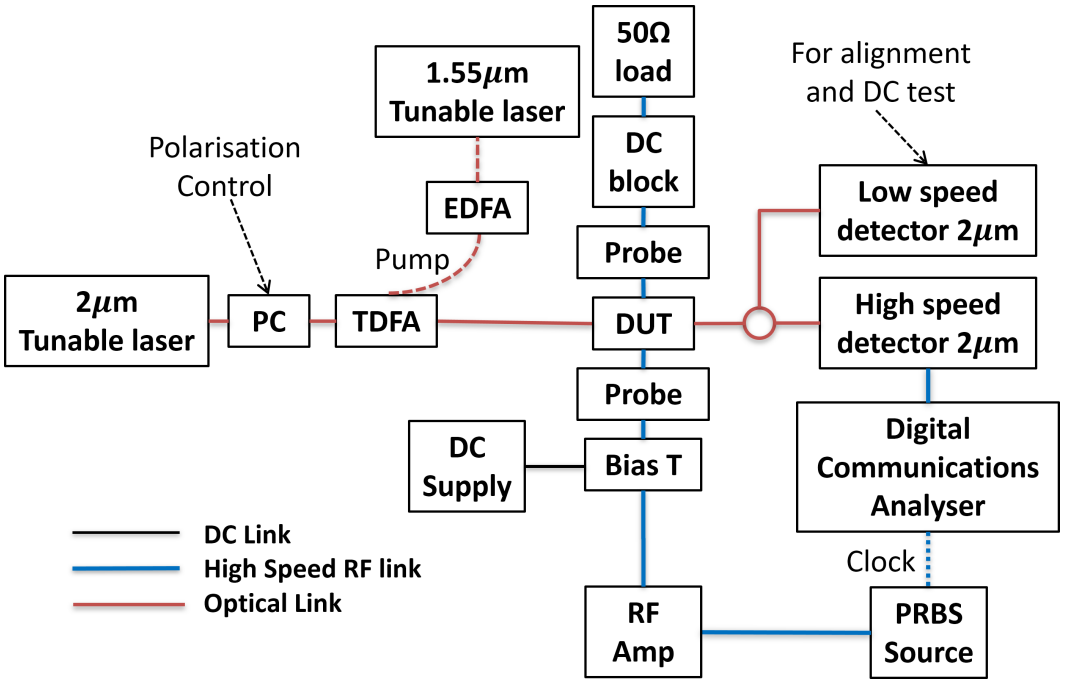

Figure 5.3: High-speed RF measurement set up for 2 µm wavelength modulator.

During the high-speed testing, a pseudorandom binary sequence generator (PRBS) is used to generate a bit sequence. The high-speed electrical signal is then amplified by a 3 stage Centellax OA4MVM3 amplifier and applied to the DUT with an RF probe. A bias tee is used to combine DC bias and high-speed RF signal. While testing the MZI with travelling wave electrodes, a second probe and external 50 Ω termination load and DC block are used. The modulated light is then feed into the high-speed InGaAs detector and then analysed by the digital communication analyser (DCA) to produce an eye diagram.

Compared to the conventional 1300/1550 nm setup, there are limitations in the 2 µm system. The high-speed detector had a nominal bandwidth of >12.5GHz, limiting the speed at which we could measure the modulator to around 20 Gbit/s and with reduced extinction ratio. A signal faster than 20Gbit/s cannot operate with the detector.

Moreover, the limited power budget of the 2 µm system often leads to a decent eye been masked by the noise floor of the DAC, hence an open eye is hard to discern. In the case of RF testing of the 2 µm ring modulator, a linear amplifier (SHF S804A) with 22 dB gain is inserted between the detector and DCA. The signal will degrade to some extent but is amplified enough to obtain a healthy signal to noise ratio.

Chapter 6

2 µm Wavelength Modulator Demonstrations

6.1 Wideband MZI modulator covering both 1550 nm and 1950 nm wavelengths

The design aim of the device is to demonstrate a proof-of-principle 2 µm modulator as well as using the same modulator with 1550 nm wavelength. This is to be able to provide an direct experimental comparison and show the various effects when scaling the optical wavelength up.

6.1.1 MZI modulator design

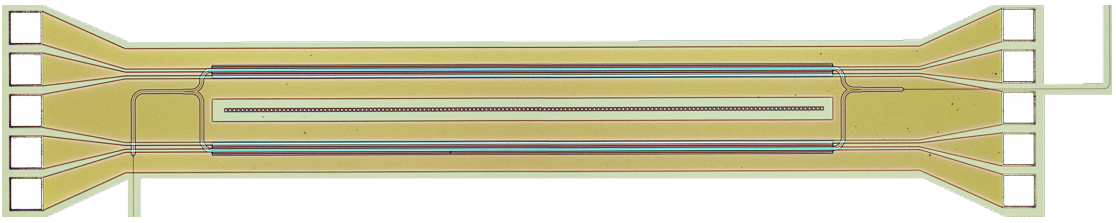

Figure 6.1: Optical microscope image of the MZI modulator. (to add scale bar and label)

The MZI modulators exploit the carrier depletion effect. It is therefore based on a PN junction in its active region. The fabrication platform is based on 220 nm SOI wafers with a 2 µm buried oxide (BOX) layer, in order to maintain compatibility with standard Si thicknesses used in NIR silicon photonics multi-project wafer

foundry services. Figure 6.2 shows a schematic of the cross section of the phase shifter in the MZI modulators. The silicon rib waveguide is 550 nm wide (W_{WG}) and etched by 90 nm in the slab region (h_{WG}). The device is fabricated by IME in a multi-project wafer (MPW) run with customised doping concentration.

Figure 6.1 is an optical microscope image of the core of the MZI modulator. The phase shifter is incorporated into both arms of an MZI, to convert the phase shift into an amplitude shift. An arm length difference of 180 µm is used in the MZI to obtain a sinusoidal response and to facilitate the characterization. In order to perform such wide band modulation at both 1550 nm and 1950 nm, special considerations need to be taken. For the 3dB coupler in the MZI, the device is designed to use Y-splitters instead of multi-mode interferometers (MMIs), providing significantly wider spectral bandwidth. Also it uses butt coupling, so that the modulator operating wavelength range is not limited by the relatively narrow bandwidth of grating couplers. The overall spectral bandwidth of the phase shifter is then only limited by the single mode waveguide bandwidth. At 1550 nm the waveguide does have a higher order TE1 mode, but the mode is weakly confined and with high loss. Therefore, the waveguide could be treated as single mode from 1550 nm to 2350 nm. A travelling wave electrode design is used with GSGSG pads on both ends and a tapered down section along the phase shifter. The pad pitch is 150 µm.

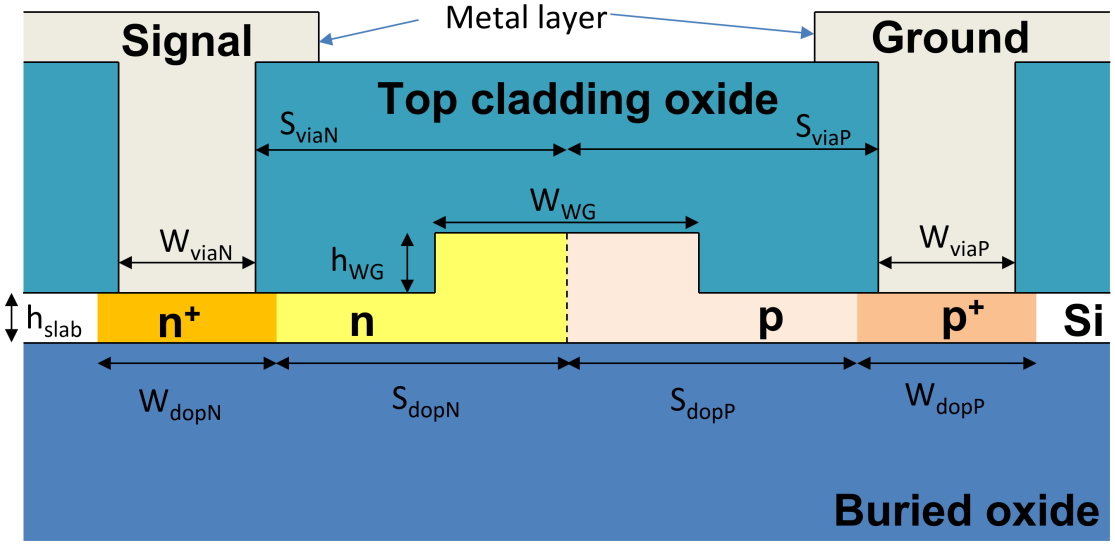

Figure 6.2: Cross section of the phase shifter for MZI and ring modulator.

The PN junction position is in the centre of the waveguide. The highly doped regions are 1.125 µm (S_{dopN}) for n+ doping and 1.025 µm (S_{dopP}) for p+ doping away from the junction. The reason for the asymmetrical separation is that p

type silicon absorbs less optical power than n type silicon for the same doping concentration, so it can be positioned closer to the waveguide core to enhance RF performance; while n type silicon has higher loss, it also has greater conductivity, so we can afford for it to be placed further away to reduce the overall loss. In this case, the simulated loss is below 20 dB/cm (at reverse bias of 4 V) and the device bandwidth is above 75 GHz. The target doping concentrations in the simulation are 3e17 cm^{-3}, 8.5e17 cm^{-3}, 1e20 cm^{-3} and 1e20 cm^{-3} for n, p, n+, and p+ regions respectively.

6.1.2 Results and Analysis

6.1.2.1 MZI modulator under carrier depletion

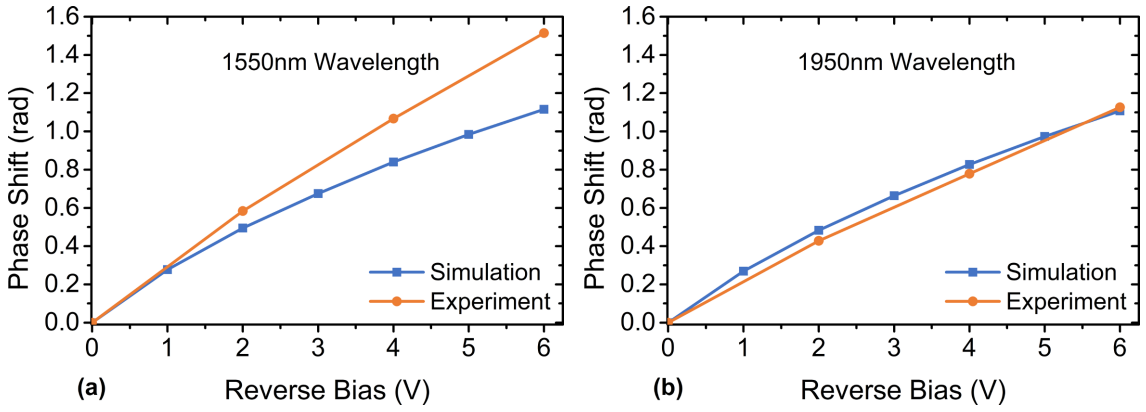

Figure 6.3: Experimental and simulated phase shift for a MZI modulator with 0.15 mm long phase shifter. (a) Phase shift at 1550 nm. (b) Phase shift at 1950 nm.

We tested and confirmed that the device transmits and modulates at both 1550 nm and 1950 nm. The modulation efficiency ($V_\pi \cdot L_\pi$) at a reverse bias of 4 V is 2.02 V·cm at 1550 nm and 2.68 V·cm at 1950 nm. In the experiment, the MZI modulator comprises a 1.5 mm long phase shifter and is driven in a single arm. The phase shift measured is shown in figure 6.3. It can be seen that the response agrees reasonably well with the simulation predictions for both wavelengths.

The high-speed RF characterization is performed by applying an amplified high-speed 2^7-1 psuedorandom-bit-stream OOK signal with a peak-to-peak amplitude of 4 V to a single arm only. A DC bias is applied simultaneously to the device via a bias-T. Combining the DC bias and the amplified RF signal, the overall scanning voltage is from -4.5V to -0.5V. At 1950 nm, an open eye is obtained at 8 Gbit/s

with an extinction ratio of 7.6 dB and 20 Gbit/s with extinction ratio of 5.8 dB, as shown in Figure 6.4. At 1550 nm, the device modulates at 20 Gbit/s with an extinction ratio of 10.3 dB, as in Figure 6.5(a), and 30 Gbit/s with an extinction ratio of 7.1 dB, as in Figure 6.5(b).

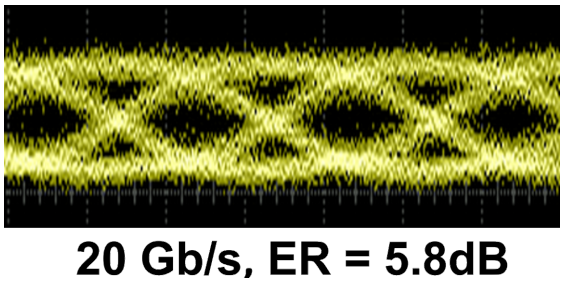

Figure 6.4: Eye diagram for MZI modulator at data rate of 20 Gb/s at 1950 nm wavelength. Extinction ratio is 5.8 dB.

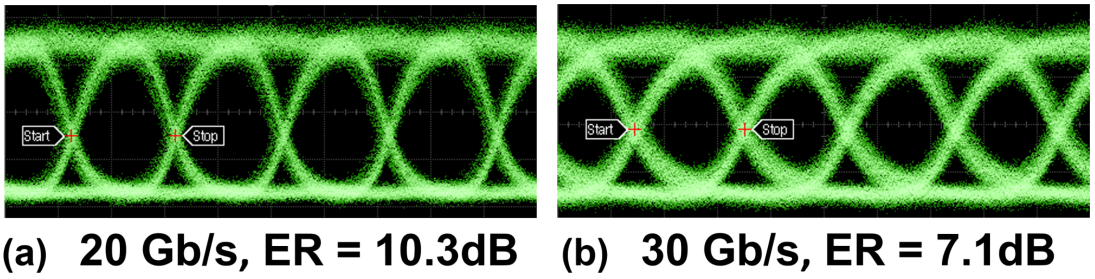

Figure 6.5: Eye diagram for MZI modulator at 1550 nm wavelength. (a) Data rate is 20 Gb/s, Extinction ratio is 10.3 dB. (b) Data rate is 30 Gb/s, Extinction ratio is 7.1 dB.

According to the simulation, the MZI modulator should give similar RF performance for both 1550 nm and 1950 nm wavelengths. The power budget of the system however is lower at 1950 nm, which renders the eye diagram at 1950 nm noisier than at 1550 nm. Furthermore, the insertion loss of the device at 1950 nm is measured as 13 dB which is significantly higher than was measured at 1550 nm (4 dB). The difference is partially due to the stronger plasma dispersion effect and a larger mode overlap with the highly-doped region in the 2 µm band. According to our simulations these factors only contribute to around 1 dB additional loss for a 1.5 mm long phase shifter. The remaining difference can be attributed to the loss from metal absorption in areas where the waveguide passes directly below the metal layer. The vertical separation between the top of the Si waveguide and the bottom of the metal layer is only 600 nm and because the optical mode at 1950 nm is substantially larger, there is greater overlap with the metal. This could be corrected in the next fabrication run either by increasing the silica top cladding

thickness to more than 1.0 µm, or by redesigning the mask to minimize the length of waveguide that passes directly underneath the metal.

Because of the bandwidth limit of the detector we were unable to obtain an eye diagram for data rates greater than 20 Gbit/s at 2 µm wavelength with this particular combination of modulator and detector, but since the bandwidth of the PN junction should be very similar at both wavelengths, we expect that the modulator can operate at higher data rates at 2 µm.

6.2 MZI Modulator Optimized at 2 µm

The next step is to build modulators dedicated to and optimized for 2 µm. This is a subsequent fabrication run from the last so experiences from previous designs have been applied to guide the new design and to avoid certain pitfalls.

6.2.1 Design

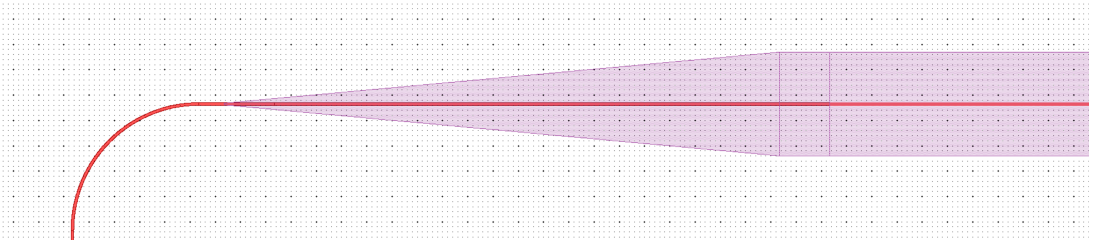

Figure 6.6: Taper structure that transitions from a strip waveguide on the left to a rib waveguide on the right. The dark red layer is the silicon waveguide core and the pale red layer is the slab region,

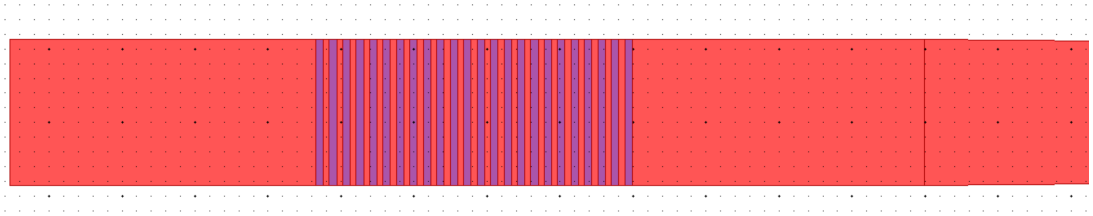

Figure 6.7: Mask design for grating coupler and part of taper down to the waveguide, working at 2 µm wavelength. The red layer is the fully etched waveguide layer, which defines protected region from the full 220 nm silicon etch. The purple layer is the gratings and it is to be etched down by 70 nm.

Table 6.1: Design parameters for 2µm SOI 1x2 MMI Splitter and 2x2 MMI 3dB Coupler. For the meaning of each parameter please refer to Figure 3.1.

	1x2 MMI Splitter	2x2 MMI Coupler
Etch Depth	220 nm (full etch)	220 nm (full etch)
W_{MMI}	6 µm	6 µm
W_{tap}	2.25 µm	2.25 µm
L_{tap}	10 µm	10 µm
W_{IO}	0.55 µm	0.55 µm
L_{MMI}	23.44 µm	92.19 µm
S	3.25 µm	3.25 µm

A similar 220 nm SOI platform has been chosen to leverage MPW runs. Since it is optimized solely for 2 µm operation, the MZM now includes gratings couplers and MMIs. Devices are fabricated on 220 nm SOI wafers with a 2 µm buried oxide (BOX) layer. The silicon rib waveguide is 550 nm wide and etched by 90 nm in the slab region. The top silicon dioxide cladding layer is at least 1 m thick, which should cope well with the swelled optical mode of 2 µm and minimize the mode overlap of metals on top of a waveguide. There is a transition taper that gradually converts the strip access waveguide to a rib waveguide in the active region, illustrated in Figure 6.6. The multi mode region of grating coupler is designed to have fully etched borders without slabs, the strip waveguide is used to bridge between is coupler and the rib waveguide in active region. Also as 2 µm wavelength has slightly more bend loss, the use of strip waveguide improves the bend loss. The grating coupler is optimized for 2 µm, the etch depth is 70nm, the pitch of the gratings is 0.92 µm, the duty cycle is 0.552 (ie for each period silicon width is 0.508 µm and the air gap width is 0.412 µm), the fully etched waveguide hosting the gratings is 10 µm in width. It takes a taper with length of 500 µm to taper down to the width of single mode strip waveguide, 550 nm. Table 6.1 summarises the design parameters for 1x2 and 2x2 MMI. For the meaning of each parameter please refer to Figure 3.1. In simulation, the insertion loss for each MMI is no bigger than 0.1 dB. These are used as coupler in the modulator MZI structure.

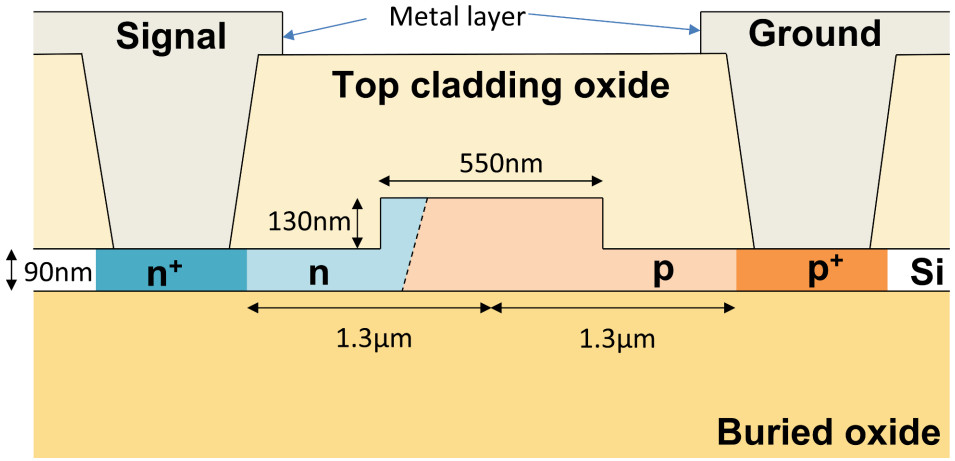

Figure 6.8: The phase shifter cross section of the 2 µm MZI modulator.

The phase shifter exploits the carrier depletion effect, and as shown in Figure 6.8 it comprises a PN junction. The device is fabricated in a CORNERSTONE multi-project wafer (MPW) run. Self-aligning lithography for n doping is used, as illustrated in Figure 6.9. The n-type dopant has been doped at an angle of 45 degrees. Therefore the junction appears angled and is positioned towards the n side. The self-alignment step helps reduce the junction position variation across devices introduced by the lithography [107]. Both highly doped regions p+ and n+ are 1.3 µm away from the junction. The target doping concentrations in the simulation are 3.8e17 cm^{-3}, 1.1e18 cm^{-3}, 1.5e17 cm^{-3}, 7.5e17 cm^{-3}, 1e20 cm^{-3} and 1e20 cm^{-3} for the p, n, p (rib), n (rib), p+, and n+ regions respectively. Please note that the n doping concentration is higher than doping which might be counter-intuitive to the fact that a unit amount of free electrons contributes large loss to holes. The reason for this traces back to the unique doping geometry resulting from the self-alignment process. Since the n doping is implanted from the side wall by implanting the dopant with an angle, it is geometrically highly away from the waveguide centre and comprise only a small fraction of the waveguide. This makes the optical mode overlap with the n region small and hence an acceptable level of loss is expected. To maximize the modulator efficiency however, the PN junction is needed to be as centred as possible to increase the interaction with the optical mode. By choosing a higher n doping and lower p doping, the depletion at p penetrates a lot deeper than n side, compensating the geometrically de-centred PN junction and effectively shifting it back towards the centre.

The Mach-Zehnder modulator contains two arms of the aforementioned phase shifter each with 2 mm length as shown in Figure 6.10(a). Various normalisation structures have been inserted. As in Figure 6.10(c), a short section of waveguide

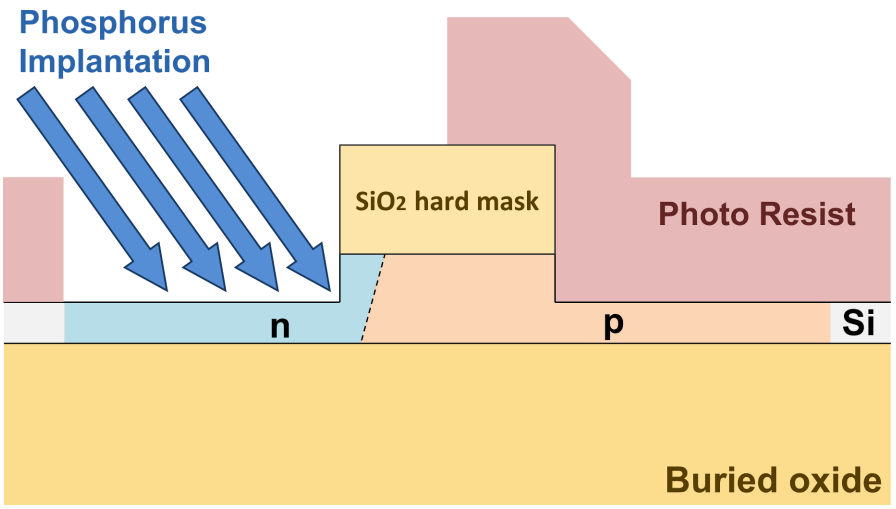

Figure 6.9: Self-aligned process used in Cornerstone PMW. Silica hard mask was used to etch the rib waveguide and it doubles as a mask for the phosphorous implantation. The photo resist edge can then be placed anywhere within the rib and the PN junction position will be independent of the resist edge. In order to make n-type dopant penetrating more into the waveguide, an implantation is performed at an angle and without any rotation.

taking the exact shape of the access waveguides of MZM is used to normalise the device insertion loss. A MZI structure is included as shown in Figure 6.10(b) to extract the optical loss from doping and metal electrode. And a doped MZI is also included as shown in Figure 6.10(d) to find out the optical loss due to via and metal electrode.

(a) Mach-Zehnder Modulator

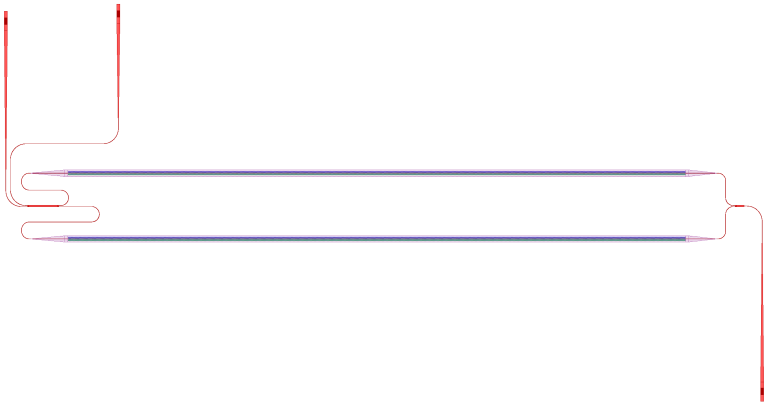

(b) Loss analysis structure will MZI and all dopings but without metal electrode.

(c) Loss analysis structure will bare passive MZI.

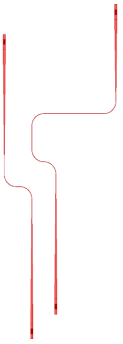

(d) Normalisation gratings and waveguide for calculating insertion loss.

Figure 6.10: Mask layout design for the modulator and normalisation reference structures used to analyse the loss contribution from different factors.

6.2.2 Updated Experimental setup

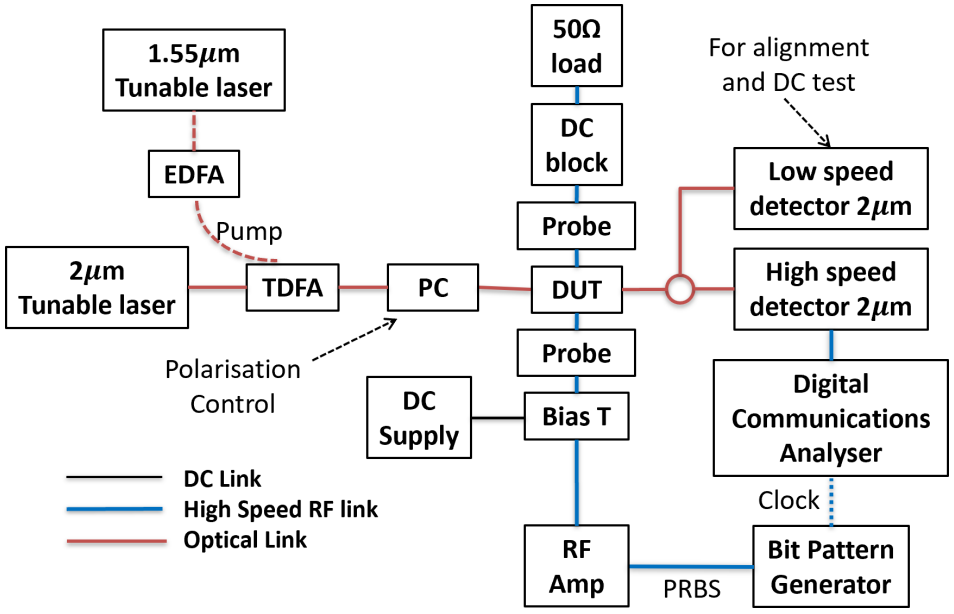

Figure 6.11: High-speed RF measurement set up for 2 µm wavelength modulator.

Compare to the previous 2 µm modulator characterisation setup, we have made several changes. The TDFA has been upgraded and it no longer uses polarisation maintaining fibres, therefore no polarisation controller is required between the seed laser and the TDFA. As the seed tunable laser power is relatively low, we found out it works more favourably to place the TDFA before the device. During the RF characterisation, a SHF 12104A Bit Pattern Generator (BPG) is used to generate a pseudorandom binary sequence (PRBS). The BPG is capable output 2 V peak-peak signal, so in the push-pull configuration no further RF amplifier is required.

As mentioned earlier, the high speed detector had a nominal bandwidth of >12.5 GHz, limiting the speed at which we could measure the modulator to around 25 Gbit/s with reduced extinction ratio.

6.2.3 Results

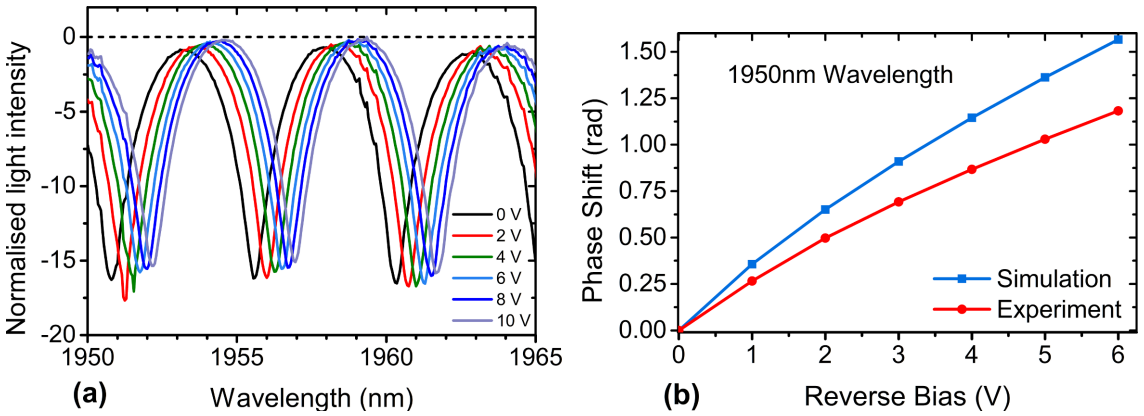

Figure 6.12: (a) Normalised light intensity from the MZM under 0 -6V bias voltages. (b) Experimental and simulated phase shift for a MZI modulator with 0.2 cm long phase shifter.

The modulation efficiency ($V_\pi \cdot L_\pi$) at a reverse bias of 4 V is 2.89 V·cm at 1950 nm. The experimental phase shift for the measured MZM that comprises a 2.0 mm long phase shifter is shown in figure 6.12. The simulated phase shift is also shown in the same graph. It can be seen that the response agrees reasonably well with the simulation predictions. According to the results from Figure 6.13, the insertion loss at zero bias voltage of the MZM with 2 mm phase shifter is 5.25 dB. A similar MZI without metal and via has also been tested to have an insertion loss of 4.96 dB. A similar MZI without doping and metal has a insertion loss of 1.25dB. We can therefore conclude that for the this CORNERSTONE MPW run, the vertical separation between the waveguide and metal is sufficient, and the main source of loss is attributed to doping.

The high speed RF characterization is carried out in a push-pull configuration. The DC bias is -4.5 V. A high-speed $2^7 - 1$ psuedorandom-bit-stream OOK signal direct output from the BPG with a peak-to-peak amplitude of 2 V is applied on each arm. Since the modulator has a unbalanced interferometer design, we can tune the wavelength of the 2 µm seed laser to shift the operation point to quadrature point. The wavelength picked is 1956.5 nm. The device modulates at 10 Gbit/s with an extinction ratio of 12.7 dB, as in figure 6.14(a), at 20 Gbit/s the extinction ratio is 10.3 dB, as in figure 6.14(b), and at 25 Gbit/s the extinction ratio is 6.25 dB, as in figure 6.14(c). Because of the bandwidth limit of the detector we were unable to obtain an eye diagram for data rates greater than 25 Gbit/s at 2 µm wavelength.

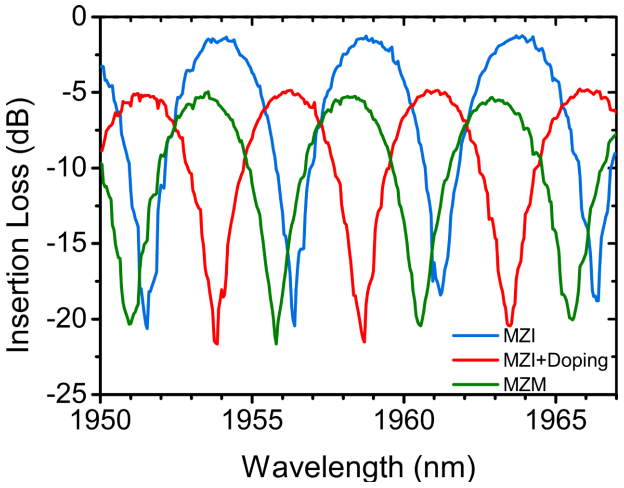

Figure 6.13: Insertion loss of the 2 mm MZM device and its reference structures.

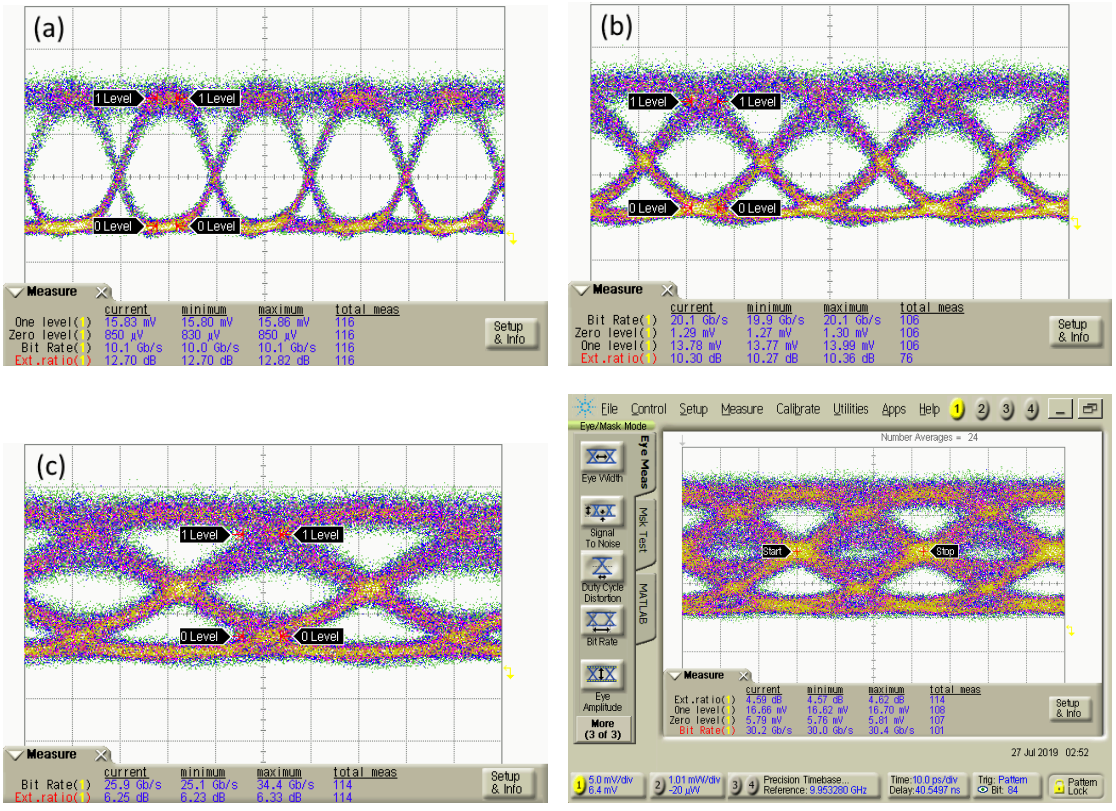

Figure 6.14: Eye diagram for MZI modulator at 1956.5 nm wavelength. (a) Data rate is 10 Gb/s, Extinction ratio is 12.7 dB. (b) Data rate is 20 Gb/s, extinction ratio is 10.3 dB. (c)Data rate is 25 Gb/s, extinction ratio is 6.25 dB.(d)Data rate is 30 Gb/s, without filtering the eye is not open.

6.3 Michelson Interferometer Modulator at 2 µm

A Michelson Interferometer modulator, as in Figure 6.15, retains some of the MZM's merits such as broad spectral bandwidth and temperature insensitivity, whilst maintaining a significantly smaller footprint, by doubling the effective optical path length on each arm. Successful silicon-based Michelson Interferometer modulator devices have been reported in the 1550 nm wavelength band [108]. We aim to explore the feasibility of Michelson Interferometer modulator at 2 µm and directly compare its performance against an equivalent MZM with twice as long a phase shifter length. The phase shifter design is the same as in the previous 2 mm long MZM, the details are specified in section 6.2.1.

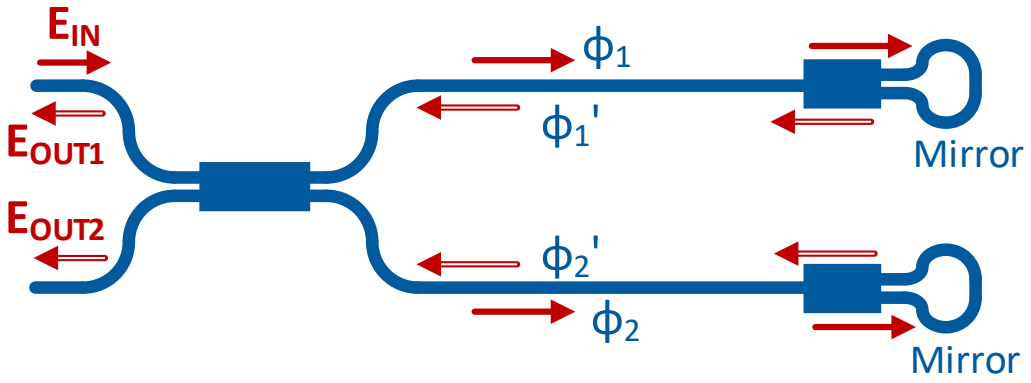

Figure 6.15: Schematic representation of a integrated Michelson Interferometer with looped mirror on both arms.

6.3.1 Design

The Michelson Interferometer modulator resembles a MZM, but it uses reflectors to reflect light back from both arms, as shown in Figure 6.16. Therefore, instead of combining and interfering the light from both arms at a second MMI, the Michelson interferometer uses the same MMI to split and combine the reflected light. Light then passes forth and back in total twice in the phase shifter which nearly doubles the efficiency of the modulator. The phase shifter length is 0.5 mm.

In our design we uses looped mirrors as reflectors. The looped mirror is advantageous in terms of reflectivity but introduces slightly larger optical delays compared to more compact mirrors such as metal reflector or 1-D photonics crystal mirror. Figure 6.17 illustrates the looped mirror design, it consists of a 1x2 MMI with parameters fromTable 6.1 and a section of waveguide arc. The total arc length is

319.26 µm. The scanner lithography mask layout for the Michelson Interferometer modulator is shown in Figure 6.16. We do have a alternative 1-D photonics crystal reflector design but it is not compatible with the DUV lithography process used with the MPW run, and hence not fabricated.

An MZM with the identical phase shifter design has been placed along side. The only apparent parameter difference is the phase shifter length, which is 1.0 mm, twice as long as the Michelson version.

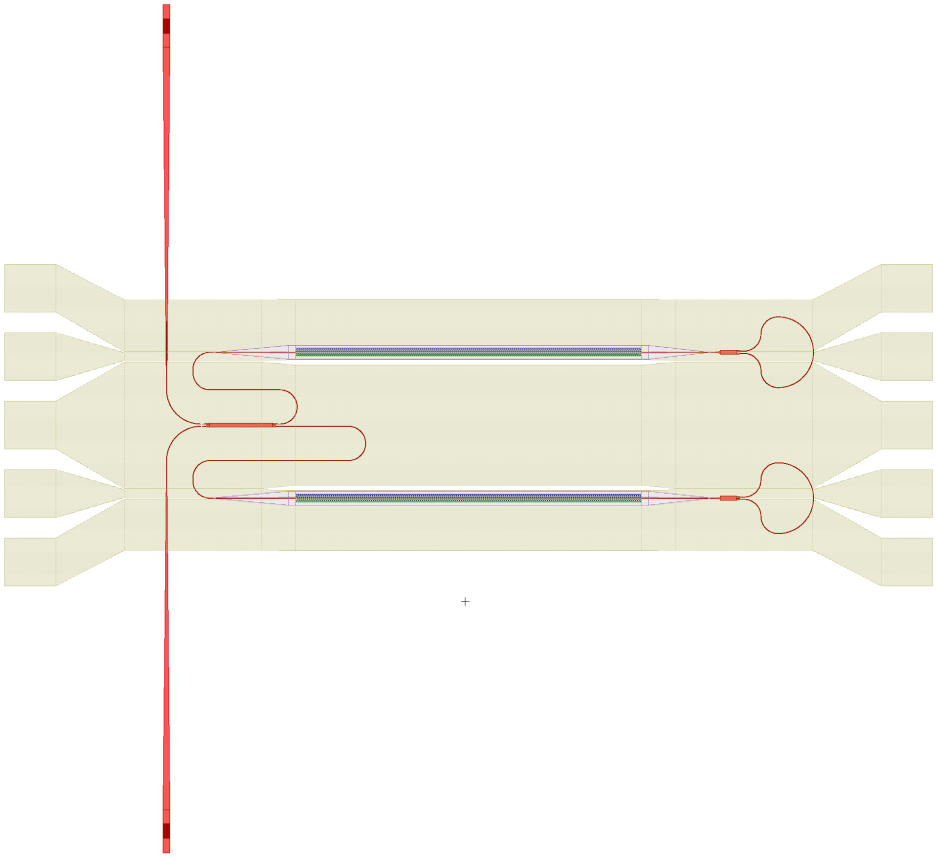

Figure 6.16: Scanner mask layout for the Michelson Interferometer modulator, with 0.5 mm phase shifter length, and looped mirror at one end.

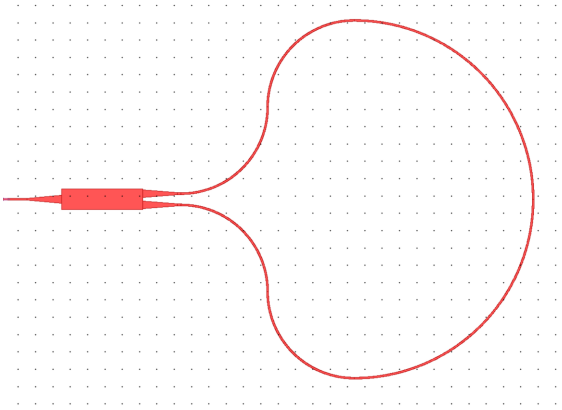

Figure 6.17: Scanner mask layout for the looped mirror design that has been used in the Michelson Interferometer.

6.3.2 Results and analysis

The Michelson Interferometer could produce significant back reflections. Hence an optical isolator between the output TDFA and the device is essential to prevent any disturbance of the TDFA and seed laser by the back reflection from the measured device.

In the DC regime, as shown in Figure 6.18, the 0.5 mm long Michelson modulator have almost identical modulation efficiency as with the 1 mm long MZM. They both have about half the efficiency of the 2 mm long MZM, which is as expected. At -4 V DC voltage, the 1 mm MZM has a measured modulation efficiency ($V_\pi \cdot L_\pi$) of 2.78 V·cm, the Michelson interferometer modulator due to its double passes, managed to provide around double the performance, reaching 1.36 V·cm.

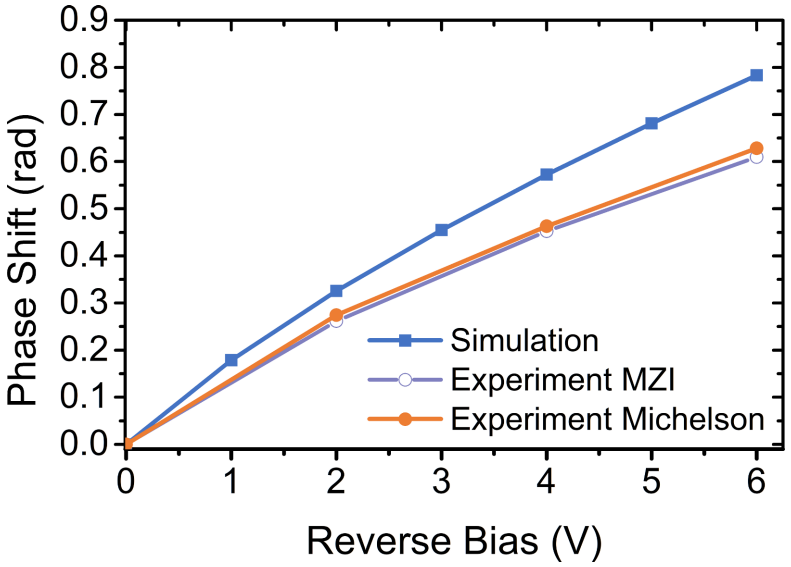

Figure 6.18: DC Modulation efficiency of a looped-mirror Michelson interferometer modulator with 0.5 mm phase shifter length and a Mach-Zehnder Interferometer modulator with 1.0 mm phase shifter length, compared against an ideal 1.0 mm active length MZM simulation.

The measurement from loss analysis structures shows a similar result as in MZM case. The insertion loss of a Michelson interferometer modulator at zero bias is approximately 3.9 dB. With waveguide loss of about 2.3 dB, doping contributing to about 1.0 dB and metal and via contributing to the remaining 0.6 dB.

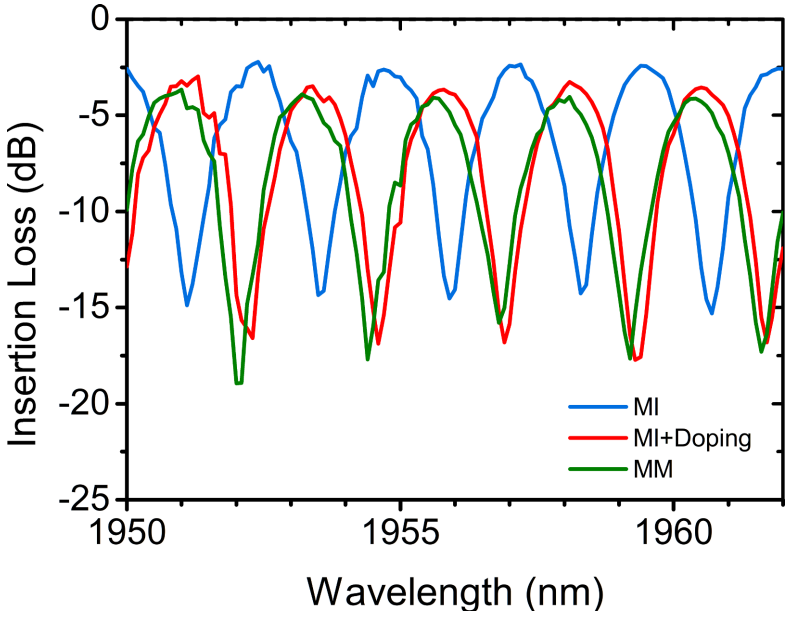

Figure 6.19: Insertion loss of the 0.5 mm Michelson interferometer modulator and its reference structures.

In the RF characterisation of the device, only single arm is used. The RF $2^7 - 1$ psuedorandom-bit-stream OOK signal output from BPG is amplified from 900 mV to 4 V peak-to-peak with an SHF S804A linear amplifier. The DC bias voltage is -2 V for the looped mirror Michelson modulator and -2.2 V for the MZM. To operating both device at the quadrature point, the wavelengths picked are 1954.10 nm for the Michelson modulator and 1955.10 nm for the MZM. The Michelson modulator with 0.5 mm long phase shifter gives extinction ratio of 1.45 dB at 8Gbit/s datarate, and extinction ratio of 0.8dB at 20 Gbit/s datarate. The MZM with 1.0 mm phase shifter gives extinction ratio of 1.98 dB at 8Gbit/s datarate, and extinction ratio of 1.97dB at 20 Gbit/s datarate. The 1 mm MZM is expected to provide lower extinction ratio than the 2 mm version tested earlier.

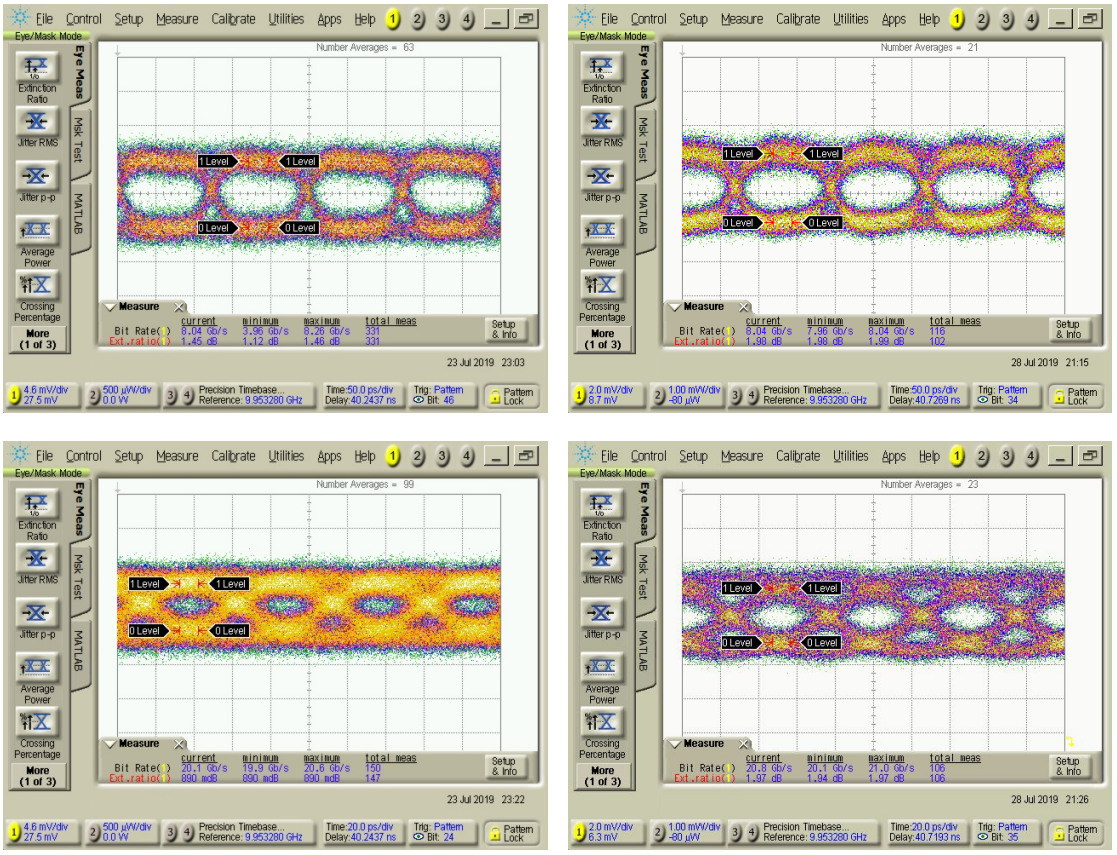

Figure 6.20: Eye diagram for 0.5 mm Michelson Interferometer modulator and 1 mm MZI modulator at 1950 nm wavelength.

The degradation of the extinction ratio at 20 Gbit/s datarate for the Michelson modulator is likely due to the mismatch of electrical and optical signal propagation, since the electrode is optimised for MZI and it is unchanged in Michelson. The effective index of RF electrical signal propagation matches closely to the optical group index. Thus in MZI, the electrical signal and optical signal co-propagate

and the modulation effect is accumulated along along the device. In the Michelson interferometer however, that condition does not hold. For moderately low datarate, there is still long enough electro-optical interaction time, but at high datarate for example in the case of 20Gbit/s, the RF modulation efficiency drops significantly.

6.4 PAM4 modulation at 2 µm

PAM4 uses 4 distinctive levels to encode 2 bits data per baud. For a system with limited bandwidth but relatively large extinction ratio, adopting PAM4 can essentially exploit the given bandwidth and offers overall higher data rate.

As industry moves to higher data rate, PAM4 has gradually become a essential standard in both optical (400G ethernet) and electrical (PCIE 4.0) fields.

6.4.1 Existing Optical PAM4 modulation architectures with MZMs

There are mainly three variants to generate optical PAM4 signal with MZMs.

Figure 6.21(a) illustrates a standard travelling waveguide MZM with a PAM4 electrical drive signal. The PAM4 electrical signal signal is normal generated by merging two NRZ signal with an electrical digital-to analogue converter (DAC). It is however very difficult to design a high performance DAC, or in terms of the price, not cost effective to be used in a real product. Furthermore, the electrical PAM4 signal quality is often inferior than a OOK signal, due to the constrains in electronics. Lastly, PAM4 requires high optical ER (at least 4 6 dB) than OOK for a similar BER performance. Therefore in a single MZM, the length needs to be extended; but this will have adverse effect in bandwidth.

The second option is to resort to a segmented MZM as shown in figure 6.21(b). Compared to the previous standard MZM, this shortens arm length on each segment and helps maintain a high bandwidth. On both segments it uses NRZ electrical driving signal , which involves no DAC and is easier to generate. Nevertheless, the segmented design is inherently subject to delay issue. The most significant bit (MSB) and most significant bit (LSB) driving signal need to be precisely tuned to

offset the delay in the optical link. Controlled delays in high datarate signal could be rather challenging to implement.

In Figure 6.21(c) a pair of parallel MZMs are used to implement a PAM4 transmitter. Both MZMs are identical in length, eliminating the delay issue. The MSB side then requires 6dB more amplified NRZ signal than the LSB side. Extra phase shifters (often thermal) need to be added to fine tune the phase of optical MSB signal and LSB signal so that they match each other. Since each modulator is only modulating half of the total input light, the driving peak-to-peak voltage would be higher than the segmented version to achieve the same ER.

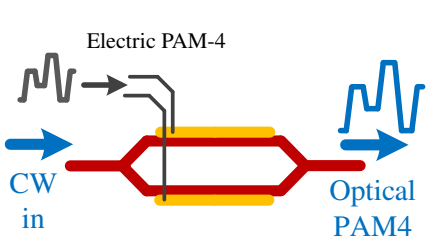

(a) Conventional MZM with electronic DAC.

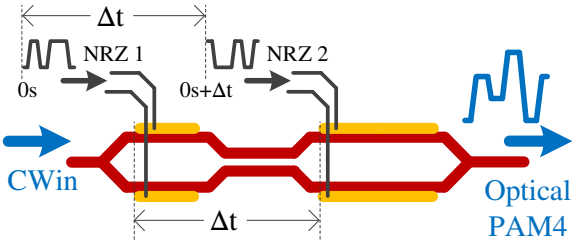

(b) Segmented MZM with dual NRZ drive signal.

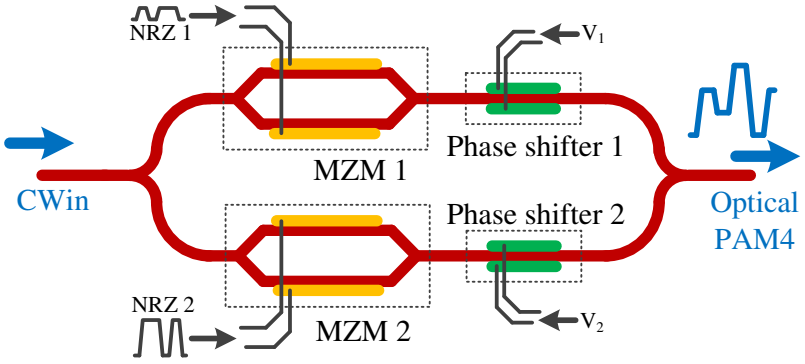

(c) Parallel MZM with regulated dual NRZ drive signal.

Figure 6.21: Three commonly used optical PAM4 modulation setups with MZMs.

6.4.2 Proposed Streamlined IMDD PAM4 with Dual-Drive MZM

We proposed a streamlined method to implement PAM4 transmitter with a standard MZM and minimal modification of current characterisation setup. As illustrated in figure 6.22 the PAM4 signal are generated by feeding NRZ electrical

signal with different peak-to-peak power into two arms of the MZM respectively. At the detection end, any phase information has been discarded and only intensity information are interpreted. The full link is called intensity-modulation, direct detection (IMDD).

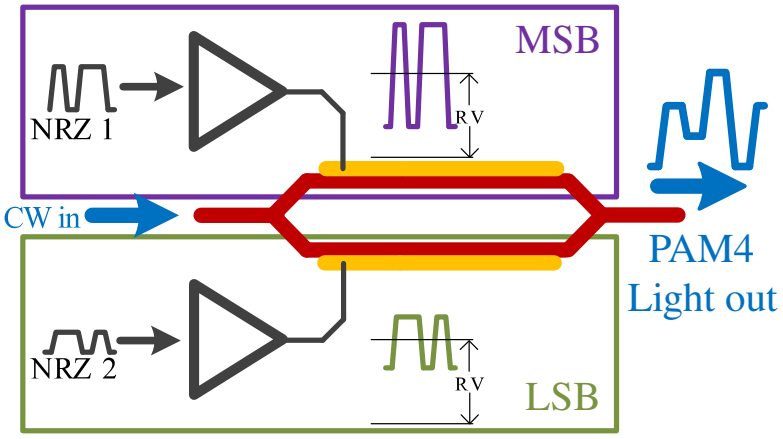

Figure 6.22: Proposed streamlined PAM4 modulation with dual-drive MZM. RV stands for reverse bias voltage. The upper arm NRZ 1 signal is been amplified 6 dB than the lower arm NRZ 2 signal. The more amplified drive signal carries the MSB and the other carries the LSB.

To proof the validity of the method, we need to analyse the system mathematically. Equation 3.12 provides the transfer function of a 1x1 MZI. To simplify the calculation, assume there is no loss in each arm and ignore the plasma dispersion effect induced loss.

$$\frac{E_{OUT}}{E_{IN}} \approx \tfrac{1}{2}[e^{j(\omega t-\phi_1)} + e^{j(\omega t-\phi_2)}] \tag{6.1}$$

$$= e^{j\frac{\phi 1+\phi 2}{2}} \cos\left(\tfrac{\phi 1-\phi 2}{2}\right) \tag{6.2}$$

where $\frac{\phi 1+\phi 2}{2}$ is the argument, which corresponds to the phase. And $\left|\cos\left(\frac{\phi 1-\phi 2}{2}\right)\right|$ is the magnitude, which corresponds to the amplitude. The phase shift on each arm ϕ_i consists inherent propagation delay ϕ_i' and phase shifter induced delay $\Delta\phi_i$. If assume the phase shifter response is linear, the phase change $\Delta\phi_i$ induced is linearly propositional to the reverse bias voltage V_i imposed.

$$\phi_1 = \phi_1' + \Delta\phi_1 \approx \phi_1' + \pi\frac{V_1}{V_\pi} \tag{6.3}$$

$$\phi_2 = \phi_2' + \Delta\phi_2 \approx \phi_1' + \pi\frac{V_2}{V_\pi} \tag{6.4}$$

When operating at the quadrature point, $\phi_1' - \phi_2' = \pi/2$. Therefore,

$$\frac{E_{OUT}}{E_{IN}} = \frac{1}{2} e^{j\left[\frac{\phi_1'+\phi_2'}{2} + \frac{\pi}{2V_\pi}(V_1+V_2)\right]} \cdot \cos\left[\frac{\phi_1' - \phi_2'}{2} + \frac{\pi}{2V_\pi}(V_1 - V_2)\right] \tag{6.5}$$

$$= \frac{1}{2} e^{j\left[\frac{\phi_1'+\phi_2'}{2} + \frac{\pi}{2V_\pi}(V_1+V_2)\right]} \cdot \cos\left[\frac{\pi}{4} + \frac{\pi}{2V_\pi}(V_1 - V_2)\right] \tag{6.6}$$

The reverse bias voltages V_i consists a DC bias voltage V_{bias_i} and a RF AC signal with peak-to-peak voltage of V_{pp_i}.

$$V_1 = V_{bias_1} \pm \frac{V_{pp_1}}{2} \tag{6.7}$$

$$V_2 = V_{bias_2} \pm \frac{V_{pp_2}}{2} \tag{6.8}$$

If $V_{pp_1} = 2V_pp$ $V_{pp_2} = V_pp$, V_1 and V_2 can then take these four distinctive levels.

$$V_1 - V_2 = \begin{cases} (V_{bias_1} - V_{bias_2}) + \frac{1}{2}(V_{pp_1} + V_{pp_2}) \\ (V_{bias_1} - V_{bias_2}) + \frac{1}{2}(V_{pp_1} - V_{pp_2}) \\ (V_{bias_1} - V_{bias_2}) + \frac{1}{2}(-V_{pp_1} + V_{pp_2}) \\ (V_{bias_1} - V_{bias_2}) + \frac{1}{2}(-V_{pp_1} - V_{pp_2}) \end{cases} \tag{6.9}$$

$$= \begin{cases} (V_{bias_1} - V_{bias_2}) + \frac{3}{2}V_{pp} \\ (V_{bias_1} - V_{bias_2}) + \frac{1}{2}V_{pp} \\ (V_{bias_1} - V_{bias_2}) - \frac{1}{2}V_{pp} \\ (V_{bias_1} - V_{bias_2}) - \frac{3}{2}V_{pp} \end{cases} \tag{6.10}$$

Since,

$$\frac{I_{OUT}}{I_{IN}} = \cos^2\left[\frac{\pi}{4} + \frac{\pi}{2V_\pi}(V_1 - V_2)\right] \tag{6.11}$$

Therefore the output intensity will also take four distinctive levels, if $\max(V_1 - V_2) < V_\pi/2$. The phase information however is lost in the detection, and the whole system is effectively a PAM4 transmission and detection. But due to the residue phase in each output level, coherent application is not possible with this scheme. The linearity of PAM can be improved by choosing a RF driving signal with moderately small peak-to-peak voltage V_{pp}.

Also if $V_{pp_1} = V_pp$ $V_{pp_2} = V_pp$, V_1 and V_2 can then take three distinctive levels.

$$V_1 - V_2 = \begin{cases} (V_{bias_1} - V_{bias_2}) + V_{pp} \\ (V_{bias_1} - V_{bias_2}) + 0 \\ (V_{bias_1} - V_{bias_2}) - V_{pp} \end{cases} \tag{6.12}$$

It is now a transmitter with a 3-level dual-binary signal output.

We now proved analytically the proposed dual drive single MZM PAM-4 is feasible. Please note, there are two major assumptions where we ignored the carrier effect induced loss and assumed phase shifter response against voltage is linear. However in real experiment, the actual response should not deviate too much from the prediction and the results should still remain valid.

We have build a rudimentary proof-of-principle simulation in Lumerical Interconnect to testify our argument. We feed two streams of 25 Gbit/s PRBS signals into each arm of a MZM. The bias voltage is -4 V on both arms and the peak-to-peak voltages of the RF signal are 1 V and 2 V, corresponding to least significant bit (LSB) and most significant bit (MSB) respectively. We have build a full coherent detector in order to capture both phase and amplitude information and hence to generate a constellation diagram. Figure 6.23(a) shows the raw constellation diagram showing all the transitions between states. And when plot the heat map of these transitions, we can clearly distinguish four PAM 4 states as in figure 6.23(b). The figure 6.24 shows the direct oscilloscope view of the signal output from such transmitter and it is indeed a optical PAM4 signal.

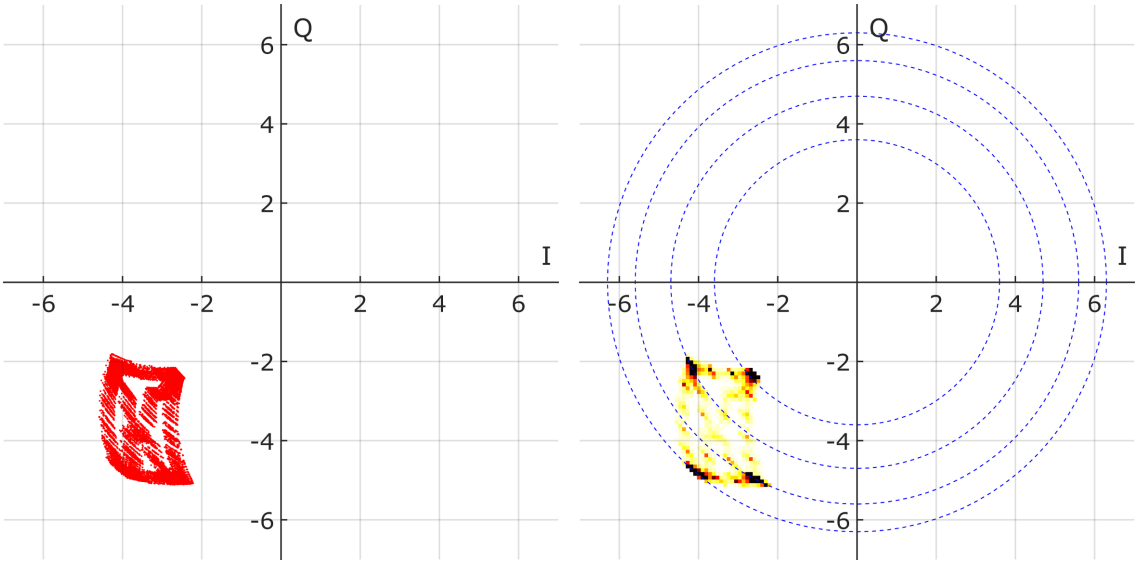

(a) Simulated raw constellation diagram of a received signal with all transitional trails.

(b) Simulated the heat scatter constellation diagram, emphasizes the four modulation states.

Figure 6.23: Simulated constellation diagram of signal output from a streamlined PAM4 transmitter.

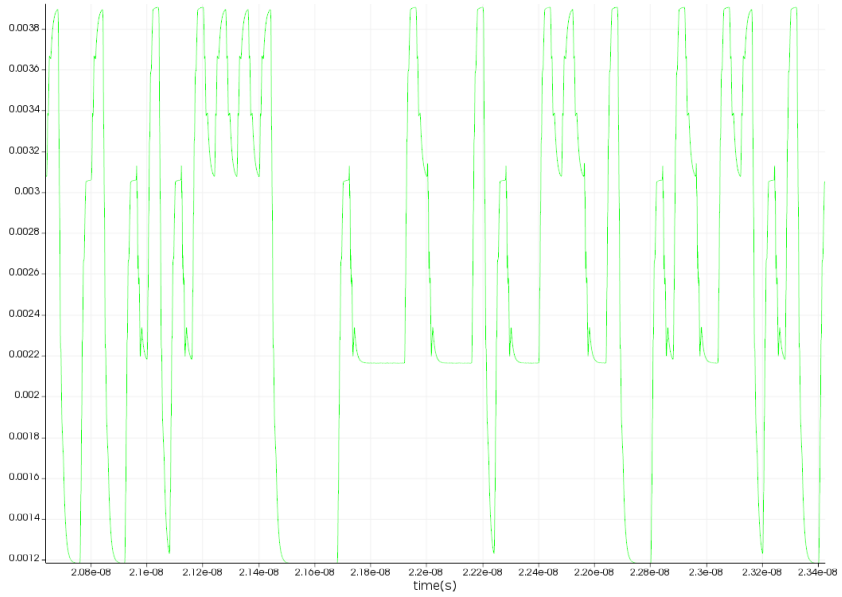

Figure 6.24: Simulated raw oscilloscope view of the signal output of the transmitter.

6.4.3 PAM4 Experiment Results in 2 µm

The same MZM with 2 mm phase shifter length in the previous chapter is used to perform the PAM4 experiment. We have applied -4.5 V reverse bias on both arms. The LSB arm are feed with RF signal with peak-to-peak voltage of 2 V directly output from the BPG. While for the MSB arm, the signal are amplified by the linear amplifier to provide 4 V peak-to-peak voltage. The two channels are independent $2^7 - 1$ PRBS signals. The delays between the channels are adjusted in BPG to compensate propagation delay difference in cable. The operation wavelength used is 1956.5 nm.

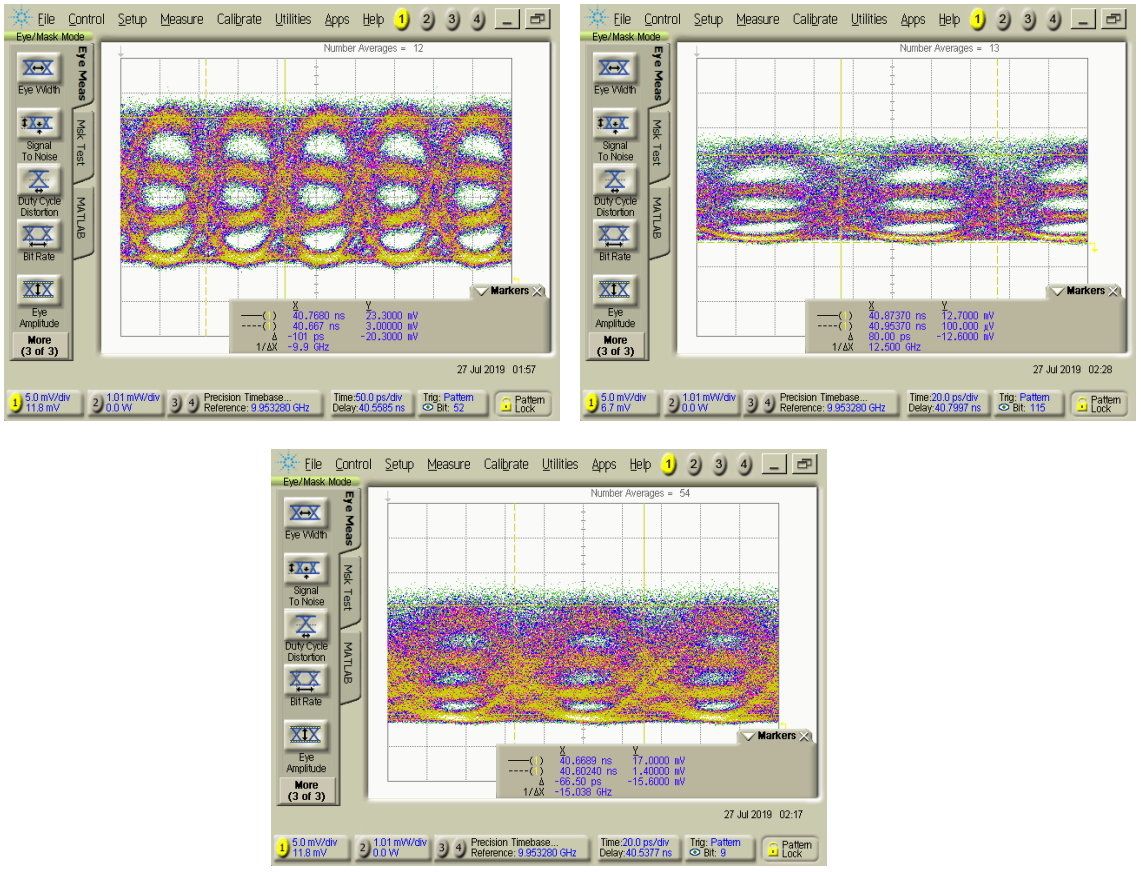

Figure 6.25: Eye diagram showing PAM4 operation of a 2 mm MZI modulator at 1950 nm wavelength.

Figure 6.25a shows the eye diagram of a 20 Gbit/s PAM4 signal (10 Gbaud/s), with an extinction ratio of $ER_{00-11} = 8.9dB$. Figure 6.25b shows the eye diagram of a 25Gbit/s PAM4 signal (12.5 Gbaud/s), with an extinction ratio of $ER_{00-11} = 20dB$. The usually high extinction ratio is due to the device is not operating at the quadrature point. We have also tested the 30 Gbit/s PAM 4 signal as in figure

6.25c, the eye however is not opening. PAM4 is a good way to improve the data rate when the bandwidth is limited but there is plenty of extinction ratio.

Chapter 7

Conclusions and Future work

7.1 Conclusions

The 2 µm communication window could be one of the solutions to mitigate the capacity crunch and it can be jointly used with other powerful method such as spatial division multiplexing to further delay the crunch. The 2 µm wavelength band is originally arisen from the predicted lowest loss window of the next-generation hollow core fibres, which offer low loss, low nonlinearity, low latency and many other advantages over incumbent SMF fibres. Those favourable properties can greatly improve SE compared to a SMF system. Also a larger optical bandwidth (1700-2200 nm), three times bandwidth of the C+L band, is becoming available thanks to thulium ion and holmium ion doped fibre amplifiers.

Multiple system-level 2 µm communication links have been demonstrated with the highest total capacity reaching 100 Gbit/s. The modulation however uses directly modulated III-V lasers with limited speed, or external commercial $LiNbO_3$ modulators with high drive voltages, or InP MZMs which are not CMOS compatible.

The 2 µm window has one extra vital advantage: compatibility with the silicon photonics SOI platform. Being CMOS compatible means full leverage of high yield low cost manufacturer capability. The small device size with silicon photonics also ensures that a system-level integration of a whole transceiver with WDM becomes feasible. In silicon, a 20 Gbit/s defect detector sensitive at 2 µm wavelength has previous been realised, which paves the way of a silicon based transceiver [21]. However, prior to our work in this thesis, there have been very few demonstrations

of high-speed silicon modulators. Only IBM has demonstrated a 3 Gbit/s carrier injection modulator operating at 2 µm wavelength in 2012.

The works in this thesis however have addressed this by demonstrating a 25 Gbit/s carrier depletion silicon MZM operating in the 2 µm wavelength band. A 25 Gbit/s PAM4 operation have also been demonstrated with the same device. We have also explored the Michelson interferometer modulator, and have achieved an efficiency of 1.36 V·cm and capable of operating at 20Gbit/s. In one of the older fabrication runs, we have also published a broadband device modulating both at 1550 nm and 1950 nm wavelengths. At 1950 nm it reaches a datarate of 20 Gbit/s and at 1550 nm it reaches a datarate of 30 Gbit/s. These works are, at the date of writing, the state of the art, as summarised in table 7.1.

Table 7.1: High-speed 2 µm-band silicon modulators including our works.

Ref	**$V_\pi \cdot L_\pi$**	**Type &format**	**Datarate &ER**	**Loss**	**Length**
2012 [50] IBM	1.2V·cm	Injection OOK	3Gb/s 8.9dB	9dB	1mm
2018 [101] This work 1	**2.68V·cm**	**Depletion OOK**	**20Gb/s 5.8dB**	**13dB**	**1.5mm**
2018 [101] This work 1	**4.4V·cm**	**Injection OOK**	**3Gb/s 2.3dB**	**-**	**Ring**
2018 [102] NTU	-	Depletion OOK	12.5Gb/s	3.2dB	1.5mm
2018 GFP McMaster	2.1V·cm	Depletion OOK	12.5Gb/s	-	Ring
2019 [103] This work 2	**2.89V·cm**	**Depletion OOK**	**25Gb/s 6.25dB**	**5.25dB**	**2mm**
2019 This work 2	**2.89V·cm**	**Depletion PAM4**	**25Gb/s**	**5.25dB**	**2mm**
2019 This work 2	**1.36V·cm**	**Depletion OOK**	**20Gb/s 0.8dB**	**3.9dB**	**0.5mm (Michelson)**

To successfully design a high-speed silicon MZM at 2 µm requires both understanding of high-speed MZM in general at transitional telecommunication wavelengths as well as the idiosyncrasies of 2 µm. By analysing the plasma dispersion modulation effect analytically and through numerical simulations, a bigger picture of

the modulator design trade-offs has been framed. In general an optimal design choice needs to starts from applications and specifications. A standard paradigm modulator design in PDK for example may not be suitable for all applications and operating conditions. Moreover, extra measures need to be taken when designing a 2 µm modulator, where the longer wavelength causes a swelled mode. Larger bend radius, higher metal and doping clearing spacing, larger waveguide dimensions are some of the things to be considered to mitigate issues. For example, the highly-doped regions and metal contact vias should be positioned further away to reduce the interaction between the 2 µm optical mode, resulting in an inferior RF performance. The plasma dispersion effect at 2 µm are higher than 1550 nm wavelength, however it is been counter-balanced by the longer wavelength, resulting to a similarly length devices at 2 µm and at 1550 nm.

7.2 Future works

In 220 nm silicon thickness SOI, due to the further placement of highly-doped region the RF performance of the 2 µm modulator is affected. This could however be mitigated by migrating to a thicker SOI platform with, for example, 340 nm or 500 nm silicon top layer. In these cases, given similar slab thickness as in the 220 nm SOI platform (to maintain similar RF properties), the optical mode retreats further from the slab region and is better confined in the rib part of the waveguide hence minimizing the interaction with the highly-doped regions in the slab. However, a thicker silicon layer may also imply a higher capacitance due to a larger depletion region area. The capacitance will also adversely affect the high-speed performance. Therefore 500 nm might be too thick and 340 nm may become the sweet spot. But all these are to be find out by actually designing such devices in various platforms in the future.

Another direction worth exploring is the WDM. AMMI is capable of a 4-channel CWMD with 20 nm channel spacing at 2 µm wavelength band. This can be added to an array of modulators to form a mini WDM system. Electrode design with awareness of flip-chip bonding of integrated driver are also worth developing. A further vision would be to design and fabricate a 2 µm silicon photonics transceiver with wire-bonding or flip-chip bonding integrated driver. The transceiver can then be used in various telecommunication transmission tests either back-to-back or going through kilometres of hollow-core fibres.

If exploring further beyond silicon, germanium becomes transparent in 2 µm wavelength, making germanium on insulator a promising platform. In germanium, the free carrier effect in 2 µm wavelength is on par with silicon. The higher refractive index of germanium provides a better refractive index contrast against the cladding and hence beneficial in terms of a tighter mode confinement. Therefore, we could expect higher high speed performance by being able to place the electrode and highly-doped region closer. Furthermore, a GeSn alloy opens up Franz-Keldysh effect by effectively shifting absorption edge right into the region of 2-3 µm wavelength. The absorption edge can be shifted by external electrical signal. An absorption type modulator based on the effect can offer a superior high-speed performance.

Other field effect modulation mechanism can also be exploited by adopting materials with high Pockels effect, such $LiNbO_3$, $BaTiO_3$ (BTO), $PbZr_xTi_{1-x}O_3$ (PZT). These material can be integrated into a silicon platform and providing not only solid high-speed performance due to lack of free carriers but also highly efficient modulation. The high efficiency implies a compact and low power consumption structure, which is highly desirable in numerous applications such as LIDAR.

Appendix A

MMI Theory

A.1 Multi-Mode Interference Device Self-Imaging Conditions

The self-imaging theory of multi-mode interference devices were initially published by Soldano et al. in 1995 [73] and thereafter forms the theoretical basis of all MMI devices as well as the later AMMI device family. Since many of the designs in this project depend on self-imaging theory as their underlying principle, it is worthy elaborating on it here.

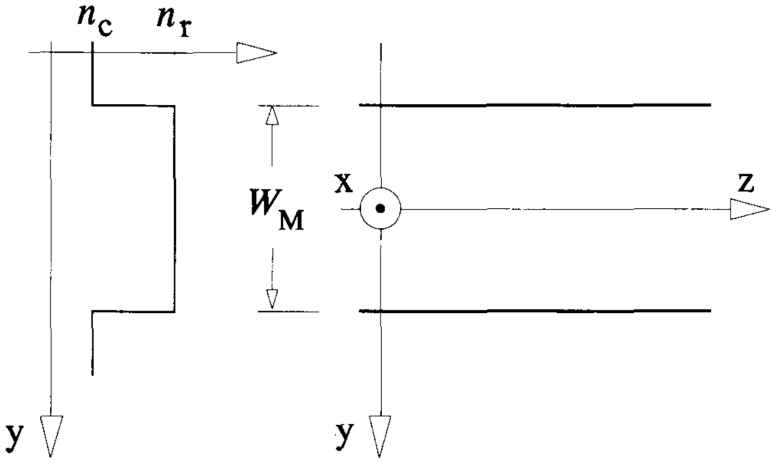

Figure A.1: The schematic of step-index multi-mode structure with core refractive index n_r and the cladding refractive index n_c. The width of the multi-mode waveguide is W_{MMI}. Extract from Soladno et al.[73]

The core of a multi-mode interference device (MMI) is a multi-mode waveguide. The Figure A.1 illustrates the generic features of such waveguide, with width

W_{MMI} and core refractive index n_r higher than the cladding refractive index n_c. Light propagates along positive z direction. The transverse mode pattern is in y direction with mode number $\upsilon = 0, 1, ...(m-1)$. According to light propagation theory in a waveguide, the lateral wavenumber, $k_{y\upsilon}$ and the propagation constant, $\beta_\upsilon = k_{z\upsilon}$ need to satisfy the following dispersion relationship: [73]

$$k_{y\upsilon}^2 + \beta_\upsilon^2 = k_0^2 n_r^2 \tag{A.1}$$

where,

$$k_0 = \frac{2\pi}{\lambda} \tag{A.2}$$

$$k_{y\upsilon} = \frac{(\upsilon+1)\pi}{W_{eff,\upsilon}} \tag{A.3}$$

where λ is the free-space propagation wavelength. And we assumed infinite x, so that the whole multi-mode section can be approximated to a 2D model. The term on the right hand side of the equation then uses n_r as refractive index. Whereas for actual 3D device one has to account for upper and lower cladding in x direction and instead use n_{eff} accordingly. $W_{eff,\upsilon}$ is the effective width of each mode, which is determined by Goos-Hähnchen shifts [109]. In Silicon-on-insulator waveguide, since the core/cladding contrast is high, the effective width of higher mode $W_{eff,\upsilon}$ is approximately equal to the effective width of fundamental mode $W_{eff,0}$. It can be further approximated to the multimode waveguide width W_{MMI}. ie:

$$W_{eff,\upsilon} \approx W_{eff,0} \approx W_{MMI} \tag{A.4}$$

Since also $k_{y\upsilon}^2 \ll k_0^2 n_r^2$, [73]

$$\beta_\upsilon \approx k_0 n_r - \frac{(\upsilon+1)^2\pi}{4 n_{eff} W_{eff,\upsilon}^2} \tag{A.5}$$

The beat length of the fundamental mode and first mode is then [73]

$$Ł_\pi = \frac{\pi}{\beta_0 - \beta_1} \approx \frac{4 n_{eff} W_{eff,\upsilon}^2}{3\lambda} \tag{A.6}$$

The arbitrary propagation constant difference from the fundamental mode can be simplified as: [73]

$$\beta_0 - \beta_\upsilon \approx \frac{\upsilon(\upsilon+2)\pi}{3L_\pi} \tag{A.7}$$

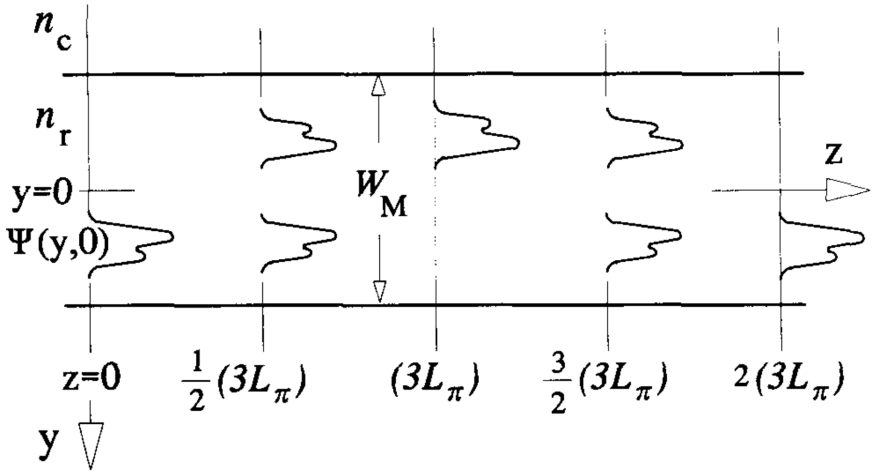

Figure A.2: The multi-mode waveguide width is W_{MMI} with core refractive index n_r and cladding refractive index n_c. The input signal $\Psi(y,0)$ propagates along the multi-mode waveguide exhibits a direct single image at $2(3L_\pi)$, and an inverted single image at $(3L_\pi)$ and two two-fold images at $\frac{1}{2}(3L_\pi)$ and $\frac{3}{2}(3L_\pi)$ respectively.

Consider an arbitrary input signal propagating from z=0 into the multi-mode waveguide. Since the all modes in the waveguide form an orthonormal basis, the input signal can thus be represented as the linear combination of those modes:

$$\Psi(y,0) = \sum_{v} c_v \psi_v(y) \tag{A.8}$$

where c_v is coefficients representing the portion of each mode in input signal. If we ignore the radiation mode and consider the confined mode only:

$$\Psi(y,0) = \sum_{v=0}^{m-1} c_v \psi_v(y) \tag{A.9}$$

As the signal propagates along z: [73]

$$\Psi(y,z,t) = \sum_{v=0}^{m-1} c_v \psi_v(y) \exp[j(\omega t - \beta_v z)] \tag{A.10}$$

If we drop the time dependence $\exp(j\omega t)$; and absorb the common fundamental mode term $\exp(-j\beta_0 z)$ into the constant c_v, Equation A.10 transforms into: [73]

$$\Psi(y,z) = \sum_{v=0}^{m-1} c_v \psi_v(y) \exp[j(\beta_0 - \beta_v) z] \tag{A.11}$$

Take $z = L$ and substitute Equation A.7 into Equation A.11: [73]

$$\Psi(y, L) = \sum_{\upsilon=0}^{m-1} c_\upsilon \psi_\upsilon(y) \exp\left[j\frac{\upsilon(\upsilon+2)\pi}{3L_\pi}L\right] \tag{A.12}$$

If meeting the following condition:

$$L = p(3L_\pi) \quad \text{where } p = 0, 1, 2.... \tag{A.13}$$

The exponential part of Equation A.12: [73]

$$\begin{cases} \exp\left[j\dfrac{\upsilon(\upsilon+2)\pi}{3L_\pi}L\right] & = 1 \qquad p \text{ is even} \\ \exp\left[j\dfrac{\upsilon(\upsilon+2)\pi}{3L_\pi}L\right] & = (-1)^\upsilon \quad p \text{ is odd} \end{cases} \tag{A.14}$$

Also due to the symmetry of transverse modes:

$$\psi_\upsilon(-y) = \begin{cases} \psi_\upsilon(y) & \upsilon \text{ is even} \\ -\psi_\upsilon(y) & \upsilon \text{ is odd} \end{cases} \quad \Longrightarrow \quad \psi_\upsilon(-y) = (-1)^\upsilon \psi_\upsilon(y) \tag{A.15}$$

Thus,

$$\begin{cases} \Psi\big(y, p(3L_\pi)\big) = \sum\limits_{\upsilon=0}^{m-1} c_\upsilon \psi_\upsilon(y) = \Psi(y, 0) & p \text{ is even} \\ \Psi\big(y, p(3L_\pi)\big) = \sum\limits_{\upsilon=0}^{m-1} c_\upsilon \psi_\upsilon(y)(-1)^\upsilon = \Psi(-y, 0) & p \text{ is odd} \end{cases} \tag{A.16}$$

Therefore in the case of $L = p(3L_\pi)$, the multi-mode waveguide produces direct self-image of input signal when p is even and produces inverted self-image when p is odd. (Figure A.2)

A.1.1 Multi-fold self-imaging conditions in MMI

Consider the two-fold self-imaging condition, when

$$L = \frac{p}{2}\big(3L_\pi\big) \quad \text{where } p = 1, 3, 5... \tag{A.17}$$

then [73]

$$\Psi\Big(y, \frac{p}{2}\big(3L_\pi\big)\Big) = \sum_{\upsilon=0}^{m-1} c_\upsilon \psi_\upsilon(y) \exp\Big[j\upsilon(\upsilon+2)p\Big(\frac{\pi}{2}\Big)\Big] \tag{A.18}$$

$$= \sum_{\upsilon \text{ even}} c_\upsilon \psi_\upsilon(y) + \sum_{\upsilon \text{ odd}} (-j)^p c_\upsilon \psi_\upsilon(y) \tag{A.19}$$

$$= \frac{1+(-j)^p}{2}\Psi(y,0) + \frac{1-(-j)^p}{2}\Psi(-y,0) \tag{A.20}$$

This implies at such distance $L = \frac{p}{2}\big(3L_\pi\big)$ where $p = 1, 3, 5...$, the multi-mode waveguide produces a direct image and an inverted image simultaneously and both with half of the power ($\frac{1}{\sqrt{2}}$ of the amplitude) as the original $\Psi(-y, 0)$ signal.

Soldano et al. further generalised the result and concluded that N-fold image will then be produced at [73]

$$L = \frac{p}{N}\big(3L_\pi\big) \tag{A.21}$$

where integer $p \geq 0$ and integer $N \geq 1$ have no common divisor. The power of each N-fold sub image will split the power equally among each other.

Substitute beat length from Equation A.6 into Equation A.21:

$$L = \frac{4Nn_{eff}W_{eff}^2}{\lambda} \approx \frac{4Nn_{eff}W_{MMI}^2}{\lambda} \tag{A.22}$$

Indeed in the case of N=2, as in Figure 3.2(b), the MMI is used as a 2x2 3dB coupler.

As indicagted in Figure 3.2, in the case of N=2, the MMI is used as 2x2 3dB coupler.

A.1.2 Restricted Interference with symmetrical mode only excitation

As for a 1x2 splitter implemented by MMI (with singled end in the middle of the MMI), the total device length can be effectively shortened into one quarter. This is achieved by exciting only the even symmetric modes in MMI. Because we have

$$mod_4[\upsilon(\upsilon+2)] = 0 \quad \text{where } \upsilon \text{ is even} \tag{A.23}$$

If we excite even symmetrical mode by placing the input access waveguide in the middle, single images of the input field will now be obtained at

$$L = \frac{p}{4}\left(3L_\pi\right) \quad \text{where } p = 0, 1, 2... \tag{A.24}$$

In general for N-fold images,

$$L = \frac{p}{4N}\left(3L_\pi\right) \quad \text{where } p = 0, 1, 2... \tag{A.25}$$

A.2 Bandwidth analysis of MMI

For a MMI with a given length L, the centre wavelength λ_c is as following:

$$\lambda_c = \frac{4Nn_{eff}W_{eff}^2}{L} \approx \frac{4Nn_{eff}W_{MMI}^2}{L} \tag{A.26}$$

Any wavelength deviation from the centre wavelength will cause excessive loss. According to equation A.22, the perturbation in wavelength is related to perturbation of length:

$$\frac{|\delta\lambda|}{\lambda_c} = \frac{|\delta L|}{L} \tag{A.27}$$

Each wavelength will have there own optimal MMI length, the image forms at the output of a MMI at different wavelength will be slightly in front or behind the output collecting waveguide (δ L). The loss can be calculated from the overlap factor between the image produced at the output of MMI and the optical mode of the collecting output waveguide. For a single mode input and output waveguide, the optical mode can be approximated by Gaussian beams with beam waist of w_0. At centre wavelength λ_c it focuses at length L. The wavelength perturbation will shift the focus position to L+δ. The excessive optical loss due to mode mismatch can then by found be calculating the overlap factor T. Besse et al [110] has analytically worked out, for excess loss $\alpha \equiv -10log_{10}(T)$,

$$|\delta L| \leq Z\frac{\pi n w_0^2}{\lambda_c} \tag{A.28}$$

with

$$Z = \sqrt{\frac{(4 - 5T^2) + \sqrt{(4 - 5T^2)^2 - 16T^2(T^2 - 1)}}{8T^2}} \tag{A.29}$$

The optical bandwidth $2|\delta\lambda|$ is then

$$2|\delta\lambda| \approx Z\frac{\pi n w_0^2}{L} \tag{A.30}$$

$$= Z\frac{\pi w_0^2 \lambda_c}{4NW_{MMI}^2} \tag{A.31}$$

For excessive insertion loss of 0.5 dB, the Z is approximately 0.5. Therefore the δL is about a quarter of the Rayleigh length of the Gaussian beam.

$$2|\delta\lambda| \approx \frac{\pi w_0^2 \lambda_c}{8NW_{MMI}^2} \quad \text{for excessive loss of 0.5 dB} \tag{A.32}$$

Appendix B

Plasma-dispersion Coefficients in Silicon

Table B.1: Coefficients for free-carrier electro-refraction/absorption effect in Silicon at 1.3μm-14μm [49]

Wavelength,	-Δn				Δa			
$\lambda(\mu\text{m})$	p (cm^3)	q	r (cm^3)	s	a (cm^2)	b	c (cm^2)	d
1.3	2.98E-22	1.016	1.25E-18	0.835	3.48E-22	1.229	1.02E-19	1.089
1.55	5.40E-22	1.011	1.53E-18	0.838	8.88E-21	1.167	5.84E-20	1.109
2.0	1.91E-21	0.992	2.28E-18	0.841	3.22E-20	1.149	6.21E-20	1.119
2.5	5.70E-21	0.976	5.19E-18	0.832	1.67E-20	1.169	8.08E-20	1.123
3.0	6.57E-21	0.981	3.62E-18	0.849	6.29E-21	1.193	3.40E-20	1.151
3.5	6.95E-21	0.986	9.28E-18	0.837	3.10E-21	1.210	6.05E-20	1.145
4.0	7.25E-21	0.991	9.99E-18	0.839	7.45E-22	1.245	5.43E-20	1.153
4.5	1.19E-20	0.985	1.29E-17	0.838	2.16E-22	1.277	5.58E-20	1.158
5.0	2.46E-20	0.973	2.03E-17	0.833	9.28E-23	1.299	6.65E-20	1.160
5.5	3.64E-20	0.968	3.31E-17	0.826	4.58E-23	1.319	8.53E-20	1.159
6.0	4.96E-20	0.965	6.91E-17	0.812	3.26E-23	1.330	1.53E-19	1.149
6.5	5.91E-20	0.964	8.23E-17	0.812	2.70E-23	1.338	1.22E-19	1.158
7.0	5.52E-20	0.969	1.15E-16	0.807	2.25E-23	1.345	1.29E-19	1.160
7.5	3.19E-20	0.984	4.81E-16	0.776	1.36E-23	1.359	9.99E-20	1.170
8.0	3.56E-20	0.984	7.44E-16	0.769	1.85E-23	1.354	1.32E-19	1.167
8.5	8.65E-20	0.966	7.11E-16	0.774	3.05E-23	1.345	1.57E-18	1.111
9.0	2.09E-19	0.948	5.29E-16	0.783	4.08E-23	1.340	1.45E-18	1.115
9.5	2.07E-19	0.951	9.72E-16	0.772	4.14E-23	1.341	1.70E-18	1.115
10.0	3.01E-19	0.944	1.22E-15	0.769	3.81E-23	1.344	1.25E-18	1.125
10.5	5.07E-19	0.934	1.16E-15	0.772	4.23E-23	1.344	8.14E-18	1.137
11.0	1.51E-19	0.965	3.16E-15	0.750	5.81E-23	1.338	1.55E-18	1.124
11.5	2.19E-19	0.958	1.51E-14	0.716	8.20E-23	1.331	4.81E-18	1.100
12.0	3.04E-19	0.953	2.71E-14	0.704	1.13E-22	1.325	4.72E-18	1.102
12.5	4.44E-19	0.912	2.65E-14	0.706	1.22E-22	1.324	2.09E-18	1.124
13.0	6.96E-19	0.936	2.94E-14	0.705	1.09E-22	1.328	1.16E-18	1.140
13.5	1.05E-18	0.928	6.85E-14	0.686	1.20E-22	1.327	2.01E-18	1.130
14.0	1.45E-18	0.922	2.60E-13	0.656	1.62E-22	1.321	7.52E-18	1.101

Bibliography

[1] D. J. Richardson, "Filling the light pipe," *Science*, vol. 330, pp. 327–328, oct 2010.

[2] A. Ellis, D. Rafique, and S. Sygletos, "Capacity in fiber optic communications-the case for a radically new fiber," in *IEEE Photonic Society 24th Annual Meeting*, IEEE, oct 2011.

[3] A. Chralyvy, "Plenary paper: The coming capacity crunch," in *35th European Conference on Optical Communication (ECOC)*, IEEE, sep 2009.

[4] "The 2019 ethernet roadmap." `https://ethernetalliance.org/technology/2019-roadmap/`, 2019. Accessed: 2019-12-09.

[5] H. Venghaus and N. Grote, eds., *Fibre Optic Communication*. Springer International Publishing, 2017.

[6] P. J. Roberts, F. Couny, H. Sabert, B. J. Mangan, D. P. Williams, L. Farr, M. W. Mason, A. Tomlinson, T. A. Birks, J. C. Knight, and P. S. J. Russell, "Ultimate low loss of hollow-core photonic crystal fibres," *Optics Express*, vol. 13, no. 1, p. 236, 2005.

[7] E. Desurvire, C. Kazmierski, F. Lelarge, X. Marcadet, A. Scavennec, F. Kish, D. Welch, R. Nagarajan, C. Joyner, R. Schneider, S. Corzine, M. Kato, P. Evans, M. Ziari, A. Dentai, J. Pleumeekers, R. Muthiah, S. Bigo, M. Nakazawa, D. Richardson, F. Poletti, M. Petrovich, S. Alam, W. Loh, and D. Payne, "Science and technology challenges in XXIst century optical communications," *Comptes Rendus Physique*, vol. 12, pp. 387–416, may 2011.

[8] K. Nagayama, M. Kakui, M. Matsui, T. Saitoh, and Y. Chigusa, "Ultra-low-loss (0.1484 dB/km) pure silica core fibre and extension of transmission distance," *Electronics Letters*, vol. 38, no. 20, p. 1168, 2002.

[9] C. J. Hensley, D. G. Ouzounov, A. L. Gaeta, N. Venkataraman, M. T. Gallagher, and K. W. Koch, "Silica-glass contribution to the effective nonlinearity of hollow-core photonic band-gap fibers," *Optics Express*, vol. 15, no. 6, p. 3507, 2007.

[10] F. Poletti, N. V. Wheeler, M. N. Petrovich, N. Baddela, E. N. Fokoua, J. R. Hayes, D. R. Gray, Z. Li, R. Slavík, and D. J. Richardson, "Towards high-capacity fibre-optic communications at the speed of light in vacuum," *Nature Photonics*, vol. 7, pp. 279–284, mar 2013.

[11] R. Slavík, G. Marra, E. N. Fokoua, N. Baddela, N. V. Wheeler, M. Petrovich, F. Poletti, and D. J. Richardson, "Ultralow thermal sensitivity of phase and propagation delay in hollow core optical fibres," *Scientific Reports*, vol. 5, oct 2015.

[12] L. Olanterä, C. Sigaud, J. Troska, F. Vasey, M. N. Petrovich, F. Poletti, N. V. Wheeler, J. P. Wooler, and D. J. Richardson, "Gamma irradiation of minimal latency hollow-core photonic bandgap fibres," *Journal of Instrumentation*, vol. 8, pp. C12010–C12010, dec 2013.

[13] F. Poletti, M. N. Petrovich, and D. J. Richardson, "Hollow-core photonic bandgap fibers: technology and applications," *Nanophotonics*, vol. 2, jan 2013.

[14] Z. Liu, Y. Chen, Z. Li, B. Kelly, R. Phelan, J. OCarroll, T. Bradley, J. P. Wooler, N. V. Wheeler, A. M. Heidt, T. Richter, C. Schubert, M. Becker, F. Poletti, M. N. Petrovich, S. ul Alam, D. J. Richardson, and R. Slavik, "High-capacity directly modulated optical transmitter for 2 µm spectral region," *Journal of Lightwave Technology*, vol. 33, pp. 1373–1379, apr 2015.

[15] Y. Chen, Z. Liu, S. R. Sandoghchi, G. T. Jasion, T. D. Bradley, E. N. Fokoua, J. R. Hayes, N. V. Wheeler, D. R. Gray, B. J. Mangan, R. Slavik, F. Poletti, M. N. Petrovich, and D. J. Richardson, "Multi-kilometer long, longitudinally uniform hollow core photonic bandgap fibers for broadband low latency data transmission," *J. Lightwave Technol.*, vol. 34, pp. 104–113, jan 2016.

[16] R. Soref, "Group IV photonics: Enabling 2 µm communications," *Nature Photonics*, vol. 9, pp. 358–359, may 2015.

[17] Z. Li, A. M. Heidt, N. Simakov, Y. Jung, J. M. O. Daniel, S. U. Alam, and D. J. Richardson, "Diode-pumped wideband thulium-doped fiber amplifiers

for optical communications in the 1800 – 2050 nm window," *Optics Express*, vol. 21, p. 26450, oct 2013.

[18] Z. Li, A. M. Heidt, J. M. O. Daniel, Y. Jung, S. U. Alam, and D. J. Richardson, "Thulium-doped fiber amplifier for optical communications at 2 µm," *Optics Express*, vol. 21, p. 9289, apr 2013.

[19] R. Soref, "Mid-infrared photonics in silicon and germanium," *Nature Photonics*, vol. 4, pp. 495–497, aug 2010.

[20] D. E. Hagan and A. P. Knights, "Mechanisms for optical loss in SOI waveguides for mid-infrared wavelengths around 2 µm," *Journal of Optics*, vol. 19, p. 025801, dec 2016.

[21] J. J. Ackert, D. J. Thomson, L. Shen, A. C. Peacock, P. E. Jessop, G. T. Reed, G. Z. Mashanovich, and A. P. Knights, "High-speed detection at two micrometres with monolithic silicon photodiodes," *Nature Photonics*, vol. 9, pp. 393–396, may 2015.

[22] C. E. Shannon, "A mathematical theory of communication," *Bell System Technical Journal*, vol. 27, pp. 379–423, jul 1948.

[23] D. J. Richardson, "New optical fibres for high-capacity optical communications," *Philosophical Transactions of the Royal Society A: Mathematical, Physical and Engineering Sciences*, vol. 374, p. 20140441, mar 2016.

[24] R. Johnson, P. Schniter, T. Endres, J. Behm, D. Brown, and R. Casas, "Blind equalization using the constant modulus criterion: a review," *Proceedings of the IEEE*, vol. 86, no. 10, pp. 1927–1950, 1998.

[25] F. Derr, "Coherent optical QPSK intradyne system: concept and digital receiver realization," *Journal of Lightwave Technology*, vol. 10, no. 9, pp. 1290–1296, 1992.

[26] E. Ip, A. P. T. Lau, D. J. F. Barros, and J. M. Kahn, "Coherent detection in optical fiber systems," *Optics Express*, vol. 16, no. 2, p. 753, 2008.

[27] P. P. Mitra and J. B. Stark, "Nonlinear limits to the information capacity of optical fibre communications," *Nature*, vol. 411, pp. 1027–1030, jun 2001.

[28] J. Tang, "A comparison study of the shannon channel capacity of various nonlinear optical fibers," *Journal of Lightwave Technology*, vol. 24, pp. 2070–2075, may 2006.

[29] J. Kahn and K.-P. Ho, "Spectral efficiency limits and modulation/detection techniques for DWDM systems," *IEEE Journal of Selected Topics in Quantum Electronics*, vol. 10, pp. 259–272, mar 2004.

[30] X. Chen and W. Shieh, "Closed-form expressions for nonlinear transmission performance of densely spaced coherent optical OFDM systems," *Optics Express*, vol. 18, p. 19039, aug 2010.

[31] D. Rafique and A. D. Ellis, "Impact of signal-ASE four-wave mixing on the effectiveness of digital back-propagation in 112 gb/s PM-QPSK systems," *Optics Express*, vol. 19, p. 3449, feb 2011.

[32] A. Ellis, J. Zhao, and D. Cotter, "Approaching the non-linear shannon limit," *Journal of Lightwave Technology*, vol. 28, pp. 423–433, feb 2010.

[33] M. Lauermann, R. Going, R. Maher, M. Lu, W. Ko, P. Studenkov, J. Ferrara, A. Hosseini, S. Corzine, J. Rahn, M. Kuntz, H. Tsai, A. Karanicolas, P. Evans, V. Lal, D. Welch, and F. Kish, "Multi-channel, widely-tunable coherent transmitter and receiver PICs operating at 88gbaud/16-QAM," in *Optical Fiber Communication Conference Postdeadline Papers*, OSA, 2017.

[34] J. X. Cai, H. G. Batshon, M. V. Mazurczyk, C. R. Davidson, O. V. Sinkin, D. Wang, M. Paskov, W. W. Patterson, M. A. Bolshtyansky, and D. G. Foursa, "94.9 tb/s single mode capacity demonstration over 1,900 km with c+l EDFAs and coded modulation," in *2018 European Conference on Optical Communication (ECOC)*, IEEE, sep 2018.

[35] "Taking zblan optical fiber production to space." `https://www.issnationallab.org/blog/taking-zblan-optical-fiber-production-to-space/`, 2018. Accessed: 2020-12-23.

[36] Y. Jung, V. A. J. M. Sleiffer, N. Baddela, M. N. Petrovich, J. R. Hayes, N. V. Wheeler, D. R. Gray, E. N. Fokoua, J. P. Wooler, N. H.-L. Wong, F. Parmigiani, S. U. Alam, J. Surof, M. Kuschnerov, V. Veljanovski, H. de Waardt, F. Poletti, and D. J. Richardson, "First demonstration of a broadband 37-cell hollow core photonic bandgap fiber and its application to high capacity mode division multiplexing," in *Optical Fiber Communication Conference/-National Fiber Optic Engineers Conference 2013*, OSA, 2013.

[37] B. J. Mangan, L. Farr, A. Langford, P. J. Roberts, D. P. Williams, F. Couny, M. Lawman, M. Mason, S. Coupland, R. Flea, H. Sabert, T. A. Birks, J. C.

Knight, and P. S. J. Russell, "Low loss (1.7 db/km) hollow core photonic bandgap fiber," in *Optical Fiber Communication Conference, 2004. OFC 2004*, vol. 2, pp. 3 pp. vol.2–, Feb 2004.

[38] N. V. Wheeler, M. N. Petrovich, R. Slavik, N. K. Baddela, E. R. N. Fokoua, J. R. Hayes, D. Gray, F. Poletti, and D. Richardson, "Wide-bandwidth, low-loss, 19-cell hollow core photonic band gap fiber and its potential for low latency data transmission," in *National Fiber Optic Engineers Conference*, OSA, 2012.

[39] M. H. Frosz, J. Nold, T. Weiss, A. Stefani, F. Babic, S. Rammler, and P. S. J. Russell, "Five-ring hollow-core photonic crystal fiber with 18 dB/km loss," *Optics Letters*, vol. 38, p. 2215, jun 2013.

[40] R. van Uden, C. Okonkwo, H. Chen, N. Wheeler, F. Poletti, M. Petrovich, D. Richardson, H. de Waardt, and A. Koonen, "8.96tb/s (32×28gbaud×32qam) transmission over 0.95 km 19 cell hollow-core photonic bandgap fiber," in *Optical Fiber Communication Conference*, OSA, 2014.

[41] H. Zhang, N. Kavanagh, Z. Li, J. Zhao, N. Ye, Y. Chen, N. V. Wheeler, J. P. Wooler, J. R. Hayes, S. R. Sandoghchi, F. Poletti, M. N. Petrovich, S. U. Alam, R. Phelan, J. O'Carroll, B. Kelly, L. Grüner-Nielsen, D. J. Richardson, B. Corbett, and F. C. G. Gunning, "100 Gbit/s WDM transmission at 2 µm transmission studies in both low-loss hollow core photonic bandgap fiber and solid core fiber," *Optics Express*, vol. 23, p. 4946, feb 2015.

[42] B. J. Mangan, M. Kuschnerov, J. W. Nicholson, J. M. Fini, L. Meng, R. S. Windeler, E. M. Monberg, A. DeSantolo, K. Mukasa, V. Mikhailov, M. Hermann, and U. Feiste, "First demonstration of hollow-core fiber for intra data center low latency connectivity with a commercial 100gb/s interface," in *Optical Fiber Communication Conference*, OSA, 2015.

[43] E. N. Fokoua, M. N. Petrovich, T. Bradley, F. Poletti, D. J. Richardson, and R. Slavík, "How to make the propagation time through an optical fiber fully insensitive to temperature variations," *Optica*, vol. 4, p. 659, jun 2017.

[44] P. J. Winzer, "Transmission system capacity scaling through space-division multiplexing: a techno-economic perspective," in *Optical Fiber Telecommunications VII*, pp. 337–369, Elsevier, 2020.

[45] S. fei Gao, Y. ying Wang, W. Ding, D. liang Jiang, S. Gu, X. Zhang, and P. Wang, "Hollow-core conjoined-tube negative-curvature fibre with ultralow loss," *Nature Communications*, vol. 9, jul 2018.

[46] M. S. Habib, E. Antonio-Lopez, C. Markos, A. Schülzgen, and R. Amezcua-Correa, "Single mode, low-loss 5-tube nested hollow-core anti-resonant fiber," in *Optical Fiber Communication Conference (OFC) 2019*, OSA, 2019.

[47] G. T. Reed, G. Z. Mashanovich, F. Y. Gardes, M. Nedeljkovic, Y. Hu, D. J. Thomson, K. Li, P. R. Wilson, S.-W. Chen, and S. S. Hsu, "Recent breakthroughs in carrier depletion based silicon optical modulators," *Nanophotonics*, vol. 3, jan 2014.

[48] X. Xiao, M. Li, L. Wang, D. Chen, Q. Yang, and S. Yu, "High speed silicon photonic modulators," in *Optical Fiber Communication Conference*, OSA, 2017.

[49] M. Nedeljkovic, R. Soref, and G. Z. Mashanovich, "Free-carrier electrorefraction and electroabsorption modulation predictions for silicon over the 1-14-µm infrared wavelength range," *IEEE Photonics J.*, vol. 3, pp. 1171–1180, dec 2011.

[50] M. A. V. Camp, S. Assefa, D. M. Gill, T. Barwicz, S. M. Shank, P. M. Rice, T. Topuria, and W. M. J. Green, "Demonstration of electrooptic modulation at 2165nm using a silicon mach-zehnder interferometer," *Opt. Express*, vol. 20, p. 28009, dec 2012.

[51] T. Li, M. Nedeljkovic, N. Hattasan, A. Z. Khokhar, S. A. Reynolds, S. Stankovic, M. Banakar, W. Cao, Z. Qu, C. G. Littlejohns, J. S. Penades, K. Grabska, L. Mastronardi, D. J. Thomson, F. Y. Gardes, G. T. Reed, H. Wu, Z. Zhou, and G. Z. Mashanovich, "Mid-infrared Ge-on-Si electro-absorption modulator," in *2017 IEEE 14th International Conference on Group IV Photonics (GFP)*, IEEE, aug 2017.

[52] D. J. Thomson, L. Shen, J. J. Ackert, E. Huante-Ceron, A. P. Knights, M. Nedeljkovic, A. C. Peacock, and G. Z. Mashanovich, "Optical detection and modulation at 2 µm-25 µm in silicon," *Optics Express*, vol. 22, p. 10825, apr 2014.

[53] J. Kang, M. Takenaka, and S. Takagi, "Novel Ge waveguide platform on Ge-on-insulator wafer for mid-infrared photonic integrated circuits," *Optics Express*, vol. 24, p. 11855, may 2016.

[54] M. Nedeljkovic, S. Stankovic, C. J. Mitchell, A. Z. Khokhar, S. A. Reynolds, D. J. Thomson, F. Y. Gardes, C. G. Littlejohns, G. T. Reed, and G. Z. Mashanovich, "Mid-infrared thermo-optic modulators in SoI," *IEEE Photonics Technology Letters*, vol. 26, pp. 1352–1355, jul 2014.

[55] J. Chiles and S. Fathpour, "Mid-infrared integrated waveguide modulators based on silicon-on-lithium-niobate photonics," *Optica*, vol. 1, p. 350, nov 2014.

[56] S. Liu, K. Xu, Q. Song, Z. Cheng, and H. Tsang, "Design of mid-infrared electro-optic modulators based on aluminum nitride waveguides," *Journal of Lightwave Technology*, pp. 1–1, 2016.

[57] N. Yahyaoui, N. Sfina, J.-L. Lazzari, A. Bournel, and M. Said, "Stark shift of the absorption spectra in ge/ge1-xsnx/ge type-i single qw cell for mid-wavelength infra-red modulators," *Superlattices and Microstructures*, vol. 85, pp. 629–637, sep 2015.

[58] H. Zhang, M. Gleeson, N. Ye, N. Pavarelli, X. Ouyang, J. Zhao, N. Kavanagh, C. Robert, H. Yang, P. E. Morrissey, K. Thomas, A. Gocalinska, Y. Chen, T. Bradley, J. P. Wooler, J. R. Hayes, E. N. Fokoua, Z. Li, S. U. Alam, F. Poletti, M. N. Petrovich, D. J. Richardson, B. Kelly, J. O'Carroll, R. Phelan, E. Pelucchi, P. O'Brien, F. Peters, B. Corbett, and F. Gunning, "Dense WDM transmission at 2 µm enabled by an arrayed waveguide grating," *Optics Letters*, vol. 40, p. 3308, jul 2015.

[59] L. Shen, N. Healy, C. J. Mitchell, J. S. Penades, M. Nedeljkovic, G. Z. Mashanovich, and A. C. Peacock, "Mid-infrared all-optical modulation in low-loss germanium-on-silicon waveguides," *Optics Letters*, vol. 40, p. 268, jan 2015.

[60] S. J. Park, A. Zakar, V. L. Zerova, D. Chekulaev, L. T. Canham, and A. Kaplan, "All-optical modulation in mid-wavelength infrared using porous si membranes," *Scientific Reports*, vol. 6, jul 2016.

[61] R. Phelan, J. O'Carroll, D. Byrne, C. Herbert, J. Somers, and B. Kelly, "In0.75ga0.25asinp multiple quantum-well discrete-mode laser diode emitting at 2 µm," *IEEE Photonics Technology Letters*, vol. 24, pp. 652–654, apr 2012.

[62] Z. Li, S. U. Alam, Y. Jung, A. M. Heidt, and D. J. Richardson, "All-fiber, ultra-wideband tunable laser at 2 µm," *Optics Letters*, vol. 38, p. 4739, nov 2013.

[63] N. Ye, M. R. Gleeson, M. U. Sadiq, B. Roycroft, C. Robert, H. Yang, H. Zhang, P. E. Morrissey, N. M. Suibhne, K. Thomas, A. Gocalinska, E. Pelucchi, R. Phelan, B. Kelly, J. OCarroll, F. H. Peters, F. C. G. Gunning, and B. Corbett, "InP-based active and passive components for communication systems at 2 µm," *Journal of Lightwave Technology*, vol. 33, pp. 971–975, mar 2015.

[64] N. Ye, M. Gleeson, H. Yang, H. Zhang, B. Roycroft, K. Thomas, A. Gocalinska, E. Pelucchi, Z. Li, D. Richardson, H. Chen, A. M. J. Koonen, W. Jia, J. Zhao, F. G. Gunning, F. Peters, and B. Corbett, "Demonstration of 90 optical hybrid at 2 µm wavelength range based on 4x4 MMI using diluted waveguide," in *2014 The European Conference on Optical Communication (ECOC)*, pp. 1–3, Sept 2014.

[65] H. Yang, N. Ye, M. Manganaro, A. Gocalinska, K. Thomas, E. Pelucchi, B. Roycroft, F. H. Peters, and B. Corbett, "High speed AlInGaAs/InGaAs quantum well waveguide photodiode for wavelengths around 2 microns," in *2012 International Conference on Indium Phosphide and Related Materials*, Institute of Electrical and Electronics Engineers (IEEE), aug 2012.

[66] H. Yang, B. Kelly, W. Han, F. Gunning, B. Corbett, R. Phelan, J. O'Carroll, F. Peters, X. Wang, N. Nudds, P. O'Brien, N. Ye, and N. MacSuibhne, "Butterfly packaged high-speed and low leakage InGaAs quantum well photodiode for 2000nm wavelength systems," *Electronics Letters*, vol. 49, pp. 281–282, feb 2013.

[67] N. Ye, H. Yang, M. Gleeson, N. Pavarelli, H. Zhang, J. O'Callaghan, W. Han, N. Nudds, S. Collins, A. Gocalinska, E. Pelucchi, P. O'Brien, F. C. G. Gunning, F. H. Peters, and B. Corbett, "InGaAs surface normal photodiode for 2 µm optical communication systems," *IEEE Photonics Technology Letters*, vol. 27, pp. 1469–1472, July 2015.

[68] Y. Chen, Z. Xie, J. Huang, Z. Deng, and B. Chen, "High-speed uni-traveling carrier photodiode for 2 µm wavelength application," *Optica*, vol. 6, p. 884, jul 2019.

[69] H. Zhang, Z. Li, N. Kavanagh, J. Zhao, N. Ye, Y. Chen, N. V. Wheeler, J. P. Wooler, J. R. Hayes, S. R. Sandoghchi, F. Poletti, M. N. Petrovich,

S. U. Alam, R. Phelan, J. O'Carroll, B. Kelly, D. J. Richardson, B. Corbett, and F. C. G. Gunning, "81 Gb/s WDM transmission at 2 µm over 1.15 km of low-loss hollow core photonic bandgap fiber," in *2014 The European Conference on Optical Communication (ECOC)*, Institute of Electrical and Electronics Engineers (IEEE), sep 2014.

[70] M. N. Petrovich, F. Poletti, J. P. Wooler, A. Heidt, N. Baddela, Z. Li, D. Gray, R. Slavík, F. Parmigiani, N. Wheeler, J. Hayes, E. Numkam, L. Grűner-Nielsen, B. Pálsdóttir, R. Phelan, B. Kelly, J. O'Carroll, M. Becker, N. MacSuibhne, J. Zhao, F. G. Gunning, A. Ellis, P. Petropoulos, S. Alam, and D. Richardson, "Demonstration of amplified data transmission at 2 µm in a low-loss wide bandwidth hollow core photonic bandgap fiber," *Optics Express*, vol. 21, p. 28559, nov 2013.

[71] M. U. Sadiq, M. R. Gleeson, N. Ye, J. O'Callaghan, P. Morrissey, H. Y. Zhang, K. Thomas, A. Gocalinska, E. Pelucchi, F. C. G. Gunning, B. Roycroft, F. H. Peters, and B. Corbett, "10 Gb/s InP-based mach-zehnder modulator for operation at 2 µm wavelengths," *Optics Express*, vol. 23, p. 10905, apr 2015.

[72] M. U. Sadiq, H. Zhang, J. O'Callaghan, B. Roycroft, N. Kavanagh, K. Thomas, A. Gocalinska, Y. Chen, T. Bradley, J. R. Hayes, Z. Li, S.-U. Alam, F. Poletti, M. N. Petrovich, D. J. Richardson, E. Pelucchi, P. O'Brien, F. H. Peters, F. Gunning, and B. Corbett, "40 Gb/s WDM transmission over 1.15-km HC-PBGF using an InP-based mach-zehnder modulator at 2 µm," *Journal of Lightwave Technology*, vol. 34, pp. 1706–1711, apr 2016.

[73] L. Soldano and E. Pennings, "Optical multi-mode interference devices based on self-imaging: principles and applications," *J. Lightwave Technol.*, vol. 13, pp. 615–627, apr 1995.

[74] M. Nedeljkovic, A. Z. Khokhar, Y. Hu, X. Chen, J. S. Penades, S. Stankovic, H. M. H. Chong, D. J. Thomson, F. Y. Gardes, G. T. Reed, and G. Z. Mashanovich, "Silicon photonic devices and platforms for the mid-infrared," *Optical Materials Express*, vol. 3, p. 1205, aug 2013.

[75] Y. Wei, G. Li, Y. Hao, Y. Li, J. Yang, M. Wang, and X. Jiang, "Long-wave infrared 1 × 2 MMI based on air-gap beneath silicon rib waveguides," *Opt. Express*, vol. 19, p. 15803, aug 2011.

[76] R. Soref and B. Bennett, "Electrooptical effects in silicon," *IEEE Journal of Quantum Electronics*, vol. 23, pp. 123–129, jan 1987.

[77] A. Singh, "Free charge carrier induced refractive index modulation of crystalline silicon," in *7th IEEE International Conference on Group IV Photonics*, Institute of Electrical & Electronics Engineers (IEEE), sep 2010.

[78] M. Berciano, P. Damas, G. Marcaud, X. L. Roux, P. Crozat, C. A. Ramos, D. Benedikovic, D. Marris-Morini, E. Cassan, and L. Vivien, "Strained silicon photonics for pockels effect based modulation," in *2017 IEEE 14th International Conference on Group IV Photonics (GFP)*, IEEE, aug 2017.

[79] D. V. Simili, M. Cada, and J. Pistora, "Silicon slot waveguide electro-optic kerr effect modulator," *IEEE Photonics Technology Letters*, vol. 30, pp. 873–876, may 2018.

[80] J. Liu, M. Beals, A. Pomerene, S. Bernardis, R. Sun, J. Cheng, L. C. Kimerling, and J. Michel, "Waveguide-integrated, ultralow-energy GeSi electro-absorption modulators," *Nature Photonics*, vol. 2, pp. 433–437, may 2008.

[81] L. Mastronardi, M. Banakar, A. Khokhar, N. Hattasan, T. Rutirawut, T. D. Bucio, K. M. Grabska, C. Littlejohns, A. Bazin, G. Mashanovich, and F. Gardes, "High-speed si/GeSi hetero-structure electro absorption modulator," *Optics Express*, vol. 26, p. 6663, mar 2018.

[82] G. T. Reed, G. Mashanovich, F. Y. Gardes, and D. J. Thomson, "Silicon optical modulators," *Nature Photonics*, vol. 4, pp. 518–526, jul 2010.

[83] W. M. Green, M. J. Rooks, L. Sekaric, and Y. A. Vlasov, "Ultra-compact, low RF power, 10 Gb/s silicon mach-zehnder modulator," *Opt. Express*, vol. 15, no. 25, p. 17106, 2007.

[84] H. C. Nguyen, Y. Sakai, M. Shinkawa, N. Ishikura, and T. Baba, "10 Gb/s operation of photonic crystal silicon optical modulators," *Opt. Express*, vol. 19, p. 13000, jun 2011.

[85] S. Manipatruni, Q. Xu, B. Schmidt, J. Shakya, and M. Lipson, "High speed carrier injection 18 Gb/s silicon micro-ring electro-optic modulator," in *LEOS 2007 - IEEE Lasers and Electro-Optics Society Annual Meeting Conference Proceedings*, Institute of Electrical & Electronics Engineers (IEEE), oct 2007.

[86] L. Liao, D. Samara-Rubio, M. Morse, A. Liu, D. Hodge, D. Rubin, U. D. Keil, and T. Franck, "High speed silicon mach-zehnder modulator," *Opt. Express*, vol. 13, no. 8, p. 3129, 2005.

[87] M. Webster, P. Gothoskar, V. Patel, D. Piede, S. Anderson, R. Tummidi, D. Adams, C. Appel, P. Metz, S. Sunder, B. Dama, and K. Shastri, "An efficient MOS-capacitor based silicon modulator and CMOS drivers for optical transmitters," in *11th International Conference on Group IV Photonics (GFP)*, Institute of Electrical & Electronics Engineers (IEEE), aug 2014.

[88] K. Debnath, D. J. Thomson, W. Zhang, A. Z. Khokhar, C. Littlejohns, J. Byers, L. Mastronardi, M. K. Husain, K. Ibukuro, F. Y. Gardes, G. T. Reed, and S. Saito, "All-silicon carrier accumulation modulator based on a lateral metal-oxide-semiconductor capacitor," *Photonics Research*, vol. 6, p. 373, apr 2018.

[89] A. Liu, L. Liao, D. Rubin, H. Nguyen, B. Ciftcioglu, Y. Chetrit, N. Izhaky, and M. Paniccia, "High-speed optical modulation based on carrier depletion in a silicon waveguide," *Opt. Express*, vol. 15, p. 660, jan 2007.

[90] D. J. Thomson, F. Y. Gardes, J.-M. Fedeli, S. Zlatanovic, Y. Hu, B. P. P. Kuo, E. Myslivets, N. Alic, S. Radic, G. Z. Mashanovich, and G. T. Reed, "50-Gb/s silicon optical modulator," *IEEE Photonics Technology Letters*, vol. 24, pp. 234–236, feb 2012.

[91] D. Patel, S. Ghosh, M. Chagnon, A. Samani, V. Veerasubramanian, M. Osman, and D. V. Plant, "Design, analysis, and transmission system performance of a 41 GHz silicon photonic modulator," *Optics Express*, vol. 23, p. 14263, may 2015.

[92] A. Samani, M. Chagnon, D. Patel, V. Veerasubramanian, S. Ghosh, M. Osman, Q. Zhong, and D. V. Plant, "A low-voltage 35-GHz silicon photonic modulator-enabled 112-gb/s transmission system," *IEEE Photonics Journal*, vol. 7, pp. 1–13, jun 2015.

[93] S. Shao, J. Ding, L. Zheng, K. Zou, L. Zhang, F. Zhang, and L. Yang, "Optical PAM-4 signal generation using a silicon mach-zehnder optical modulator," *Optics Express*, vol. 25, p. 23003, sep 2017.

[94] H. Xu, X. Li, X. Xiao, P. Zhou, Z. Li, J. Yu, and Y. Yu, "High-speed silicon modulator with band equalization," *Optics Letters*, vol. 39, p. 4839, aug 2014.

[95] R. Ding, Y. Liu, Q. Li, Y. Yang, Y. Ma, K. Padmaraju, A. E.-J. Lim, G.-Q. Lo, K. Bergman, T. Baehr-Jones, and M. Hochberg, "Design and

characterization of a 30-GHz bandwidth low-power silicon traveling-wave modulator," *Optics Communications*, vol. 321, pp. 124–133, jun 2014.

[96] R. Ding, Y. Liu, Y. Ma, Y. Yang, Q. Li, A. E.-J. Lim, G.-Q. Lo, K. Bergman, T. Baehr-Jones, and M. Hochberg, "High-speed silicon modulator with slow-wave electrodes and fully independent differential drive," *Journal of Lightwave Technology*, vol. 32, pp. 2240–2247, jun 2014.

[97] D. Marris-Morini, L. Virot, C. Baudot, J.-M. Fédéli, G. Rasigade, D. Perez-Galacho, J.-M. Hartmann, S. Olivier, P. Brindel, P. Crozat, F. Bœuf, and L. Vivien, "A 40 gbit/s optical link on a 300-mm silicon platform," *Optics Express*, vol. 22, p. 6674, mar 2014.

[98] Y. Yang, Q. Fang, M. Yu, X. Tu, R. Rusli, and G.-Q. Lo, "High-efficiency si optical modulator using cu travelling-wave electrode," *Optics Express*, vol. 22, p. 29978, nov 2014.

[99] X. Tu, T.-Y. Liow, J. Song, X. Luo, Q. Fang, M. Yu, and G.-Q. Lo, "50-Gb/s silicon optical modulator with traveling-wave electrodes," *Opt. Express*, vol. 21, p. 12776, May 2013.

[100] P. Dong, L. Chen, and Y. kai Chen, "High-speed low-voltage single-drive push-pull silicon mach-zehnder modulators," *Optics Express*, vol. 20, p. 6163, feb 2012.

[101] W. Cao, D. Hagan, D. J. Thomson, M. Nedeljkovic, C. G. Littlejohns, A. Knights, S.-U. Alam, J. Wang, F. Gardes, W. Zhang, S. Liu, K. Li, M. S. Rouifed, G. Xin, W. Wang, H. Wang, G. T. Reed, and G. Z. Mashanovich, "High-speed silicon modulators for the 2µwavelength band," *Optica*, vol. 5, p. 1055, aug 2018.

[102] W. Wang, Z. Zhang, X. Guo, J. Zhou, S. J. X. Brian, M. S. Rouifed, C. Liu, C. Littlejohns, G. T. Reed, and H. Wang, "Mid-infrared (MIR) mach-zehnder silicon modulator at 2μm wavelength based on interleaved PN junction," in *Conference on Lasers and Electro-Optics*, OSA, 2018.

[103] W. Cao, M. Nedeljkovic, S. Liu, C. G. Littlejohns, D. J. Thomson, F. Gardes, Z. Ren, K. Li, G. T. Reed, and G. Z. Mashanovich, "25 gbit/s silicon based modulators for the 2 µm wavelength band (accepted)," in *Optical Fiber Communication Conference*, OSA, 2020.

[104] A. B. Fallahkhair, K. S. Li, and T. E. Murphy, "Vector finite difference modesolver for anisotropic dielectric waveguides," *Journal of Lightwave Technology*, vol. 26, pp. 1423–1431, jun 2008.

[105] M. T. Thompson, "Review of diode physics and the ideal (and later, non-ideal) diode," in *Intuitive Analog Circuit Design*, pp. 53–86, Elsevier, 2014.

[106] G. Ghione, "Modulators," in *Semiconductor Devices for High-Speed Optoelectronics*, pp. 356–439, Cambridge University Press.

[107] D. J. Thomson, F. Y. Gardes, S. Liu, H. Porte, L. Zimmermann, J.-M. Fedeli, Y. Hu, M. Nedeljkovic, X. Yang, P. Petropoulos, and G. Z. Mashanovich, "High performance mach-zehnder-based silicon optical modulators," *IEEE Journal of Selected Topics in Quantum Electronics*, vol. 19, pp. 85–94, nov 2013.

[108] D. Patel, V. Veerasubramanian, S. Ghosh, A. Samani, Q. Zhong, and D. V. Plant, "High-speed compact silicon photonic michelson interferometric modulator," *Optics Express*, vol. 22, p. 26788, oct 2014.

[109] G. T. Reed and A. P. Knights, *The Basics of Guided Waves*, pp. 11–36. Wiley-Blackwell, jan 2005.

[110] P. Besse, M. Bachmann, H. Melchior, L. Soldano, and M. Smit, "Optical bandwidth and fabrication tolerances of multimode interference couplers," *Journal of Lightwave Technology*, vol. 12, pp. 1004–1009, jun 1994.